Slip-tremor interaction at the very beginning of Episodic Tremor and Slip in Cascadia

Yuji Itoh[1,2], Anne Socquet[1], and Mathilde Radiguet[1]

[1]Univ. Grenoble Alpes, Univ. Savoie Mont Blanc, CNRS, IRD, Univ. Gustave Eiffel, ISTerre, 38000 Grenoble, France
[2]Earthquake Research Institute, The University of Tokyo, Tokyo, Japan

Key Points:

- Multi-site stacking of geodetic deformation time series efficiently resolves moment function of slow slip during its initiation
- Geodetic moment tends to dramatically accelerate ∼1 day after the tremor onset during the initiation of Episodic Tremor and Slip in Cascadia
- Unruptured tremor patches perhaps represent a relatively strong portion of the ETS zone fault, which impacts the SSE growth

Corresponding author: Yuji Itoh, `yitoh@eri.u-tokyo.ac.jp`

Abstract

In Cascadia, the concomitance of slow slip events (SSE) and tremors during Episodic Tremor and Slip (ETS) episodes is well documented. Brittle tremor patches embedded in the ductile background deforming aseismically is the most common sketch for the fault structure, but whether tremor patches impact the SSE process is under debate. This study focuses on the initiation stage of major Cascadia ETSs. So far, few observational constraints exist on the details of ETS initiation because spatiotemporal SSE inversions usually oversmooth their temporal evolution. Scrutinizing tremors and SSE over a short period at the beginning of major ETS events gives us insights into their mechanical relationship. We directly retrieve the temporal evolution of SSE moment by stacking subdaily Global Navigation Satellite System time series at multiple sites, without slip inversions. Comparison of the GNSS stack with tremor activity demonstrates that SSE moment release accelerates drastically $\sim$1 day after the onset of vigorous tremor activity. We propose that heterogeneous interface strength limits the growth of SSE and that unruptured tremor patches may strengthen the fault. This scenario suggests that seeds of SSE grow more efficiently with the macroscopic weakening of the interface through the rupture of tremor patches. In that scenario, isolated tremor bursts lacking SSE signal would mark failed and aborted initiation due to an under-stressed interface. When the SSE moment release accelerates, the tremor area expands more rapidly, suggesting that the growth of the ETS occurs through a feedback mechanism between slip and tremor once the SSE is well developed.

Plain Language Summary

Slow slip events (SSE) and tremors are aseismic and seismic components of the slow earthquake family, respectively, which have considerably smaller slip rates than regular fast earthquakes. In the Cascadia subduction zone, they occur at the down-dip extension of the seismogenic zone along the subduction interface. Their interaction during the initiation of SSEs should provide us with insights into their mechanical connection, but it is so far unclear because of the technical limitations of conventional SSE analysis methods. By analyzing the temporal evolution of SSEs in Cascadia using a stacking method for geodetic time series at multiple observation sites, we found that tremor occurrence tends to precede the acceleration of SSE during the initiation stage. Enlightened by our knowledge from other seismological observations and computer simulations of SSE and tremors, the observed lag implies that unruptured tremor patches might represent a relatively strong location of the locked plate interface and that SSE can grow more efficiently after the rupture of these tremor patches, unpinning the interface.

1 Introduction

Slow earthquakes are prevalent on tectonic faults in various settings around the world (Obara & Kato, 2016; Peng & Gomberg, 2010). They are shear slip like regular earthquakes, but their slip rate and rupture velocity are considerably lower (and hence event duration is longer) than regular "fast" earthquakes with comparable magnitude (e.g., H. Gao et al., 2012; Ide et al., 2007; Ito et al., 2007; Royer & Bostock, 2014; Schmidt & Gao, 2010; Shelly et al., 2006, 2007; Sweet et al., 2014). Tremors and low frequency earthquakes (LFEs) are a seismic manifestation of slow earthquake processes with feeble shaking, and tremors are thought to be swarms of LFEs (e.g., Kao et al., 2005; Obara, 2002; Shelly et al., 2006, 2007). Slow slip events (SSEs) are aseismic fault transient slips lasting for days to years, captured by geodetic observations such as Global Navigation Satellite System (GNSS) or Global Positioning System (GPS) (e.g., Dragert et al., 2001; Nishimura et al., 2013), tiltmeters (e.g., Hirose & Obara, 2005; Yabe et al., 2023), or strainmeters (e.g., Dragert & Wang, 2011; Hawthorne et al., 2016; Katsumata et al., 2024; Yabe et al., 2023). These seismic and aseismic components of the slow earthquake family are observed simultaneously in space and time in some subduction zones such as Cascadia, also called "Episodic tremor and slip (ETS)" (Rogers & Dragert, 2003). The spatiotemporal association of tremor and SSE is usually found at the down-dip extension of the seismogenic zone (e.g., Behr & Bürgmann, 2021; Obara & Kato, 2016; Peng & Gomberg, 2010), where the fault rheology transitions from brittle to ductile regime due to the gradual increase of pressure and temperature with depth (Scholz, 1998). Geological outcrops of ancient ETS fault zone evidence the presence of finite-thickness megathrust consisting of a mixture of ductile and brittle materials at the ETS depth (e.g., Angiboust et al., 2015; Behr & Bürgmann, 2021; Fagereng et al., 2014; Kotowski & Behr, 2019; Ujiie et al., 2018; Tulley et al., 2022) which are thought to host SSE and seismic slow earthquakes (LFE and tremors), respectively. Brittle-ductile mixture (e.g., Ando et al., 2012, 2023; Beall et al., 2019; Behr et al., 2021; Lavier et al., 2021; Wu, 2021) and the asperity-in-matrix (e.g., Luo & Liu, 2019, 2021) models for ETS are inspired by the geological evidence.

Despite the well-known concomitance of tremors and SSE, their mechanical relationship remains unraveled. Tremor patches are known to be much weaker than regular earthquake patches (e.g., Houston, 2015; Ide & Tanaka, 2014). Tremors are therefore usually considered a passive response to SSE that does not impact the SSE behavior (e.g., Bartlow et al., 2011). Contrary to this weak tremor patch scenario, a few observations suggest that unruptured tremor patches modulate the behavior of ETS by introducing heterogeneity in the interface strength (Yabe & Ide, 2014). Because the difference between these two scenarios should be most evident when the SSE moment rate is low, the ETS behavior at its very beginning should give key insights into the mechanics of SSE growth and the mechanical relationships between tremors and SSE. Although tremor behavior at the initiation of ETS has been well studied (Houston, 2015; Sweet et al., 2019; Yabe & Ide, 2014; Yabe et al., 2015), the temporal evolution of SSE moment during the ETS initiation remains poorly documented because time-dependent inversion of daily GNSS data usually smooth temporal evolution of SSE, regardless of the inversion method used (e.g., Fukuda et al., 2008; Radiguet et al., 2011; Segall & Matthews, 1997). Some inversion methods do not explicitly impose any temporal smoothness constraint, but even in such cases, the data fit plots exhibit smoother slip evolution than the actual (Bletery & Nocquet, 2020) or inferred temporal evolution of slip and potentially lack details of their actual evolution (e.g., Gualandi et al., 2016; Kositsky & Avouac, 2010; Michel et al., 2019; Zhang et al., 2023). Hence, despite these technical advances and the substantial expansion of GNSS networks, the initiation process of SSEs and their relationship with tremors is hardly imaged. Another method to resolve the temporal evolution of the SSE initiation without inversion is necessary to obtain novel insights into the mechanics of ETS initiation.

The initiation stage of ETSs, which corresponds to the initial growth preceding their lateral migration, is expected to last for only up to a few days (Bartlow et al., 2011; Hall et al., 2019; Itoh et al., 2022; Michel et al., 2019; Wech & Bartlow, 2014). Hence, daily GNSS coordinates, most widely used for imaging SSE processes, cannot access the details of initiation processes. Strainmeters and tiltmeters have sub-daily temporal resolution for SSE imaging, but their application to studies of SSEs is not always straightforward because they are sensitive to non-tectonic processes such as precipitations and their spatial distribution is generally not as dense as GNSS stations (e.g., Dragert & Wang, 2011; Hawthorne et al., 2016; Hirose & Obara, 2005; Katsumata et al., 2024; Yabe et al., 2023). Noise level of sub-daily GNSS coordinates is typically of centimeters (e.g., Itoh & Aoki, 2022; Itoh et al., 2022; Twardzik et al., 2019), which is larger than SSE-induced surface motion, of a few millimeters (e.g., Bartlow et al., 2011; Dragert et al., 2001; Michel et al., 2019; Nishimura et al., 2013; Okada et al., 2022; Rousset et al., 2017; Wech & Bartlow, 2014). Yet, a recent application of sub-daily GNSS coordinates to a major SSE in Cascadia demonstrated that after carefully removing of inherent fluctuations, the long-period component of SSE-induced surface motion can be captured with a much finer time interval than using daily time series (Itoh et al., 2022). Hence, the sub-daily GNSS time series is a dataset with great potential to resolve processes at the initiation stage of SSEs if their fluctuations are properly mitigated and/or modeled.

We first present a new data analysis specifically targeting the initiation stage of ETSs in Cascadia. We exclude spatiotemporal SSE inversions of GNSS time series to avoid the distortion of the actual temporal evolution of the SSE moment. Instead, we stack sub-daily GNSS time series to improve signal-to-noise ratio (e.g., Bletery & Nocquet, 2023; Jara et al., 2024; Marill et al., 2021; Rousset et al., 2017). Based on the obtained results, we discuss two end-member models of interaction between tremor and SSE and propose a conceptual model of ETS initiation which can reconcile major observational features of ETS. In this study, we purposely use the term ”initiation” instead of ”nucleation” to describe the earliest stage of ETS events, as ”nucleation” is a specific term for earthquake initiation with frictional instability (e.g., McLaskey, 2019), which can inadequately narrow the range of possible physical process behind the beginning of ETS. We design all the analyses to discuss the first-order feature of ETS, that is, their initial growth that precedes their lateral migration. Many observational features of ETS in a finer spatial and temporal scale are ignored for the sake of simplification (e.g., Bletery et al., 2017; Ghosh et al., 2010; Hawthorne et al., 2016; Houston et al., 2011; Rubin & Armbruster, 2013).

2 Data analysis

In this section, we describe our data analysis strategy specifically designed for the ETS initiation stage. We went through three steps: (1) identifying zones of SSE initiation using associated tremors, (2) calculating the cumulative tremor count with time in this zone, and (3) stacking sub-daily GNSS time series at multiple sites weighted by surface displacements expected from unit slip in the initiation zone. This procedure allows us to quantify the temporal evolution of tremor and SSE at the ETS initiation stage.

2.1 Initiation event selection

In this study, we focus on the temporal evolution of SSE moment at the initiation stage, by analyzing major ETSs reported by previous studies in Cascadia (e.g., Bartlow et al., 2011; Bletery & Nocquet, 2020; Costantino et al., 2023; Dragert et al., 2001; Dragert & Wang, 2011; Itoh et al., 2022; Michel et al., 2019; Schmidt & Gao, 2010; Wech & Bartlow, 2014). We chose the Cascadia subduction zone as the target region because, there, short-term SSEs are on average larger than in other subduction zones such as Nankai (e.g., Hirose & Obara, 2005; Nishimura et al., 2013; Okada et al., 2022; Yabe et al., 2023) and well recorded with better spatiotemporal observation coverage than in Mexico (e.g., El Yousfi et al., 2023; Rousset et al., 2017). The availability of a long-lasting tremor catalog was another reason to choose Cascadia for our target (Ide, 2012; Wech, 2021). We used Michel et al. (2019)'s SSE catalog in Cascadia to pick up 9 spatial and temporal windows in which major ETSs occur (Table S1). The number of the picked windows is much smaller than the number of events reported in Michel et al. (2019)'s catalog because we noticed that some of their individual events can spatiotemporally be merged. We excluded the events before June 2009 because the dense tremor catalog was not available at that time. We focus only on northern and central Cascadia where plenty of GNSS stations are available above and around the ETS zone (Table 1).

We plotted tremors in each spatiotemporal window to identify each ETS' initiation zone. Our analysis mainly employed the Pacific Northwest Seismic Network (PNSN; Wech, 2021) catalog, which starts on August 6, 2009 (Decimal Year 2009.5954825462) in the region of interest. We noticed that the activity of Event #1 (Tables 1 and S1) initiated before that date, so we merged the tremor catalog of the World Tremor Database (WTD; Ide, 2012; Idehara et al., 2014) with the PNSN catalog before that date. The density of recorded tremors is much smaller in WTD than in PNSN, which impacts the event count evolution. Nevertheless, as we discuss later, the qualitative discussion and conclusions still hold, so we included this event in our analysis. Based on the spatiotemporal pattern of tremor epicenters and their strike-time plots (Figures 1c-d and S1c-d-S12c-d), we visually identified approximate areas of ETS initiation. Some events, which start at one along-strike location and migrate unilaterally or bilaterally, have only one initiation stage. On the other hand, some SSEs show more complex and irregular spatiotemporal evolution patterns. For instance, some of them started at multiple places and merged in the end (Event #6-7 (Figure S5-S6), e.g., Bletery & Nocquet, 2020). An ETS in spring 2017 near the Canada-US border experienced a short halt of tremor activity shortly after the migration started (Event #12-13 (Figure S11-S12), e.g., Itoh et al., 2022; Luo & Liu, 2019). For such irregular events, we defined multiple initiation stages. In total, we obtained 13 initiation stages to analyze, from the 9 major ETSs considered (Figures 1 and S1-S12; Tables 1 and S1). In the rest of this paper, the term "event" describes each ETS's initiation, not the entire process of the ETS.

We defined the area of the initiation stage for each event solely based on the tremors. We defined the initiation zone as an area where a cluster of tremors appear but do not propagate along-strike and continue for a while (Figures 1c and S1c-S12c). We designed a square which encloses the spatially distributing tremors associated with the initiation stages. We manually adjusted the square size and location by checking the spatial pattern of tremor epicenters and along-strike versus time tremor distribution to gain the preferred initiation zone quantification (Figures 1 and S1-S12). We counted the cumulative number of tremors with time inside the initiation zone (green in Figures 1b and S1b-S12b). The interval of the tremor count series is 5 minutes, which is consistent with the sampling rate of sub-daily GPS coordinates we used (Section 2.2). We explain our definition of the onset time of the tremor activity in Section 3.1.

2.2 Multi-site stacking of sub-daily GPS time series

We employed GPS coordinates at a 5-minute interval processed by Nevada Geodetic Laboratory (Blewitt et al., 2018) to resolve the moment release associated with the SSE initiation. We first, corrected them for various noise by mostly following the procedure of Moutote et al. (2023) and Itoh et al. (2023) (Figure S13a): after fixing the coordinates into the North American plate reference frame (Altamimi et al., 2017), we removed spatiotemporally correlating fluctuations due to multipath (e.g., Choi et al., 2004; Itoh & Aoki, 2022; Larson et al., 2007; Ragheb et al., 2007), diurnal variation (Itoh et al., 2022). Then, we removed the common mode error (e.g., Wdowinski et al., 1997) and outliers from the time series. Finally, we removed artificial offsets due to instrumental changes and other technical reasons on days described on NGL's database. The detailed procedures of each step are supplied in Text S1.

To resolve the temporal evolution of SSE at the initiation stage, we performed a weighted stack of multi-site time series (e.g., Bletery & Nocquet, 2023; Jara et al., 2024; Marill et al., 2021; Okada et al., 2022; Rousset et al., 2017; Wdowinski et al., 1997). For each event e, the GPS stack $d_e(t)$ is:

$$d_e(t) = \frac{\sum_{i=1}^{N_e} \mathbf{d}_i^{GPS}(t) \cdot \mathbf{w}_i^e}{\sum_{i=1}^{N_e} |\mathbf{w}_i^e|}, \tag{1}$$

where the term $\mathbf{d}_i^{GPS}(t)$ is the cleaned GPS time series at site i out of N_e time series. Here, $\mathbf{d}_i^{GPS}(t)$ is a matrix containing two time series in the east and north directions. The weight term $\mathbf{w}_i^e$ is a two-dimensional vector containing east and north elastic displacement due to anticipated thrust slip in a template square fault located in the initiation zone, which was modeled using the dislocation model for the homogeneous isotropic elastic half-space (Okada, 1985). We adopted the square area we used to define the initiation zone for the template fault for GPS stack. For each event, $\mathbf{w}_i^e$ is time-invariant expected displacements associated with slip in the initiation zone. Their dot product $\mathbf{d}_i^{GPS}(t) \cdot \mathbf{w}_i^e$ projects the time series in the two directions into the anticipated SSE-induced displacement direction and assign a weight for multi-site stacking according to the anticipated displacement amplitude, similar to Marill et al. (2021) and Bletery and Nocquet (2023). This procedure naturally enhances the expected signal associated with the initiation stage of SSE. We then applied a moving median with a window length of 3 days to the stacked time series to mitigate high-frequency fluctuations and better resolve the long-period temporal evolution of the GPS stack. Finally, we removed the local linear trend which is evident prior to and/or following the transient during the high tremor activity period in the initiation zone (Figures 2a and S14a-S25a). We explain the details of template fault parameter setting, selection of sites to stack, and sensitivity tests regarding the choice of sites in Text S1 and Figure S26.

The GPS stack exhibits a rapid transient signal roughly during the high significant tremor activity in the initiation zone (Figures 2a and S14a-S25a). A synthetic test using a kinematic SSE model demonstrates that the GPS stacks we obtained (Figures 2a and S14a-S25a) are a reasonable approximation of moment-time function shape in the initiation zone (Text S2, Figure S27). The intrinsic assumption of the multi-site stacking approach is that the temporal change in the spatial pattern of slip during the SSE initiation stage is not significant in comparison with the station distribution. This assumption is clearly not satisfied when the SSE starts to migrate laterally. The same synthetic test (Section 2 and Figure S27) verifies that the actual moment-time history with a crack-like stationary expanding slip at the initiation stage (e.g., Bartlow et al., 2011; Gomberg et al., 2016; Itoh et al., 2022; Michel et al., 2019; Wech & Bartlow, 2014) is not distorted by stacking.

3 Temporal evolution of slip and tremor at their initiation stage

3.1 Definition of time window of the ETS initiation stage

The synthetic test also verifies that the surface displacement time series and the moment-time function match fairly well until the slip outside the initiation zone becomes significant (Section 2 and Figure S27). This means that for retrieving the moment release process at the initiation stage from the actual GPS stack, we should use the data before such a timing at which non-negligible moment release starts outside the initiation zone. To infer such timing, we use the tremor activity in the initiation zone. As the tremor activity dramatically decreases within the initiation zone once tremors start to migrate laterally, we defined the end time T_e of each initiation event e as the inflection point of the curve of cumulative tremor count in the ETS initiation zone. This inflection point is determined by computing the second time derivative of this curve (Figure S28). For the subsequent analysis, we only consider data before this end-time T_e (Figures 1 and S1-S12). We also defined the onset timing of tremor activities for each event T_e^{tb} by the same approach.

3.2 Acceleration of slip moment and tremors at different timings

A comparison of the stacked GPS (referred to as slip proxy hereafter) and the cumulative tremor count in the initiation zone (referred to as tremor proxy hereafter) suggests their temporal shift for most of the analyzed events (Figures 2, 3a, 4a, and S14-S25). We measured this temporal shift for each event by calculating the cross-correlation (CC) between the tremor and slip proxy curves (Figures 3 and S14-S25). A compilation of the measured temporal shift systematically indicates that the slip proxy is delayed from 0 to less than 2 days with respect to the tremor proxy, except for one event with the lowest correlation (Figure 3c). CC curves as a function of the temporal shift show a plateau near the maximum CC value, but the range of shift values with high CC values is usually found on the positive side (Figures 3 and S14-S25), which supports the delay. The measured delay for Event #1 is likely biased by the merged tremor catalog, but the delay of slip proxy holds for Event #1 because the PNSN catalog records considerably ampler tremors than WTD (e.g., Figure 11c of Michel et al., 2019). The temporal shift of onset timings of the observed tremors and SSEs for all the events reflects the difference in detection capability of tremors and SSEs with seismometers and GNSS, respectively. GNSS data are unable to record signals of low amplitudes, and will thus be blind to aseismic moment release at a low rate. Hence, this shift marks the delay between the onset of vigorous tremor activity and the acceleration of the moment release. This interpretation implicitly but reasonably assumes that no significant change in the noise level of GNSS during each event's period. We discuss the possibility of a tiny moment release before the acceleration observed by the multi-site stack in Section 3.3. There are numerous short-duration tremor bursts which last for only a few days and are not accompanied by detectable slip signals (Figures 1c and S1c-S12c)(e.g., Frank, 2016; Wech, 2021). This implies that a typical time scale of acceleration of SSE moment release is a few days.

Another way to illustrate the difference between slip and tremor evolution is to represent the slip proxy as a function of the tremor proxy (Figure 4b). For a fair comparison among all the analyzed events, we normalized each slip and tremor axis by their final value at the end of the initiation stage at time T_e (Figures 4b-c). The use of the unnormalized slip moment and tremor proxies makes it more difficult to illustrate their general feature (Figure 4c). In spite of the fluctuations in each event's tremor-slip curve, the geodetic slip moment rate per seismic tremor count tends to be larger at the later stage. To confirm this tendency, we stacked the normalized curves of all the events to retrieve the average behavior (Figures 4b). The stacked tremor-slip curve clearly exhibits the gradual acceleration of geodetic slip moment release with respect to the development of tremor activity. In other words, the slip moment per tremor increases with time.

Although the cumulative tremor count does not significantly accelerate in the initiation zone following the SSE moment acceleration (Figure 4a), some tremor properties are known to increase after the first few days since the onset of ETS. For example, tidal sensitivity of LFEs and tremors (Houston, 2015; Sweet et al., 2019) and tremor energy (Yabe & Ide, 2014; Yabe et al., 2015) increases after the first few days of each ETS. Similarly, our results show that tremor energy for events #12 and #13 also increases after the first few days (Figure S29). Likewise, LFE amplitudes increase during the first 12 hours and so (Rubin & Armbruster, 2013). Together with our data analysis results, they suggest that the mechanical interaction mode between SSE and tremors changes after the first few days of ETS.

3.3 Function shape of SSE moment release

We examined how the SSE moment release evolves with time during the ETS initiation. For most events, the following piece-wise linear function approximates well the slip proxy (Figure 4a):

$$\begin{aligned} \hat{d}_e(t) &= c_{e1} & (t < T_e^{sb}), \\ &= c_{e1} + c_{e2}\tfrac{t-T_e^{sb}}{T_e-T_e^{sb}} & (T_e^{sb} \leq t \leq T_e), \end{aligned} \tag{2}$$

where $\hat{d}_e(t)$ is the individual-event stack for event e following the smoothing and the local trend removal, c_{e1} and c_{e2} are the initial position and the amplitude of the GPS stack for each ETS initiation event, respectively, and T_e^{sb} and T_e are the onset and the end time of the SSE moment release. T_e was defined in Section 3.1 and T_e^{sb} was determined by grid search at an interval of 0.1 days. This piece-wise linear approximation gives us the shortest estimation of the duration of slip moment release during each ETS initiation. The determined T_e^{sb} is typically later than the tremor onset T_e^{tb} (Section 3.1; Figures 4a and S28) and this tendency, $T_e^{sb} > T_e^{tb}$ for most events e, is consistent with the CC-based delay quantification (Figure 3c).

The gradual development of slip moment with respect to the tremor development (Figures 4b-c) and the shift between T_e^{sb} and T_e^{tb} (Figure 4a) hint at a tiny slip moment release prior to $t = T_e^{sb}$, that is buried in the noise of the GPS stack. We carried out a multi-event stack, by stacking the slip proxy of all the events to resolve such signal. To achieve that, we first aligned the time axis for each event by setting a new origin at each $t = T_e^{sb}$ so that $t' = t - T_e^{sb}$ (Figure 5a) and weighted each individual-event slip proxy based on their typical fluctuation level computed as a standard deviation prior to $t' = 0$. The obtained multi-event stack shows an onset of signal (Figure 5b) for $t' < 0$. This signal onset earlier than $t' = 0$ represents a possible tiny slip signal prior to the rapid linear moment release before $t = T_e^{sb}$ for each event. We determined the onset timing of this tiny slip moment release $t' = T_{mb}$ to be -0.7 days by another piecewise linear fit as follows:

$$\begin{aligned} d(t) &= c_3 + c_4 t' & (t' < T_{mb}), \\ &= c_3 + c_4 t' + c_5 \tfrac{t' - T_{mb}}{T_m - T_{mb}} & (T_{mb} \leq t' \leq T_m), \end{aligned} \tag{3}$$

where $d(t)$, c_3, c_4, and c_5 are the multi-event stack, the initial position, the local linear trend, and the amplitude of the multi-event stack, respectively, and T_m is the end time of the moment release for the multievent stack, which is determined from the duration of slip moment release determined by individual-event stacks, namely, $T_m = \min_e (T_e - T_e^{sb})$. We carried out a bootstrap test for this multi-event stack and gained a distribution of the onset time T_{mb} associated with each resampling (Figure 5b). The distribution of T_{mb} values shows that T_{mb} is likely the negative value, implying a tiny moment release prior to the larger linear moment release.

Our individual-event and multi-event stack analyses showed the presence of the two moment rates, namely, the rapid release ($c_{e2}/(T_e - T_e^{sb})$) and the much slower release ($c_5/(T_m - T_{mb})$) prior to the rapid release. Although our fits used the piecewise function, this implies that the slip moment release during the ETS initiation does not suddenly start but gradually accelerates. An exponential acceleration could be a candidate of such a gradual initiation as an analog to earthquake nucleation (Figure 5c; e.g., Cattania, 2023; Favreau et al., 1999; Latour et al., 2013), but other continuous acceleration functions such as polynomial and power-law (e.g., Latour et al., 2013; Noda et al., 2013) functions would equally fit the multi-event stack because of the noise inherent to GNSS time series. Hence, it is difficult to constrain the physical mechanism of SSE initiation by directly comparing the slip proxy with analytical slip evolution functions based on theoretical and experimental derivations of unstable slip.

3.4 Development of tremor activity area

Although not migrating along strike, the spatial extent of tremors expands during this initiation stage. Therefore, we analyzed the tremors at the initiation stage to explore the relationship between the evolution of the spatial extent of tremors and the slip moment evolution. For the analysis of each ETS initiation event, we first extracted tremors within a 150 km × 150 km square centered at the middle of each template fault (Figure 6). Then, to align the time axis of each event, we converted their occurrence time into a normalized time axis defined as follows:

$$t_{norm} = \frac{t - T_e^{sb}}{T_e - T_e^{sb}}, \tag{4}$$

where t and t_{norm} indicate the time axis before and after the normalization and T_e^{sb} and T_e are already defined in Equation (2) for each ETS initiation event e. With this normalization, $t_{norm} < 0$ and $t_{norm} \geq 0$ correspond to the period before and during the SSE moment release detectable with the multi-site stack for each individual event, respectively. The period $t_{norm} \geq 1$ corresponds to the migration stage. We inferred the effective area of the tremor activity by fitting an ellipse enclosing about 95% of tremor epicenters using singular value decomposition analysis. For each ETS initiation event, we took tremors from $t_{norm} = -1$ to $t_{norm} = T_{area}$ with T_{area} varied from -0.6 to 1 to illustrate the temporal evolution of area until the onset of the migration stage. We provide more details of the tremor area estimation in Text S3. Most events we analyzed exhibit tremor occurrence prior to the emergence of detectable slip signal (i.e., $t_{norm} < 0$) as seen in our other analyses (Figures 3 and 4b). The area at $t_{norm} = 0$, namely, $A_e(t_{norm} = 0)$ could be considered a reasonable proxy for the minimum area of tremors to form the detectable ETS (Figure 7a). The ellipse area at $t_{norm} = 0$ varies from one event to another (Figure 7a) even for those initiating at similar locations (Figure 6), but the typical dimension is tens of kilometers.

The tremor areas $A_e(t_{norm})$ increase steadily in space and time for most events (Figures 6 and 7). To illustrate common features of tremor area evolution among the events, we focus on the normalized evolution of tremor areas $\Delta A_e(t_{norm})$ (Figure 7b) given as

$$\Delta A_e(t_{norm}) = \frac{A_e(t_{norm}) - A_e(t_{norm}^{min})}{A_e(1) - A_e(t_{norm}^{min})} \quad (5)$$

where $A_e(t_{norm})$ is the ellipse area of event e as a function of t_{norm}. The term t_{norm}^{min} is the normalized time when the first estimation of A_e is obtained, namely, when a sufficient number of tremors emerges to fit an ellipse. The compilation of $\Delta A_e(t_{norm})$ for the events we analyzed indicates a tendency for faster area increase at a later time, especially after $t_{norm} = 0$ (Figure 7b). This means that the tremor area develops more efficiently when the slip moment release grows significantly, suggesting a feedback process between tremors and slip. This feedback starts after the first few days (Section 3.2).

Actually, the ellipse approximation of the tremor activity area is not always a suitable approach for all the events. For example, Event #8 and #10 exhibit a jump of tremor cluster location during the initiation stage (Figures 6 and 7b). As a result, the tendency of the quicker area increase with the detectable SSE moment rate is blurred for them. Also, we excluded 4 events from the tremor area analysis for either of the following reasons. (1) No ellipse estimations before $t_{norm} = 0$ (Event #1; Figures 4a and S14), which is due to the catalog break on August 6 2009 (Section 2.1), (2) The onset time of linear moment release earlier than the tremor onset time due to the limitation of the piecewise linear fit (Event #3 and #13; Figures 4a, S15, and S25), or (3) The too uncertain onset time of linear moment release due to the very little number of GPS sites stacked (Event #9; Figures 4a and and S21).

4 Discussion

4.1 Mechanical interpretation using end-member models of slip-tremor interaction

We discuss the mechanical relationship between SSE and tremor during the ETS initiation. We first employ two end-member models proposed by previous studies and then propose a scenario reconciling them in the next section. Both end-member scenarios assume that tremor is a seismic rupture of a brittle stick-slip patch whereas SSE is an aseismic creep of the background matrix (e.g., Chestler & Creager, 2017a, 2017b; Luo & Liu, 2019, 2021). This stick-slip assumption for tremor agrees well with the recurrence of tremors at nearly identical locations (Rubin & Armbruster, 2013) and thrust-type mechanism solution of LFEs that compose tremors (Royer & Bostock, 2014; Shelly et al., 2007). The two scenarios assume a different relative strength of the unruptured tremor patches compared to the strength of the background SSE matrix. In one scenario, unruptured tremor patches are "strong" so that they prevent SSEs from accelerating. In the other scenario, unruptured tremor patches are weaker and they rupture in response to the SSE and do not modulate the SSE behavior. We compare our analysis results, other observations, and model knowledge against the anticipated behavior for each scenario to discuss the plausible relationship between SSE and tremors. In the following discussion, we assume a planar heterogeneous fault consisting of brittle and ductile components, but our conceptual and qualitative discussion is directly applicable to the volumetric ETS zone fault model, which is favored by the geological outcrops (e.g., Angiboust et al., 2015; Behr & Bürgmann, 2021; Fagereng et al., 2014; Kotowski & Behr, 2019; Ujiie et al., 2018; Tulley et al., 2022).

The first scenario considers "strong" brittle tremor patches, which govern the interface fault strength, and the ductile background contributes little to the fault strength (Ando et al., 2023; Beall et al., 2019; Lavier et al., 2021; Wu, 2021). Small brittle seismogenic patches may couple the interface and collectively generate a stress shadow preventing the interface from slipping (Hetland & Simons, 2010). This simple mechanical sketch may be applicable for the ETS growth and, if so, tremor patches would pin the interface and prevent the background ductile matrix from creeping at an observable moment rate. In other words, the growth of SSEs in Cascadia would be hindered by the readiness of tremor patches to rupture and their spatial distribution. Fluid pressure and its temporal evolution indirectly modulate the interface strength and affect the readiness of the tremor patches. In this scenario, the lag between the onsets of tremor activity and detectable SSE moment acceleration would result from the necessity of interface unpinning by means of tremor occurrence to let SSE grow into a detectable size. The active tremor area at the onset of detectable slip (i.e., $Ae(t_{norm} = 0)$) variable from one event to another (Figure 7a) might also indicate that SSE growth is modulated by the distribution of unruptured tremor patches and their strength. Yet, whether unruptured tremor patches are strong enough to control the interface strength to generate the extensive inter-ETS locking in the ETS zone (Figure 8a; Saux et al., 2022) is questionable given the huge contrast in size and moment between the tremors and the surrounding SSE (Chestler & Creager, 2017b).

The other end-member scenario considers extremely weak unruptured tremor patches. Those patches do not contribute to the inter-ETS fault strength and locking which is instead supported by the background SSE fault. Tremors are a passive marker of slip (e.g., El Yousfi et al., 2023; Frank, 2016; Jolivet & Frank, 2020). This scenario is consistent with the huge contrast in size and moment between the tremors and the surrounding SSE (Chestler & Creager, 2017b). In this scenario, tremor patches do not modulate the SSE behavior. In such case, the lag between the acceleration of the SSE moment and the onset of tremor activity (Figures 3c and 4b) may simply highlight critically stressed tremor patches which respond to tiny local seeds of SSE. The growth of the SSE is controlled by the characteristic critical dimension of mildly velocity-strengthening faults (e.g., Liu & Rice, 2007), and the slip area needs to expand to the critical dimension to form a detectable SSE. Hence, the large characteristic dimension of tens of kilometers (Figure 7a and Section 3.4) might be responsible for the observed lag. However, this scenario possibly fails in explaining the occurrence of isolated tremor bursts in a smaller dimension than the critical length unless spatial variation of normal stress is introduced, which locally clamps the interface (e.g., Luo & Liu, 2021). Hence, highly non-uniform normal stress (and hence strength) distribution would be required to reproduce the spatiotemporally prevalent short tremor bursts. Fluids released from the subducted slab around the mantle wedge corner (e.g., Audet & Bürgmann, 2014; Audet et al., 2009; Farge et al., 2021; X. Gao & Wang, 2017; Gosselin et al., 2020; Liu & Rice, 2007, 2009; Shapiro et al., 2018) might contribute this heterogeneous stress distribution to some extent.

4.2 Proposed scenario of ETS initiation in Cascadia

We propose a scenario reconciling the two end-member models: both the unruptured brittle tremor patches and the background SSE fault zone contribute to the ETS zone fault strength, but unruptured tremor patches are a relatively strong portion compared to the background. To describe the anticipated ETS process in this scenario, we define four stages of ETS growth: (a) inter-ETS, (b) local unpinning, (c) slip-tremor feedback growth, and (d) migration stages. The ETS initiation stage corresponds to stages b and c (Figure 8). At the inter-ETS stage (Figure 8a), locking at a large slip deficit rate is anticipated in the ETS zone, supported by the recent geodetic analysis (Figure 8a; Saux et al., 2022). During this stage, only very tiny SSEs with feeble displacement signals are allowed, which are, however, hidden in the noise of geodetic observations and observable only by stacking a large amount of GNSS data (Frank, 2016; Jolivet & Frank, 2020). When tremor activity starts, namely, at the beginning of the local unpinning stage (Figure 8b), the locked background fault is locally unpinned. However, it is not allowed to form a detectable large slip while the rest of the interface remains coupled, partly supported by unruptured tremor patches. Our multi-event stack suggests the presence of such a tiny slip during the local unpinning stage (Figure 5). Once a sufficient number of tremor patches are ruptured, the background SSE fault creeps more efficiently. The lag between the tremor onset and the slip acceleration claims for a transition from the local unpinning to the slip-tremor feedback growth stages. This transition happens within a few days, as highlighted by many observations (Section 3.2). As such a fast slip rate triggers further unpinning of the interface, ETS grows as a feedback between slip and tremor (Figure 8c). The colocation of slip and tremor peaks during the initiation stage (e.g., Dragert & Wang, 2011; Hall et al., 2019; Itoh et al., 2022) supports the idea that the unpinning of the interface via tremor ruptures facilitates the creep of the interface. Once the SSE is grown, its stress perturbation may trigger tremors at the tip of the slipping area, which facilitates the spatial expansion of the slipping area. Then, once the slipping region saturates the down-dip extent of the ETS zone, the SSE can only propagate laterally (Gomberg et al., 2016), which is commonly seen as migration (Figure 8d). This stress-driven unpinning allows the slip peak to migrate into these unpinned areas in the lateral adjacent zones, resulting in the observed spatial shift of tremor and slip peaks (e.g., Dragert & Wang, 2011; Hall et al., 2019; Itoh et al., 2022).

The proposed scenario is consistent with the occurrence of isolated tremor bursts lasting for a few days without detectable slip signal unless extensively stacked (e.g., Frank, 2016; Jolivet & Frank, 2020) (Figures 1c and S1c-S12c). They can be interpreted as events aborting at the local unpinning stage (Figure 8b), which fail to evolve into the slip-tremor feedback growth stage (Figure 8c). Their more frequent occurrence than major ETSs is consistent with the assumption that the readiness of tremor patches to rupture controls the slip growth process. Hence, during most time of the ETS cycle, the interface state oscillates between the inter-ETS stage and the local unpinning stage.

4.3 Implication for moment-duration scaling of slow earthquakes

The scaling relationship between the moment and the duration of slow earthquakes offers a clue to their physical mechanism, but it has been under debate for decades (Frank & Brodsky, 2019; Ide & Beroza, 2023; Ide et al., 2007; Gomberg et al., 2016; Michel et al., 2019). The scaling relationship usually investigates the total moment and duration of each event, and the temporal evolution of this scaling for specific event phases (initiation, propagation, termination) has not been investigated. Such temporal snapshots should contain ample information which potentially constrains the underlying physical mechanisms of slow earthquakes, so we discuss a snapshot of the moment-duration scaling at the end of the ETS initiation stage. We converted the slip proxy (i.e., the moment-time function shape) into absolute moment evolution by following Bletery and Nocquet (2023); the moment function is linear to the GPS stack with a conversion coefficient which is a function of $\mathbf{w}_i^e$ in Equation (1) (i.e., the distribution of sites stacked and the template fault parameters). We attempted two different ways of measuring each initiation event's duration; the first one is based on the duration of the second section of the piecewise linear fit $T_e - T_e^{sb}$ (Figure 4a) and the other is based on the tremor activity duration in the initiation zone $T_e - T_e^{tb}$ (Figure S28). Whichever duration measurement we use, the moment and duration fall near the upper bound of cumulative slow earthquake moment with a given total duration Ide and Beroza (2023) (Figure 9). The linear relationship between moment and duration over the range of 0.1 seconds to a few years marks this upper bound Ide and Beroza (2023); Ide et al. (2007). This suggests that the moment and duration of SSEs evolve by following the upper bound during the migration stage, meaning that SSEs migrate diffusively. This diffusive nature of SSE migration is consistent with many observations and models (e.g., Ando et al., 2012; Ide, 2008; Ide & Maury, 2018).

During the initiation stage, the piecewise linear function in Equation (2) satisfactorily fits the moment proxy (i.e., the GPS stacks) for most events (Figure 4a), indicating that the development of SSE source during the slip-tremor feedback stage (Figure 8c) is also a diffusive process once the slip moment has significantly accelerated. Meanwhile, the development of ETS is not diffusive at the local unpinning stage (Figure 8b) because the multi-event stack suggests the presence of possibly continuous slip acceleration during this local unpinning stage (Figures 5). We speculate that the moment-duration relationship during the local unpinning follows that of tremors or LFEs as ingredients of tremors, which do not necessarily obey the linear scaling (Farge et al., 2020; Oikawa & Aso, 2024; Supino et al., 2020). The deviation from the linear scaling at the very beginning of ETS unpinning conforms also with the scenario that external perturbations activate the unpinning process such as continuous loading from the stable sliding zone (e.g., Wech & Creager, 2011), dynamic triggering (e.g., Itaba & Ando, 2011; Rubinstein et al., 2007, 2009), and fluid pressure transient (Gosselin et al., 2020; Kita et al., 2021; Nakajima & Uchida, 2018; Shapiro et al., 2018; Warren-Smith et al., 2019).

5 Conclusions

We carried out ETS analyses specifically designed to observationally illustrate the ETS initiation stage without time-dependent slip inversions which smooth the actual temporal history of moment release. Our results highlight that the significant acceleration of the SSE moment occurs $\sim$1 day after the onset of tremors. In agreement with other seismological observations, our results imply that SSE acceleration has a typical time scale of a few days to accelerate into a detectable moment rate. We also found that the tremor area expands more rapidly once the SSE moment has accelerated, suggesting slip-tremor feedback as an efficient way of ETS growth. We propose that the interface strength is controlled by both the tremor patches and the background SSE fault and unruptured tremor patches represent a relatively strong portion of the plate interface. Unruptured tremor patches may hinder the growth of the SSE, which becomes more efficient once these tremor patches rupture collectively (Figure 8a-b). Once the SSE has accelerated, SSE itself starts to trigger tremors, the rupture of which in turn facilitates the SSE growth, exhibiting a slip-tremor feedback growth (Figures 8c-d). Our moment-duration analysis suggests that this feedback growth might be a diffusive process. Quantitative validation of the proposed scenarios through numerical modeling and laboratory experiments is necessary in the future.

Open Research Section

We processed only published results/data and no new data were acquired. The GPS coordinates (Blewitt et al., 2018) are available from Nevada Geodetic Laboratory (2024). Tremors (Ide, 2012; Idehara et al., 2014; Wech, 2021) used in this study are retrieved from Pacific Northwest Seismic Network (2024) and World Tremor DataBase (2024). We used a Fortran 90 translation of DC3D and DC3D0 (Okada, 1985) provided as Miyashita (2020).

Table 1. List of ETS initiation events and template fault parameters

#	T_e (year)	Longitude (°)	Latitude (°)	Depth[a] (km)	Length (km)	Width (km)
1	2009.6088200624	-123.20	46.30	36.14	80	80
2	2010.6251806221	-123.00	47.50	40.43	70	70
3	2011.4477146551	-123.30	45.00	34.59	70	70
4	2012.6889972621	-124.50	48.90	36.96	70	70
5	2013.1751749182	-123.10	45.25	35.35	80	80
6	2013.7015457449	-123.00	47.50	40.43	100	100
7	2013.7201117956	-126.50	50.00	29.47	70	70
8	2014.9189482090	-123.00	47.70	41.25	70	70
9	2014.8558445509	-125.69	49.50	32.05	60	60
10	2015.9919100312	-124.40	48.90	37.86	100	100
11	2016.1103030649	-123.50	44.50	34.23	80	80
12	2017.1566278804	-123.00	47.60	40.81	80	80
13	2017.2233249677	-123.30	47.95	38.12	60	60

The rest of fault parameters is provided in Table S2
[a] Slab 2 (G. P. Hayes et al., 2018)

Acknowledgments

We appreciate Camilla Cattania, William Frank, Kelian Dascher-Cousineau, Hanaya Okuda, Roland Burgmann, Valère Lambert, Naoki Uchida, Aitaro Kato, Satoshi Ide, and Yoshihiro Kaneko for the fruitful discussion. Yuji Itoh was an Overseas Research Fellow of the Japan Society for the Promotion of Science (JSPS). This study is supported by JSPS KAKENHI 21K14007 (YI) and ERC CoG 865963 DEEP-trigger (AS).

References

Altamimi, Z., Métivier, L., Rebischung, P., Rouby, H., & Collilieux, X. (2017, 03). ITRF2014 plate motion model. *Geophysical Journal International*, *209*(3), 1906-1912. Retrieved from `https://doi.org/10.1093/gji/ggx136` doi: 10.1093/gji/ggx136

Ando, R., Takeda, N., & Yamashita, T. (2012). Propagation dynamics of seismic and aseismic slip governed by fault heterogeneity and newtonian rheology. *Journal of Geophysical Research: Solid Earth*, *117*(B11). Retrieved from `https://agupubs.onlinelibrary.wiley.com/doi/abs/10.1029/2012JB009532` doi: https://doi.org/10.1029/2012JB009532

Ando, R., Ujiie, K., Nishiyama, N., & Mori, Y. (2023). Depth-dependent slow earthquakes controlled by temperature dependence of brittle-ductile transitional rheology. *Geophysical Research Letters*, *50*(5), e2022GL101388. Retrieved from `https://agupubs.onlinelibrary.wiley.com/doi/abs/10.1029/2022GL101388` (e2022GL101388 2022GL101388) doi: https://doi.org/10.1029/2022GL101388

Angiboust, S., Kirsch, J., Oncken, O., Glodny, J., Monié, P., & Rybacki, E. (2015). Probing the transition between seismically coupled and decoupled segments along an ancient subduction interface. *Geochemistry, Geophysics, Geosystems*, *16*(6), 1905-1922. Retrieved from `https://agupubs.onlinelibrary.wiley.com/doi/abs/10.1002/2015GC005776` doi: https://doi.org/10.1002/2015GC005776

Audet, P., Bostock, M. G., Christensen, N. I., & Peacock, S. M. (2009). Seismic evidence for overpressured subducted oceanic crust and megathrust fault sealing. *Nature*, *457*(7225), 76–78. doi: https://doi.org/10.1038/nature07650

Audet, P., & Bürgmann, R. (2014). Possible control of subduction zone slow-earthquake periodicity by silica enrichment. *Nature*, *510*(7505), 389–392. doi: https://doi.org/10.1038/nature13391

Bartlow, N. M., Miyazaki, S., Bradley, A. M., & Segall, P. (2011). Space-time correlation of slip and tremor during the 2009 cascadia slow slip event. *Geophysical Research Letters*, *38*(18). Retrieved from `https://agupubs.onlinelibrary.wiley.com/doi/abs/10.1029/2011GL048714` doi: https://doi.org/10.1029/2011GL048714

Beall, A., Fagereng, A., & Ellis, S. (2019). Fracture and weakening of jammed subduction shear zones, leading to the generation of slow slip events. *Geochemistry, Geophysics, Geosystems*, *20*(11), 4869-4884. Retrieved from `https://agupubs.onlinelibrary.wiley.com/doi/abs/10.1029/2019GC008481` doi: https://doi.org/10.1029/2019GC008481

Behr, W. M., & Bürgmann, R. (2021). What's down there? the structures, materials and environment of deep-seated slow slip and tremor. *Philosophical Transactions of the Royal Society A: Mathematical, Physical and Engineering Sciences*, *379*(2193), 20200218. Retrieved from `https://royalsocietypublishing.org/doi/abs/10.1098/rsta.2020.0218` doi: 10.1098/rsta.2020.0218

Behr, W. M., Gerya, T. V., Cannizzaro, C., & Blass, R. (2021). Transient slow slip characteristics of frictional-viscous subduction megathrust shear zones. *AGU Advances*, *2*(3), e2021AV000416. Retrieved from `https://agupubs.onlinelibrary.wiley.com/doi/abs/10.1029/2021AV000416` (e2021AV000416 2021AV000416) doi: https://doi.org/10.1029/2021AV000416

Bletery, Q., & Nocquet, J.-M. (2020). Slip bursts during coalescence of slow slip events in cascadia. *Nature communications*, *11*(1), 2159.

Bletery, Q., & Nocquet, J.-M. (2023). The precursory phase of large earthquakes. *Science*, *381*(6655), 297-301. Retrieved from `https://www.science.org/doi/abs/10.1126/science.adg2565` doi: 10.1126/science.adg2565

Bletery, Q., Thomas, A. M., Hawthorne, J. C., Skarbek, R. M., Rempel, A. W., & Krogstad, R. D. (2017). Characteristics of secondary slip fronts associated with slow earthquakes in cascadia. *Earth and Planetary Science Letters*, *463*, 212-220. Retrieved from `https://www.sciencedirect.com/science/article/pii/S0012821X17300584` doi: https://doi.org/10.1016/j.epsl.2017.01.046

Blewitt, G., Hammond, W. C., & Kreemer, C. (2018). Harnessing the gps data explosion for interdisciplinary science. *EOS*, *99*. doi: 10.1029/2018EO104623

Cattania, C. (2023, 02). A Source Model for Earthquakes near the Nucleation Dimension. *Bulletin of the Seismological Society of America*, *113*(3), 909-923. Retrieved from `https://doi.org/10.1785/0120220045` doi: 10.1785/0120220045

Chestler, S. R., & Creager, K. C. (2017a). Evidence for a scale-limited low-frequency earthquake source process. *Journal of Geophysical Research: Solid Earth*, *122*(4), 3099-3114. Retrieved from `https://agupubs.onlinelibrary.wiley.com/doi/abs/10.1002/2016JB013717` doi: https://doi.org/10.1002/2016JB013717

Chestler, S. R., & Creager, K. C. (2017b). A model for low-frequency earthquake slip. *Geochemistry, Geophysics, Geosystems*, *18*(12), 4690-4708. Retrieved from `https://agupubs.onlinelibrary.wiley.com/doi/abs/10.1002/2017GC007253` doi: https://doi.org/10.1002/2017GC007253

Choi, K., Bilich, A., Larson, K. M., & Axelrad, P. (2004). Modified sidereal filtering: Implications for high-rate gps positioning. *Geophysical Research Letters*, *31*(22). doi: 10.1029/2004GL021621

Costantino, G., Giffard-Roisin, S., Radiguet, M., Dalla Mura, M., Marsan, D., & Socquet, A. (2023). Multi-station deep learning on geodetic time series detects slow slip events in cascadia. *Communications Earth & Environment*, *4*(1), 435.

doi: 10.1038/s43247-023-01107-7
Dragert, H., & Wang, K. (2011). Temporal evolution of an episodic tremor and slip event along the northern cascadia margin. *Journal of Geophysical Research: Solid Earth*, *116*(B12). Retrieved from `https://agupubs.onlinelibrary.wiley.com/doi/abs/10.1029/2011JB008609` doi: https://doi.org/10.1029/2011JB008609
Dragert, H., Wang, K., & James, T. S. (2001). A silent slip event on the deeper cascadia subduction interface. *Science*, *292*(5521), 1525-1528. Retrieved from `https://www.science.org/doi/abs/10.1126/science.1060152` doi: 10.1126/science.1060152
El Yousfi, Z., Radiguet, M., Rousset, B., Husker, A., Kazachkina, E., & Kostoglodov, V. (2023). Intermittence of transient slow slip in the mexican subduction zone. *Earth and Planetary Science Letters*, *620*, 118340. Retrieved from `https://www.sciencedirect.com/science/article/pii/S0012821X23003539` doi: https://doi.org/10.1016/j.epsl.2023.118340
Fagereng, A., Hillary, G. W. B., & Diener, J. F. A. (2014). Brittle-viscous deformation, slow slip, and tremor. *Geophysical Research Letters*, *41*(12), 4159-4167. Retrieved from `https://agupubs.onlinelibrary.wiley.com/doi/abs/10.1002/2014GL060433` doi: https://doi.org/10.1002/2014GL060433
Farge, G., Jaupart, C., & Shapiro, N. M. (2021). Episodicity and migration of low frequency earthquakes modeled with fast fluid pressure transients in the permeable subduction interface. *Journal of Geophysical Research: Solid Earth*, *126*(9), e2021JB021894. Retrieved from `https://agupubs.onlinelibrary.wiley.com/doi/abs/10.1029/2021JB021894` (e2021JB021894 2021JB021894) doi: https://doi.org/10.1029/2021JB021894
Farge, G., Shapiro, N. M., & Frank, W. B. (2020). Moment-duration scaling of low-frequency earthquakes in guerrero, mexico. *Journal of Geophysical Research: Solid Earth*, *125*(8), e2019JB019099. Retrieved from `https://agupubs.onlinelibrary.wiley.com/doi/abs/10.1029/2019JB019099` (e2019JB019099 10.1029/2019JB019099) doi: https://doi.org/10.1029/2019JB019099
Favreau, P., Campillo, M., & Ionescu, I. R. (1999, 10). Initiation of in-plane shear instability under slip-dependent friction. *Bulletin of the Seismological Society of America*, *89*(5), 1280-1295. Retrieved from `https://doi.org/10.1785/BSSA0890051280` doi: 10.1785/BSSA0890051280
Frank, W. B. (2016). Slow slip hidden in the noise: The intermittence of tectonic release. *Geophysical Research Letters*, *43*(19), 10,125-10,133. Retrieved from `https://agupubs.onlinelibrary.wiley.com/doi/abs/10.1002/2016GL069537` doi: https://doi.org/10.1002/2016GL069537
Frank, W. B., & Brodsky, E. E. (2019). Daily measurement of slow slip from low-frequency earthquakes is consistent with ordinary earthquake scaling. *Science Advances*, *5*(10), eaaw9386. Retrieved from `https://www.science.org/doi/abs/10.1126/sciadv.aaw9386` doi: 10.1126/sciadv.aaw9386
Fukuda, J., Miyazaki, S., Higuchi, T., & Kato, T. (2008). Geodetic inversion for space—time distribution of fault slip with time-varying smoothing regularization. *Geophysical Journal International*, *173*(1), 25–48. doi: https://doi.org/10.1111/j.1365-246X.2007.03722.x
Gao, H., Schmidt, D. A., & Weldon, I., Ray J. (2012, 02). Scaling Relationships of Source Parameters for Slow Slip Events. *Bulletin of the Seismological Society of America*, *102*(1), 352-360. Retrieved from `https://doi.org/10.1785/0120110096` doi: 10.1785/0120110096
Gao, X., & Wang, K. (2017). Rheological separation of the megathrust seismogenic zone and episodic tremor and slip. *Nature*, *543*(7645), 416–419. doi: https://doi.org/10.1038/nature21389
Ghosh, A., Vidale, J. E., Sweet, J. R., Creager, K. C., Wech, A. G., Houston, H.,

& Brodsky, E. E. (2010). Rapid, continuous streaking of tremor in cascadia. *Geochemistry, Geophysics, Geosystems*, *11*(12). Retrieved from https://agupubs.onlinelibrary.wiley.com/doi/abs/10.1029/2010GC003305 doi: https://doi.org/10.1029/2010GC003305

Gomberg, J., Wech, A., Creager, K., Obara, K., & Agnew, D. (2016). Reconsidering earthquake scaling. *Geophysical Research Letters*, *43*(12), 6243-6251. Retrieved from https://agupubs.onlinelibrary.wiley.com/doi/abs/10.1002/2016GL069967 doi: https://doi.org/10.1002/2016GL069967

Gosselin, J. M., Audet, P., Estève, C., McLellan, M., Mosher, S. G., & Schaeffer, A. J. (2020). Seismic evidence for megathrust fault-valve behavior during episodic tremor and slip. *Science Advances*, *6*(4), eaay5174. Retrieved from https://www.science.org/doi/abs/10.1126/sciadv.aay5174 doi: 10.1126/sciadv.aay5174

Gualandi, A., Serpelloni, E., & Belardinelli, M. E. (2016). Blind source separation problem in gps time series. *Journal of Geodesy*, *90*, 323–341. doi: 10.1007/s00190-015-0875-4

Hall, K., Schmidt, D., & Houston, H. (2019). Peak tremor rates lead peak slip rates during propagation of two large slow earthquakes in cascadia. *Geochemistry, Geophysics, Geosystems*, *20*(11), 4665-4675. Retrieved from https://agupubs.onlinelibrary.wiley.com/doi/abs/10.1029/2019GC008510 doi: https://doi.org/10.1029/2019GC008510

Hawthorne, J. C., Bostock, M. G., Royer, A. A., & Thomas, A. M. (2016). Variations in slow slip moment rate associated with rapid tremor reversals in cascadia. *Geochemistry, Geophysics, Geosystems*, *17*(12), 4899-4919. Retrieved from https://agupubs.onlinelibrary.wiley.com/doi/abs/10.1002/2016GC006489 doi: https://doi.org/10.1002/2016GC006489

Hayes, G. P., Moore, G. L., Portner, D. E., Hearne, M., Flamme, H., Furtney, M., & Smoczyk, G. M. (2018). Slab2, a comprehensive subduction zone geometry model. *Science*, *362*(6410), 58-61. Retrieved from https://www.science.org/doi/abs/10.1126/science.aat4723 doi: 10.1126/science.aat4723

Hetland, E. A., & Simons, M. (2010, 04). Post-seismic and interseismic fault creep II: transient creep and interseismic stress shadows on megathrusts. *Geophysical Journal International*, *181*(1), 99-112. Retrieved from https://doi.org/10.1111/j.1365-246X.2009.04482.x doi: 10.1111/j.1365-246X.2009.04482.x

Hirose, H., & Obara, K. (2005). Repeating short-and long-term slow slip events with deep tremor activity around the bungo channel region, southwest japan. *Earth, planets and space*, *57*, 961–972. doi: https://doi.org/10.1186/BF03351875

Houston, H. (2015). Low friction and fault weakening revealed by rising sensitivity of tremor to tidal stress. *Nature Geoscience*, *8*(5), 409–415.

Houston, H., Delbridge, B. G., Wech, A. G., & Creager, K. C. (2011). Rapid tremor reversals in cascadia generated by a weakened plate interface. *Nature Geoscience*, *4*(6), 404–409.

Ide, S. (2008). A brownian walk model for slow earthquakes. *Geophysical Research Letters*, *35*(17). Retrieved from https://agupubs.onlinelibrary.wiley.com/doi/abs/10.1029/2008GL034821 doi: https://doi.org/10.1029/2008GL034821

Ide, S. (2012). Variety and spatial heterogeneity of tectonic tremor worldwide. *Journal of Geophysical Research: Solid Earth*, *117*(B3). Retrieved from https://agupubs.onlinelibrary.wiley.com/doi/abs/10.1029/2011JB008840 doi: https://doi.org/10.1029/2011JB008840

Ide, S., & Beroza, G. C. (2023). Slow earthquake scaling reconsidered as a boundary between distinct modes of rupture propagation. *Proceedings of the National Academy of Sciences*, *120*(32), e2222102120. Retrieved from https://www.pnas.org/doi/abs/10.1073/pnas.2222102120 doi:

10.1073/pnas.2222102120
Ide, S., Beroza, G. C., Shelly, D. R., & Uchide, T. (2007). A scaling law for slow earthquakes. *Nature*, *447* (7140), 76–79. doi: https://doi.org/10.1038/nature05780
Ide, S., & Maury, J. (2018). Seismic moment, seismic energy, and source duration of slow earthquakes: Application of brownian slow earthquake model to three major subduction zones. *Geophysical Research Letters*, *45* (7), 3059-3067. Retrieved from https://agupubs.onlinelibrary.wiley.com/doi/abs/10.1002/2018GL077461 doi: https://doi.org/10.1002/2018GL077461
Ide, S., & Tanaka, Y. (2014). Controls on plate motion by oscillating tidal stress: Evidence from deep tremors in western japan. *Geophysical Research Letters*, *41* (11), 3842-3850. Retrieved from https://agupubs.onlinelibrary.wiley.com/doi/abs/10.1002/2014GL060035 doi: https://doi.org/10.1002/2014GL060035
Idehara, K., Yabe, S., & Ide, S. (2014). Regional and global variations in the temporal clustering of tectonic tremor activity. *Earth, Planets and Space*, *66* (1), 1–10.
Itaba, S., & Ando, R. (2011). A slow slip event triggered by teleseismic surface waves. *Geophysical Research Letters*, *38* (21). Retrieved from https://agupubs.onlinelibrary.wiley.com/doi/abs/10.1029/2011GL049593 doi: https://doi.org/10.1029/2011GL049593
Ito, Y., Obara, K., Shiomi, K., Sekine, S., & Hirose, H. (2007). Slow earthquakes coincident with episodic tremors and slow slip events. *Science*, *315* (5811), 503-506. Retrieved from https://www.science.org/doi/abs/10.1126/science.1134454 doi: 10.1126/science.1134454
Itoh, Y., & Aoki, Y. (2022). On the performance of position-domain sidereal filter for 30-s kinematic gps to mitigate multipath errors. *Earth, Planets and Space*, *74* (1), 1–20. doi: 10.1186/s40623-022-01584-8
Itoh, Y., Aoki, Y., & Fukuda, J. (2022). Imaging evolution of cascadia slow-slip event using high-rate gps. *Scientific reports*, *12* (1), 7179.
Itoh, Y., Socquet, A., & Radiguet, M. (2023). Largest aftershock nucleation driven by afterslip during the 2014 iquique sequence. *Geophysical Research Letters*, *50* (24), e2023GL104852. Retrieved from https://agupubs.onlinelibrary.wiley.com/doi/abs/10.1029/2023GL104852 (e2023GL104852 2023GL104852) doi: https://doi.org/10.1029/2023GL104852
Jara, J., Jolivet, R., Socquet, A., Comte, D., & Norabuena, E. (2024, Jun.). Detection of slow slip events along the southern peru - northern chile subduction zone. *Seismica*, *3* (1). Retrieved from https://seismica.library.mcgill.ca/article/view/980 doi: 10.26443/seismica.v3i1.980
Jolivet, R., & Frank, W. B. (2020). The transient and intermittent nature of slow slip. *AGU Advances*, *1* (1), e2019AV000126. Retrieved from https://agupubs.onlinelibrary.wiley.com/doi/abs/10.1029/2019AV000126 (e2019AV000126 10.1029/2019AV000126) doi: https://doi.org/10.1029/2019AV000126
Kao, H., Shan, S.-J., Dragert, H., Rogers, G., Cassidy, J. F., & Ramachandran, K. (2005). A wide depth distribution of seismic tremors along the northern cascadia margin. *Nature*, *436* (7052), 841–844. doi: https://doi.org/10.1038/nature03903
Katsumata, A., Miyaoka, K., Tsuyuki, T., Itaba, S., Tanaka, M., Ito, T., . . . Araya, A. (2024). Temporary slip speed increases during short-term slow slip events with durations of one to three hours. *Earth, Planets and Space*, *76* (1), 45. doi: https://doi.org/10.1186/s40623-024-01983-z
Kita, S., Houston, H., Yabe, S., Tanaka, S., Asano, Y., Shibutani, T., & Suda, N. (2021). Effects of episodic slow slip on seismicity and stress near a subduction-zone megathrust. *Nature Communications*, *12* (1), 7253. doi:

https://doi.org/10.1038/s41467-021-27453-8
Kositsky, A. P., & Avouac, J.-P. (2010). Inverting geodetic time series with a principal component analysis-based inversion method. *Journal of Geophysical Research: Solid Earth*, *115*(B3). Retrieved from https://agupubs.onlinelibrary.wiley.com/doi/abs/10.1029/2009JB006535 doi: https://doi.org/10.1029/2009JB006535
Kotowski, A. J., & Behr, W. M. (2019, 06). Length scales and types of heterogeneities along the deep subduction interface: Insights from exhumed rocks on Syros Island, Greece. *Geosphere*, *15*(4), 1038-1065. Retrieved from https://doi.org/10.1130/GES02037.1 doi: 10.1130/GES02037.1
Larson, K. M., Bilich, A., & Axelrad, P. (2007). Improving the precision of high-rate gps. *Journal of Geophysical Research: Solid Earth*, *112*(B5). doi: 10.1029/2006JB004367
Latour, S., Schubnel, A., Nielsen, S., Madariaga, R., & Vinciguerra, S. (2013). Characterization of nucleation during laboratory earthquakes. *Geophysical Research Letters*, *40*(19), 5064-5069. Retrieved from https://agupubs.onlinelibrary.wiley.com/doi/abs/10.1002/grl.50974 doi: https://doi.org/10.1002/grl.50974
Lavier, L. L., Tong, X., & Biemiller, J. (2021). The mechanics of creep, slow slip events, and earthquakes in mixed brittle-ductile fault zones. *Journal of Geophysical Research: Solid Earth*, *126*(2), e2020JB020325. Retrieved from https://agupubs.onlinelibrary.wiley.com/doi/abs/10.1029/2020JB020325 (e2020JB020325 2020JB020325) doi: https://doi.org/10.1029/2020JB020325
Liu, Y., & Rice, J. R. (2007). Spontaneous and triggered aseismic deformation transients in a subduction fault model. *Journal of Geophysical Research: Solid Earth*, *112*(B9). Retrieved from https://agupubs.onlinelibrary.wiley.com/doi/abs/10.1029/2007JB004930 doi: https://doi.org/10.1029/2007JB004930
Liu, Y., & Rice, J. R. (2009). Slow slip predictions based on granite and gabbro friction data compared to gps measurements in northern cascadia. *Journal of Geophysical Research: Solid Earth*, *114*(B9). Retrieved from https://agupubs.onlinelibrary.wiley.com/doi/abs/10.1029/2008JB006142 doi: https://doi.org/10.1029/2008JB006142
Luo, Y., & Liu, Z. (2019). Rate-and-state model casts new insight into episodic tremor and slow-slip variability in cascadia. *Geophysical Research Letters*, *46*(12), 6352-6362. Retrieved from https://agupubs.onlinelibrary.wiley.com/doi/abs/10.1029/2019GL082694 doi: https://doi.org/10.1029/2019GL082694
Luo, Y., & Liu, Z. (2021). Fault zone heterogeneities explain depth-dependent pattern and evolution of slow earthquakes in cascadia. *Nature Communications*, *12*(1), 1959. doi: https://doi.org/10.1038/s41467-021-22232-x
Marill, L., Marsan, D., Socquet, A., Radiguet, M., Cotte, N., & Rousset, B. (2021). Fourteen-Year Acceleration Along the Japan Trench. *Journal of Geophysical Research: Solid Earth*, *126*(11), e2020JB021226. doi: 10.1029/2020JB021226
McLaskey, G. C. (2019). Earthquake initiation from laboratory observations and implications for foreshocks. *Journal of Geophysical Research: Solid Earth*, *124*(12), 12882-12904. Retrieved from https://agupubs.onlinelibrary.wiley.com/doi/abs/10.1029/2019JB018363 doi: https://doi.org/10.1029/2019JB018363
Michel, S., Gualandi, A., & Avouac, J.-P. (2019, September). Interseismic Coupling and Slow Slip Events on the Cascadia Megathrust. *Pure and Applied Geophysics*, *176*(9), 3867-3891. doi: 10.1007/s00024-018-1991-x
Michel, S., Gualandi, A., & Avouac, J.-P. (2019). Similar scaling laws for earthquakes and cascadia slow-slip events. *Nature*, *574*(7779), 522–526. doi:

https://doi.org/10.1038/s41586-019-1673-6

Miyashita, T. (2020). *Dc3d.f90: January 14, 2020 release [software].* Retrieved from `https://github.com/hydrocoast/DC3D.f90`

Moutote, L., Itoh, Y., Lengliné, O., Duputel, Z., & Socquet, A. (2023). Evidence of a transient aseismic slip driving the 2017 valparaiso earthquake sequence, from foreshocks to aftershocks. *Journal of Geophysical Research: Solid Earth*, *128*(9), e2023JB026603. Retrieved from `https://agupubs.onlinelibrary.wiley.com/doi/abs/10.1029/2023JB026603` (e2023JB026603 2023JB026603) doi: https://doi.org/10.1029/2023JB026603

Nakajima, J., & Uchida, N. (2018). Repeated drainage from megathrusts during episodic slow slip. *Nature Geoscience*, *11*(5), 351–356. doi: https://doi.org/10.1038/s41561-018-0090-z

Nevada Geodetic Laboratory. (2024). *[dataset].* Retrieved from `http://geodesy.unr.edu/`

Nishimura, T., Matsuzawa, T., & Obara, K. (2013). Detection of short-term slow slip events along the nankai trough, southwest japan, using gnss data. *Journal of Geophysical Research: Solid Earth*, *118*(6), 3112-3125. Retrieved from `https://agupubs.onlinelibrary.wiley.com/doi/abs/10.1002/jgrb.50222` doi: https://doi.org/10.1002/jgrb.50222

Noda, H., Nakatani, M., & Hori, T. (2013). Large nucleation before large earthquakes is sometimes skipped due to cascade-up—implications from a rate and state simulation of faults with hierarchical asperities. *Journal of Geophysical Research: Solid Earth*, *118*(6), 2924-2952. Retrieved from `https://agupubs.onlinelibrary.wiley.com/doi/abs/10.1002/jgrb.50211` doi: https://doi.org/10.1002/jgrb.50211

Obara, K. (2002). Nonvolcanic deep tremor associated with subduction in southwest japan. *Science*, *296*(5573), 1679-1681. Retrieved from `https://www.science.org/doi/abs/10.1126/science.1070378` doi: 10.1126/science.1070378

Obara, K., & Kato, A. (2016). Connecting slow earthquakes to huge earthquakes. *Science*, *353*(6296), 253-257. Retrieved from `https://www.science.org/doi/abs/10.1126/science.aaf1512` doi: 10.1126/science.aaf1512

Oikawa, G., & Aso, N. (2024, 01). Cubic moment–duration relationship of low-frequency earthquakes. *Geophysical Journal International*, *237*(1), 90-108. Retrieved from `https://doi.org/10.1093/gji/ggae031` doi: 10.1093/gji/ggae031

Okada, Y. (1985, 08). Surface deformation due to shear and tensile faults in a half-space. *Bulletin of the Seismological Society of America*, *75*(4), 1135-1154. Retrieved from `https://doi.org/10.1785/BSSA0750041135` doi: 10.1785/BSSA0750041135

Okada, Y., Nishimura, T., Tabei, T., Matsushima, T., & Hirose, H. (2022). Development of a detection method for short-term slow slip events using gnss data and its application to the nankai subduction zone. *Earth, Planets and Space*, *74*(1), 1–18.

Pacific Northwest Seismic Network. (2024). *[dataset].* Retrieved from `https://pnsn.org/tremor`

Peng, Z., & Gomberg, J. (2010). An integrated perspective of the continuum between earthquakes and slow-slip phenomena. *Nature geoscience*, *3*(9), 599–607. doi: https://doi.org/10.1038/ngeo940

Radiguet, M., Cotton, F., Vergnolle, M., Campillo, M., Valette, B., Kostoglodov, V., & Cotte, N. (2011, 02). Spatial and temporal evolution of a long term slow slip event: the 2006 Guerrero Slow Slip Event. *Geophysical Journal International*, *184*(2), 816-828. Retrieved from `https://doi.org/10.1111/j.1365-246X.2010.04866.x` doi: 10.1111/j.1365-246X.2010.04866.x

Ragheb, A., Clarke, P. J., & Edwards, S. (2007). Gps sidereal filtering: coordinate- and carrier-phase-level strategies. *Journal of Geodesy*, *81*(5), 325–335. doi: 10

.1007/s00190-006-0113-1
Rogers, G., & Dragert, H. (2003). Episodic tremor and slip on the cascadia subduction zone: The chatter of silent slip. *Science*, *300*(5627), 1942-1943. Retrieved from https://www.science.org/doi/abs/10.1126/science.1084783 doi: 10.1126/science.1084783
Rousset, B., Campillo, M., Lasserre, C., Frank, W. B., Cotte, N., Walpersdorf, A., . . . Kostoglodov, V. (2017). A geodetic matched filter search for slow slip with application to the mexico subduction zone. *Journal of Geophysical Research: Solid Earth*, *122*(12), 10,498-10,514. Retrieved from https://agupubs.onlinelibrary.wiley.com/doi/abs/10.1002/2017JB014448 doi: https://doi.org/10.1002/2017JB014448
Royer, A., & Bostock, M. (2014). A comparative study of low frequency earthquake templates in northern cascadia. *Earth and Planetary Science Letters*, *402*, 247-256. Retrieved from https://www.sciencedirect.com/science/article/pii/S0012821X13004780 (Special issue on USArray science) doi: https://doi.org/10.1016/j.epsl.2013.08.040
Rubin, A. M., & Armbruster, J. G. (2013). Imaging slow slip fronts in cascadia with high precision cross-station tremor locations. *Geochemistry, Geophysics, Geosystems*, *14*(12), 5371-5392. Retrieved from https://agupubs.onlinelibrary.wiley.com/doi/abs/10.1002/2013GC005031 doi: https://doi.org/10.1002/2013GC005031
Rubinstein, J. L., Gomberg, J., Vidale, J. E., Wech, A. G., Kao, H., Creager, K. C., & Rogers, G. (2009). Seismic wave triggering of nonvolcanic tremor, episodic tremor and slip, and earthquakes on vancouver island. *Journal of Geophysical Research: Solid Earth*, *114*(B2). Retrieved from https://agupubs.onlinelibrary.wiley.com/doi/abs/10.1029/2008JB005875 doi: https://doi.org/10.1029/2008JB005875
Rubinstein, J. L., Vidale, J. E., Gomberg, J., Bodin, P., Creager, K. C., & Malone, S. D. (2007). Non-volcanic tremor driven by large transient shear stresses. *Nature*, *448*(7153), 579–582. doi: https://doi.org/10.1038/nature06017
Saux, J. P., Molitors Bergman, E. G., Evans, E. L., & Loveless, J. P. (2022). The role of slow slip events in the cascadia subduction zone earthquake cycle. *Journal of Geophysical Research: Solid Earth*, *127*(2), e2021JB022425. Retrieved from https://agupubs.onlinelibrary.wiley.com/doi/abs/10.1029/2021JB022425 (e2021JB022425 2021JB022425) doi: https://doi.org/10.1029/2021JB022425
Schmidt, D. A., & Gao, H. (2010). Source parameters and time-dependent slip distributions of slow slip events on the cascadia subduction zone from 1998 to 2008. *Journal of Geophysical Research: Solid Earth*, *115*(B4). Retrieved from https://agupubs.onlinelibrary.wiley.com/doi/abs/10.1029/2008JB006045 doi: https://doi.org/10.1029/2008JB006045
Scholz, C. H. (1998). Earthquakes and friction laws. *Nature*, *391*(6662), 37–42. doi: https://doi.org/10.1038/34097
Segall, P., & Matthews, M. (1997). Time dependent inversion of geodetic data. *Journal of Geophysical Research: Solid Earth*, *102*(B10), 22391-22409. Retrieved from https://agupubs.onlinelibrary.wiley.com/doi/abs/10.1029/97JB01795 doi: https://doi.org/10.1029/97JB01795
Shapiro, N. M., Campillo, M., Kaminski, E., Vilotte, J.-P., & Jaupart, C. (2018). Low-frequency earthquakes and pore pressure transients in subduction zones. *Geophysical Research Letters*, *45*(20), 11,083-11,094. Retrieved from https://agupubs.onlinelibrary.wiley.com/doi/abs/10.1029/2018GL079893 doi: https://doi.org/10.1029/2018GL079893
Shelly, D. R., Beroza, G. C., & Ide, S. (2007). Non-volcanic tremor and low-frequency earthquake swarms. *Nature*, *446*(7133), 305–307. doi: https://doi.org/10.1038/nature05666

Shelly, D. R., Beroza, G. C., Ide, S., & Nakamula, S. (2006). Low-frequency earthquakes in shikoku, japan, and their relationship to episodic tremor and slip. *Nature*, *442*(7099), 188–191. doi: https://doi.org/10.1038/nature04931

Supino, M., Poiata, N., Festa, G., Vilotte, J., Satriano, C., & Obara, K. (2020, Apr). Self-similarity of low-frequency earthquakes. *Scientific Reports*, *10*(1). doi: 10.1038/s41598-020-63584-6

Sweet, J. R., Creager, K. C., & Houston, H. (2014). A family of repeating low-frequency earthquakes at the downdip edge of tremor and slip. *Geochemistry, Geophysics, Geosystems*, *15*(9), 3713-3721. Retrieved from `https://agupubs.onlinelibrary.wiley.com/doi/abs/10.1002/2014GC005449` doi: https://doi.org/10.1002/2014GC005449

Sweet, J. R., Creager, K. C., Houston, H., & Chestler, S. R. (2019). Variations in cascadia low-frequency earthquake behavior with downdip distance. *Geochemistry, Geophysics, Geosystems*, *20*(2), 1202-1217. Retrieved from `https://agupubs.onlinelibrary.wiley.com/doi/abs/10.1029/2018GC007998` doi: https://doi.org/10.1029/2018GC007998

Tulley, C. J., Fagereng, A., Ujiie, K., Diener, J. F. A., & Harris, C. (2022). Embrittlement within viscous shear zones across the base of the subduction thrust seismogenic zone. *Geochemistry, Geophysics, Geosystems*, *23*(9), e2021GC010208. Retrieved from `https://agupubs.onlinelibrary.wiley.com/doi/abs/10.1029/2021GC010208` (e2021GC010208 2021GC010208) doi: https://doi.org/10.1029/2021GC010208

Twardzik, C., Vergnolle, M., Sladen, A., & Avallone, A. (2019). Unravelling the contribution of early postseismic deformation using sub-daily gnss positioning. *Scientific reports*, *9*(1), 1775. doi: https://doi.org/10.1038/s41598-019-39038-z

Ujiie, K., Saishu, H., Fagereng, A., Nishiyama, N., Otsubo, M., Masuyama, H., & Kagi, H. (2018). An explanation of episodic tremor and slow slip constrained by crack-seal veins and viscous shear in subduction mélange. *Geophysical Research Letters*, *45*(11), 5371-5379. Retrieved from `https://agupubs.onlinelibrary.wiley.com/doi/abs/10.1029/2018GL078374` doi: https://doi.org/10.1029/2018GL078374

Warren-Smith, E., Fry, B., Wallace, L., Chon, E., Henrys, S., Sheehan, A., ... Lebedev, S. (2019). Episodic stress and fluid pressure cycling in subducting oceanic crust during slow slip. *Nature Geoscience*, *12*(6), 475–481. doi: https://doi.org/10.1038/s41561-019-0367-x

Wdowinski, S., Bock, Y., Zhang, J., Fang, P., & Genrich, J. (1997). Southern california permanent gps geodetic array: Spatial filtering of daily positions for estimating coseismic and postseismic displacements induced by the 1992 landers earthquake. *Journal of Geophysical Research: Solid Earth*, *102*(B8), 18057-18070. doi: 10.1029/97JB01378

Wech, A. G. (2021). Cataloging tectonic tremor energy radiation in the cascadia subduction zone. *Journal of Geophysical Research: Solid Earth*, *126*(10), e2021JB022523. Retrieved from `https://agupubs.onlinelibrary.wiley.com/doi/abs/10.1029/2021JB022523` doi: https://doi.org/10.1029/2021JB022523

Wech, A. G., & Bartlow, N. M. (2014). Slip rate and tremor genesis in cascadia. *Geophysical Research Letters*, *41*(2), 392-398. Retrieved from `https://agupubs.onlinelibrary.wiley.com/doi/abs/10.1002/2013GL058607` doi: https://doi.org/10.1002/2013GL058607

Wech, A. G., & Creager, K. C. (2011). A continuum of stress, strength and slip in the cascadia subduction zone. *Nature Geoscience*, *4*(9), 624–628. doi: https://doi.org/10.1038/ngeo1215

World Tremor DataBase. (2024). *[dataset].* Retrieved from `http://www-solid.eps.s.u-tokyo.ac.jp/~idehara/wtd0/Welcome.html`

Wu, B. (2021). Explaining slow earthquake phenomena with a frictional-viscous faulting model. *ProQuest Dissertations and Theses*, 255. Retrieved from https://www.proquest.com/dissertations-theses/explaining-slow-earthquake-phenomena-with/docview/2638699203/se-2 (Copyright - Database copyright ProQuest LLC; ProQuest does not claim copyright in the individual underlying works; Last updated - 2024-03-19)

Yabe, S., & Ide, S. (2014). Spatial distribution of seismic energy rate of tectonic tremors in subduction zones. *Journal of Geophysical Research: Solid Earth*, *119*(11), 8171-8185. Retrieved from https://agupubs.onlinelibrary.wiley.com/doi/abs/10.1002/2014JB011383 doi: https://doi.org/10.1002/2014JB011383

Yabe, S., Ochi, T., Matsumoto, N., Itaba, S., Kitagawa, Y., & Matsuzawa, T. (2023). Eight-year catalog of deep short-term slow slip events at the nankai trough based on objective detection algorithm using strain and tilt records. *Earth, Planets and Space*, *75*(1), 1–21.

Yabe, S., Tanaka, Y., Houston, H., & Ide, S. (2015). Tidal sensitivity of tectonic tremors in nankai and cascadia subduction zones. *Journal of Geophysical Research: Solid Earth*, *120*(11), 7587-7605. Retrieved from https://agupubs.onlinelibrary.wiley.com/doi/abs/10.1002/2015JB012250 doi: https://doi.org/10.1002/2015JB012250

Zhang, L., Huang, D., Shum, C. K., & Guo, R. (2023). The 2019 east coast slow slip event, new zealand: Spatiotemporal evolution and associated seismicity. *Marine Geodesy*, *46*(3), 195–215. Retrieved from https://doi.org/10.1080/01490419.2022.2141931 doi: 10.1080/01490419.2022.2141931

References in Supplementary Information

Altamimi, Z., Métivier, L., Rebischung, P., Rouby, H., & Collilieux, X. (2017, 03). ITRF2014 plate motion model. *Geophysical Journal International*, *209*(3), 1906-1912. Retrieved from https://doi.org/10.1093/gji/ggx136 doi: 10.1093/gji/ggx136

Bartlow, N. M. (2020). A long-term view of episodic tremor and slip in cascadia. *Geophysical Research Letters*, *47*(3), e2019GL085303. Retrieved from https://agupubs.onlinelibrary.wiley.com/doi/abs/10.1029/2019GL085303 (e2019GL085303 10.1029/2019GL085303) doi: https://doi.org/10.1029/2019GL085303

Bletery, Q., & Nocquet, J.-M. (2023). The precursory phase of large earthquakes. *Science*, *381*(6655), 297-301. Retrieved from https://www.science.org/doi/abs/10.1126/science.adg2565 doi: 10.1126/science.adg2565

Blewitt, G., Hammond, W. C., & Kreemer, C. (2018). Harnessing the gps data explosion for interdisciplinary science. *EOS*, *99*. doi: 10.1029/2018EO104623

Choi, K., Bilich, A., Larson, K. M., & Axelrad, P. (2004). Modified sidereal filtering: Implications for high-rate gps positioning. *Geophysical Research Letters*, *31*(22). doi: 10.1029/2004GL021621

Cleveland, R. B., Cleveland, W. S., McRae, J. E., & Terpenning, I. (1990). Stl: A seasonal-trend decomposition. *J. Off. Stat*, *6*(1), 3–73.

Costantino, G., Giffard-Roisin, S., Radiguet, M., Dalla Mura, M., Marsan, D., & Socquet, A. (2023). Multi-station deep learning on geodetic time series detects slow slip events in cascadia. *Communications Earth & Environment*, *4*(1), 435. doi: 10.1038/s43247-023-01107-7

Hayes, G. (2018, Aug). *A comprehensive subduction zone geometry model.* Retrieved from https://doi.org/10.5066/F7PV6JNV

Hayes, G. P., Moore, G. L., Portner, D. E., Hearne, M., Flamme, H., Furtney, M., & Smoczyk, G. M. (2018). Slab2, a comprehensive subduction zone geometry model. *Science*, *362*(6410), 58-61. Retrieved from https://www.science.org/

doi/abs/10.1126/science.aat4723 doi: 10.1126/science.aat4723
Houston, H. (2015). Low friction and fault weakening revealed by rising sensitivity of tremor to tidal stress. *Nature Geoscience*, *8*(5), 409–415.
Houston, H., Delbridge, B. G., Wech, A. G., & Creager, K. C. (2011). Rapid tremor reversals in cascadia generated by a weakened plate interface. *Nature Geoscience*, *4*(6), 404–409.
Itoh, Y., & Aoki, Y. (2022). On the performance of position-domain sidereal filter for 30-s kinematic gps to mitigate multipath errors. *Earth, Planets and Space*, *74*(1), 1–20. doi: 10.1186/s40623-022-01584-8
Itoh, Y., Aoki, Y., & Fukuda, J. (2022). Imaging evolution of cascadia slow-slip event using high-rate gps. *Scientific reports*, *12*(1), 7179.
Itoh, Y., Socquet, A., & Radiguet, M. (2023). Largest aftershock nucleation driven by afterslip during the 2014 iquique sequence. *Geophysical Research Letters*, *50*(24), e2023GL104852. Retrieved from https://agupubs.onlinelibrary.wiley.com/doi/abs/10.1029/2023GL104852 (e2023GL104852 2023GL104852) doi: https://doi.org/10.1029/2023GL104852
Jara, J., Jolivet, R., Socquet, A., Comte, D., & Norabuena, E. (2024, Jun.). Detection of slow slip events along the southern peru - northern chile subduction zone. *Seismica*, *3*(1). Retrieved from https://seismica.library.mcgill.ca/article/view/980 doi: 10.26443/seismica.v3i1.980
Larson, K. M., Bilich, A., & Axelrad, P. (2007). Improving the precision of high-rate gps. *Journal of Geophysical Research: Solid Earth*, *112*(B5). doi: 10.1029/2006JB004367
Li, S., Wang, K., Wang, Y., Jiang, Y., & Dosso, S. E. (2018). Geodetically inferred locking state of the cascadia megathrust based on a viscoelastic earth model. *Journal of Geophysical Research: Solid Earth*, *123*(9), 8056-8072. Retrieved from https://agupubs.onlinelibrary.wiley.com/doi/abs/10.1029/2018JB015620 doi: https://doi.org/10.1029/2018JB015620
Marill, L., Marsan, D., Socquet, A., Radiguet, M., Cotte, N., & Rousset, B. (2021). Fourteen-Year Acceleration Along the Japan Trench. *Journal of Geophysical Research: Solid Earth*, *126*(11), e2020JB021226. doi: 10.1029/2020JB021226
McCaffrey, R., Qamar, A. I., King, R. W., Wells, R., Khazaradze, G., Williams, C. A., ... Zwick, P. C. (2007, 06). Fault locking, block rotation and crustal deformation in the Pacific Northwest. *Geophysical Journal International*, *169*(3), 1315-1340. Retrieved from https://doi.org/10.1111/j.1365-246X.2007.03371.x doi: 10.1111/j.1365-246X.2007.03371.x
Michel, S., Gualandi, A., & Avouac, J.-P. (2019, September). Interseismic Coupling and Slow Slip Events on the Cascadia Megathrust. *Pure and Applied Geophysics*, *176*(9), 3867-3891. doi: 10.1007/s00024-018-1991-x
Moutote, L., Itoh, Y., Lengliné, O., Duputel, Z., & Socquet, A. (2023). Evidence of a transient aseismic slip driving the 2017 valparaiso earthquake sequence, from foreshocks to aftershocks. *Journal of Geophysical Research: Solid Earth*, *128*(9), e2023JB026603. Retrieved from https://agupubs.onlinelibrary.wiley.com/doi/abs/10.1029/2023JB026603 (e2023JB026603 2023JB026603) doi: https://doi.org/10.1029/2023JB026603
Okada, Y. (1985, 08). Surface deformation due to shear and tensile faults in a half-space. *Bulletin of the Seismological Society of America*, *75*(4), 1135-1154. Retrieved from https://doi.org/10.1785/BSSA0750041135 doi: 10.1785/BSSA0750041135
Okada, Y., Nishimura, T., Tabei, T., Matsushima, T., & Hirose, H. (2022). Development of a detection method for short-term slow slip events using gnss data and its application to the nankai subduction zone. *Earth, Planets and Space*, *74*(1), 1–18.
Pedregosa, F., Varoquaux, G., Gramfort, A., Michel, V., Thirion, B., Grisel, O., ... others (2011). Scikit-learn: Machine learning in python. *the Journal of*

machine Learning research, *12*, 2825–2830.
Ragheb, A., Clarke, P. J., & Edwards, S. (2007). Gps sidereal filtering: coordinate- and carrier-phase-level strategies. *Journal of Geodesy*, *81*(5), 325–335. doi: 10.1007/s00190-006-0113-1
Rousset, B., Campillo, M., Lasserre, C., Frank, W. B., Cotte, N., Walpersdorf, A., … Kostoglodov, V. (2017). A geodetic matched filter search for slow slip with application to the mexico subduction zone. *Journal of Geophysical Research: Solid Earth*, *122*(12), 10,498-10,514. Retrieved from `https://agupubs.onlinelibrary.wiley.com/doi/abs/10.1002/2017JB014448` doi: https://doi.org/10.1002/2017JB014448
Schmalzle, G. M., McCaffrey, R., & Creager, K. C. (2014). Central cascadia subduction zone creep. *Geochemistry, Geophysics, Geosystems*, *15*(4), 1515-1532. Retrieved from `https://agupubs.onlinelibrary.wiley.com/doi/abs/10.1002/2013GC005172` doi: https://doi.org/10.1002/2013GC005172
Wdowinski, S., Bock, Y., Zhang, J., Fang, P., & Genrich, J. (1997). Southern california permanent gps geodetic array: Spatial filtering of daily positions for estimating coseismic and postseismic displacements induced by the 1992 landers earthquake. *Journal of Geophysical Research: Solid Earth*, *102*(B8), 18057-18070. doi: 10.1029/97JB01378
Wech, A. G. (2021). Cataloging tectonic tremor energy radiation in the cascadia subduction zone. *Journal of Geophysical Research: Solid Earth*, *126*(10), e2021JB022523. Retrieved from `https://agupubs.onlinelibrary.wiley.com/doi/abs/10.1029/2021JB022523` doi: https://doi.org/10.1029/2021JB022523

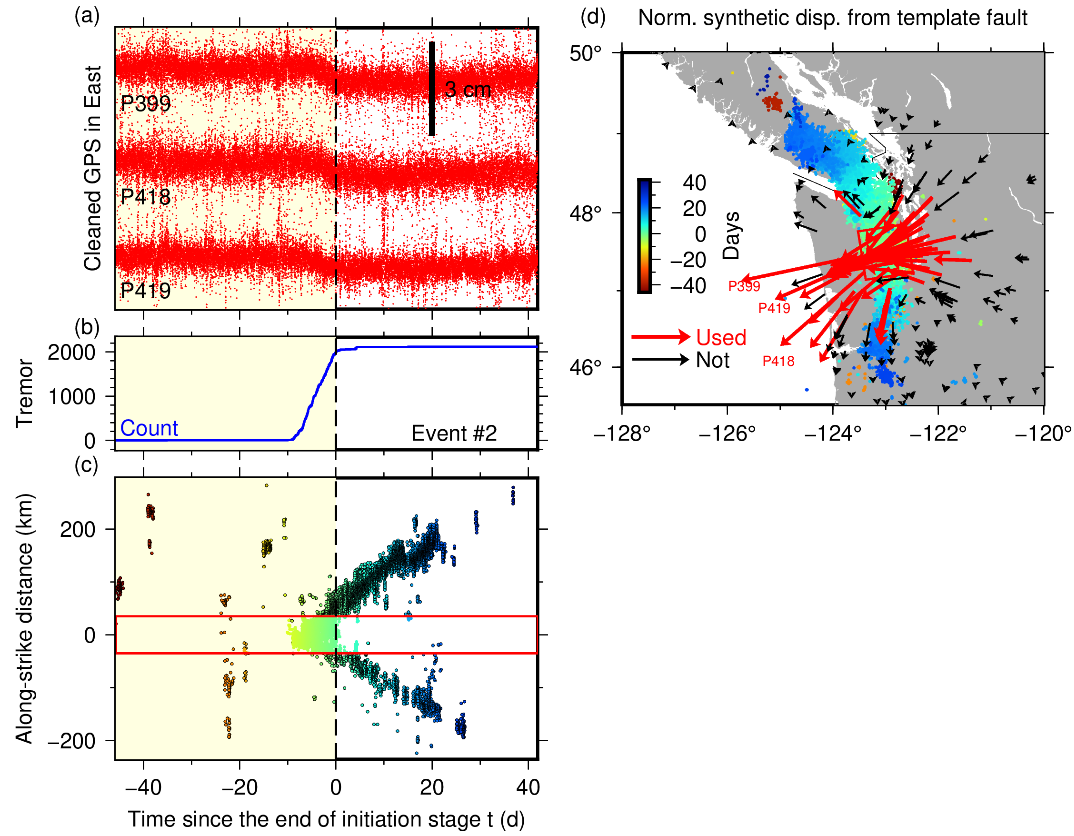

Figure 1. An example of major Cascadia ETSs analyzed in this study (Event #2; Table 1). (a) Examples of the east component of cleaned sub-daily GPS time series (site name labeled and location in (d)). Yellow background highlights the time range toward the end of the initiation stage of the ETS studied here. (b) Cumulative tremor counts in the initiation zone (red rectangle in (c-d)). (c) Time evolution of tremor location in the along-strike direction (dots). Dots without and with the outline are those inside and outside the initiation zone, respectively. The red lines indicate the along-strike range of the initiation zone. (d) Tremor distribution color-coded with time. Red rectangle indicates a template fault to compute surface displacements (vectors) used to weight time series at each site for stacking ($\mathbf{w}_i^e$). Only vectors in red are used for stacking $b = 0.3$ (See Text S1). Plots for other events are shown as Figures S1-S12

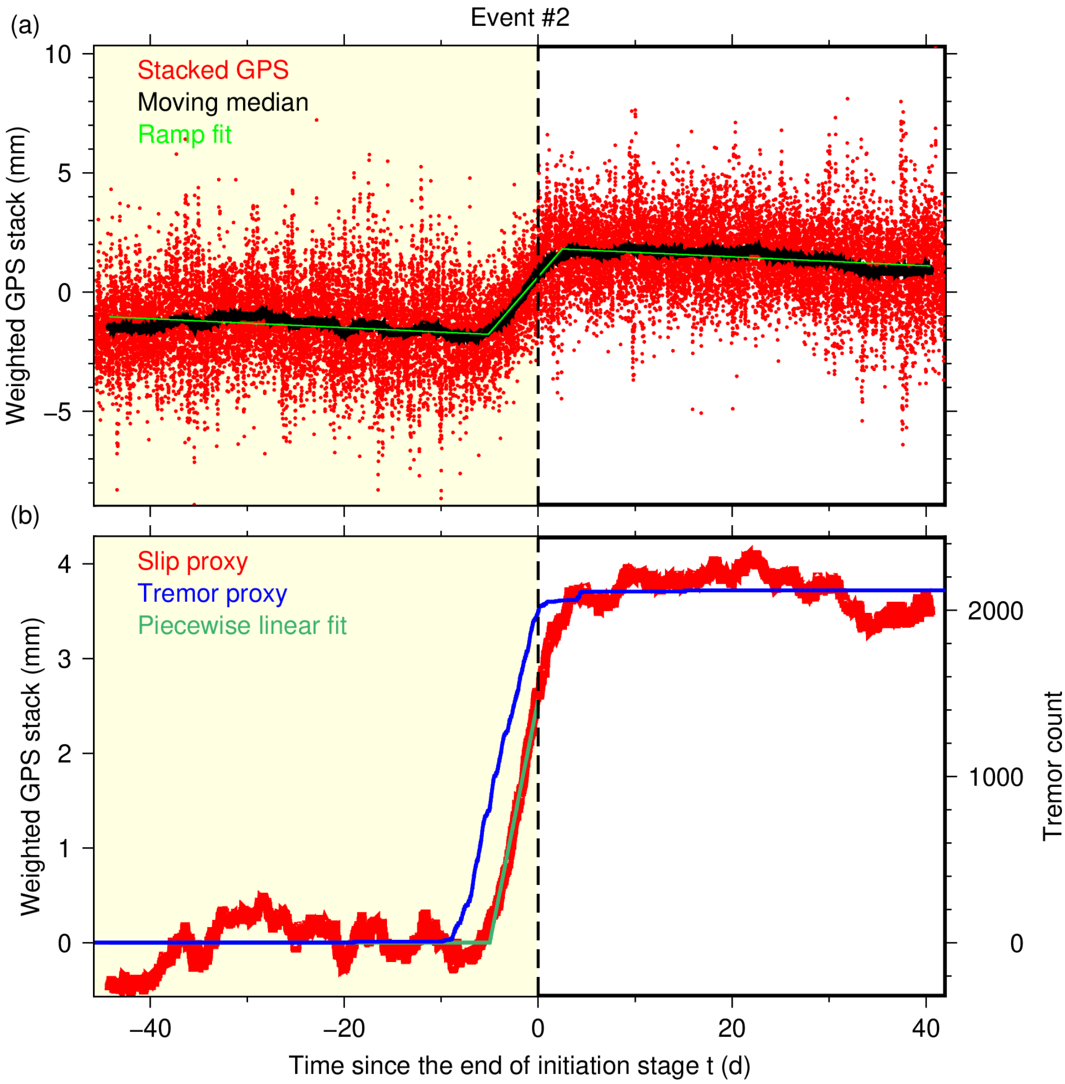

Figure 2. An example of sub-daily GPS stack (Event #2). (a) Stacked GPS (red dots), their moving median (black curve, window length = 3 days), and a ramp function fit to the moving median to remove the local linear trend (green; Text S1). (b) Detrended moving median of sub-daily GPS stack (slip proxy; red), piecewise-linear fit to it (green; data at $t \leq 0$ is used), and cumulative tremor count (tremor proxy; blue). Plots for other events are shown in Figures S14-S25.

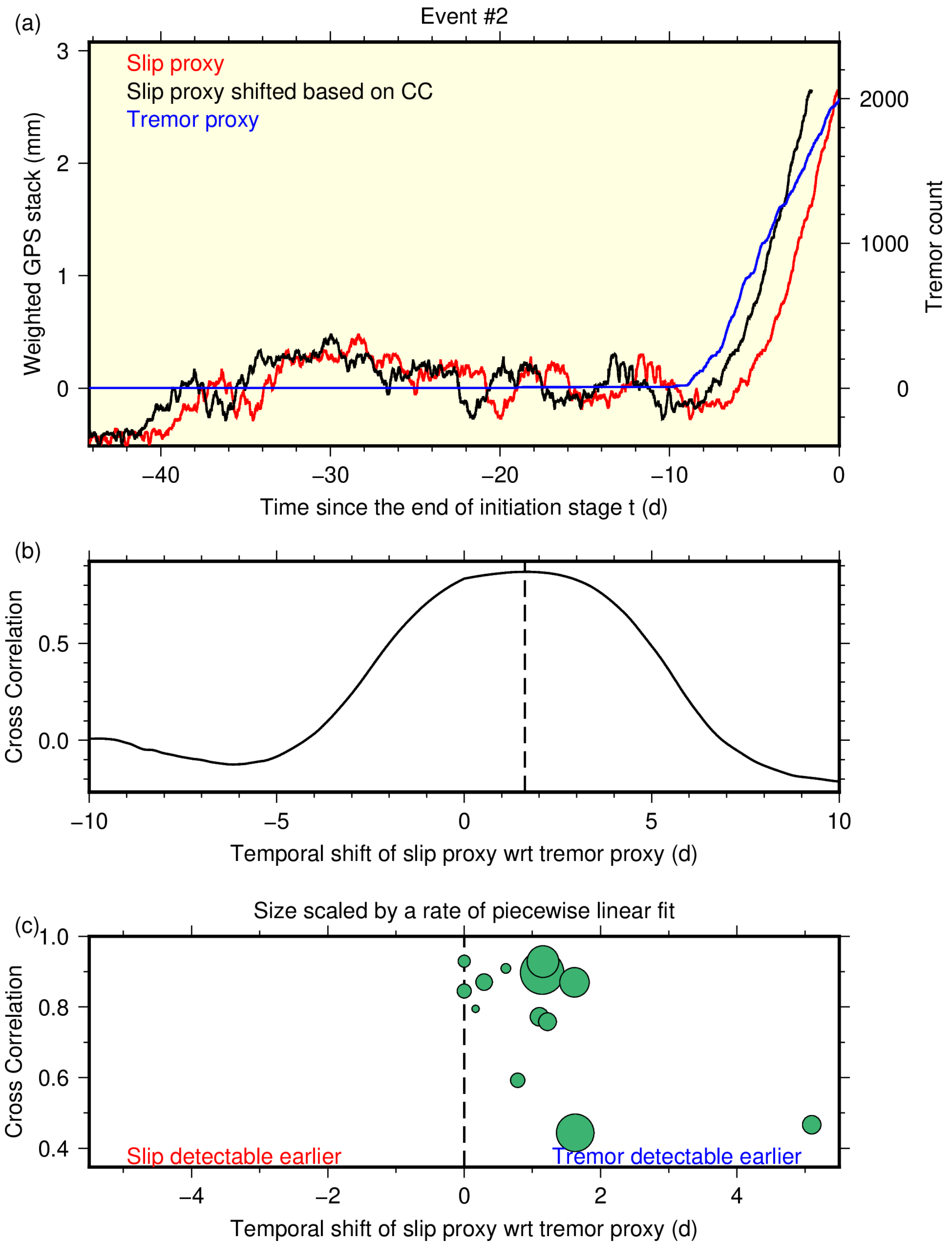

Figure 3. Cross correlation (CC) analysis. (a) Comparison of slip (red) and tremor (blue) proxies as well as slip proxy shifted by the lag measured by CC (black). (b) CC values with different temporal shifts of slip proxy. The vertical broken line indicates the delay which maximizes CC. (c) Compilation of temporal shift and corresponding CC for all the events (green dots). Dot size is scaled by a rate of the second section of the piecewise linear fit to the slip proxy (Figures 2b, 4a, S14b-S25b, and Section 3.3) which approximates signal to noise ratio of the slip proxy.

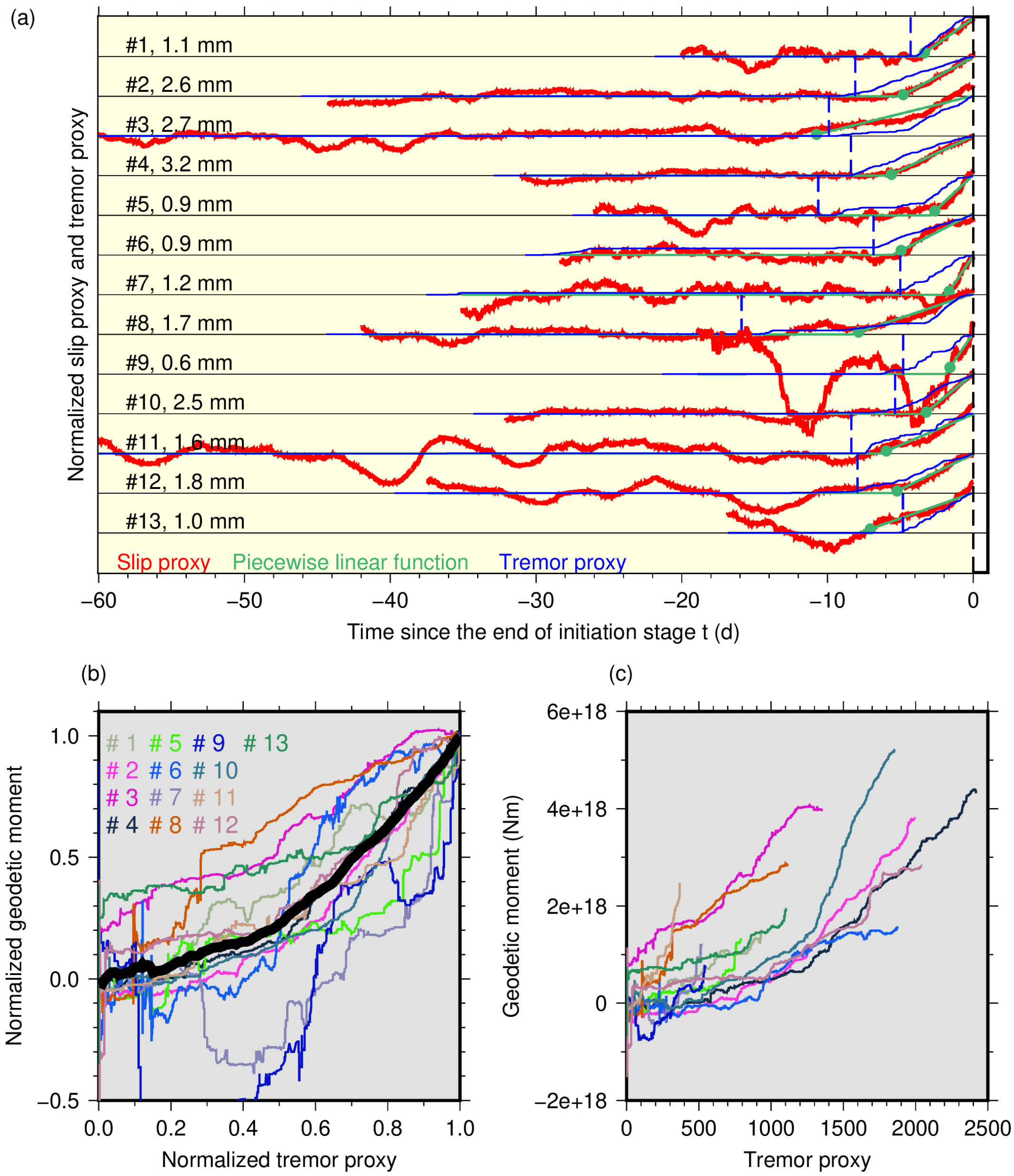

Figure 4. (a) GPS stacks for all the events (red; slip proxy), piece-wise linear fit to them (green), and cumulative tremor count (blue; tremor proxy) until the end of the initiation stage. Event # (Table 1) and corresponding amplitudes of stack displacement are labeled. Each GPS stack and corresponding piece-wise linear fit are normalized by the amplitude. Each cumulative tremor count is normalized by its value at the end of the initiation stage ($t = 0$). The green dot indicates the SSE moment onset time $t = T_e^{sb}$ while the blue vertical dotted line indicates the tremor onset time $t = T_e^{tb}$ (Figure S28). (b) Evolution of geodetic SSE moment (slip proxy) with respect to tremor count (tremor proxy) for each event (color), both of which are normalized by their respective final values for each event. Thick black curves indicate a weighted stack of the normalized curves. (c) Same as (b) but with both axes not normalized.

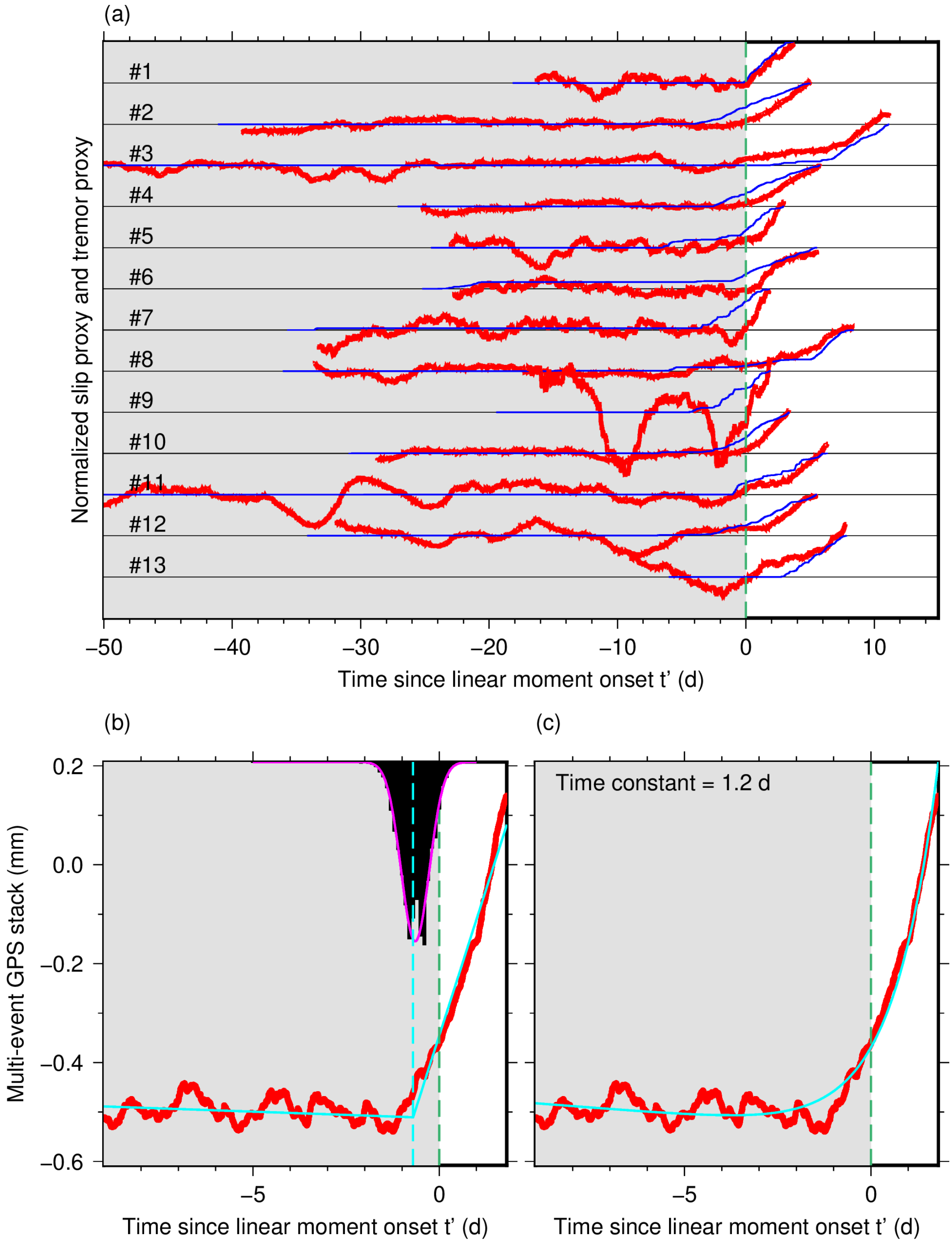

Figure 5. Multi-event GPS stack. (a) Same as Figure 4, but with the new t' time axis (Section 3.3) after shifting the time axis of the original stacks by the onset of linear moment release time. The green vertical line corresponds to $t = T_e^{sb}$ (green dot in Figure 4). Gray background indicates the period during which the clear moment release is not identified by the piecewise linear fit to the multi-site stack for each individual event. (b-c) Multi-event stack result (red) with its piece-wise linear fit (aqua). Black histogram and pink Gaussian curve fit in (b) indicate a bootstrap test result for the estimated time of the kink T_{mb} indicated as the broken line in aqua. (c) Same as (b) but with an exponential fit with the equation of $d(t') = c_6 + c_7 t' + c_8 \exp(-\frac{t'-T_m}{\tau_{exp}})$, where c_6, c_7, c_8 are the coefficient of each term, τ_{exp} is the time constant as labeled in (c). Refer to Section 3.3 for the other variables.

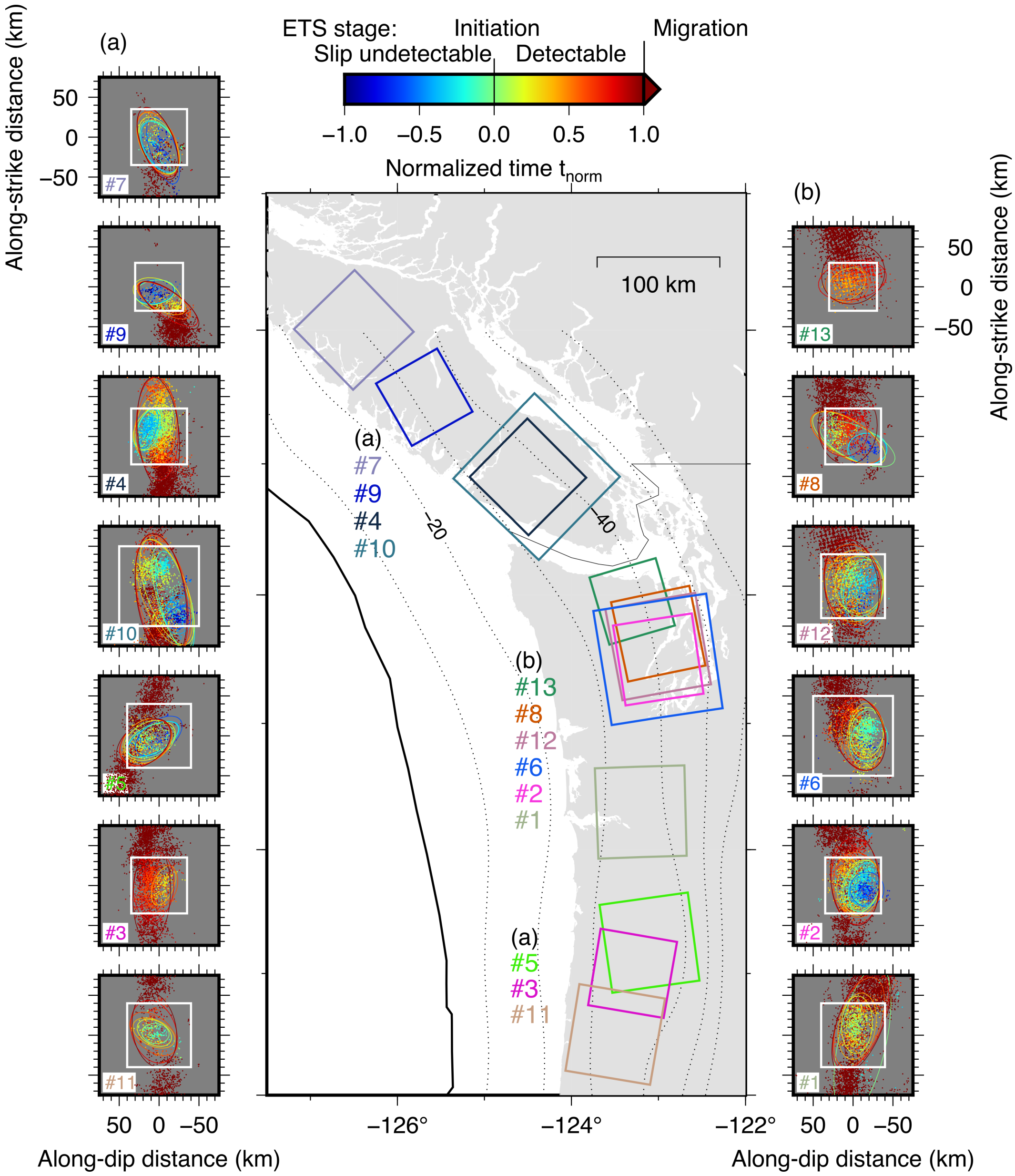

Figure 6. Map view of ETS initiation zones as template faults for GPS stack (colored rectangles in the map) with associated tremors (colored dots). (a-b) Tremor distribution color-coded by normalized time t_{norm} (Equation (4)). Colored ellipses indicate ellipsoidal areas enclosing about 95% of tremors by the time since $t_{norm} = -1$. White rectangles indicate the area of the template faults for each event.

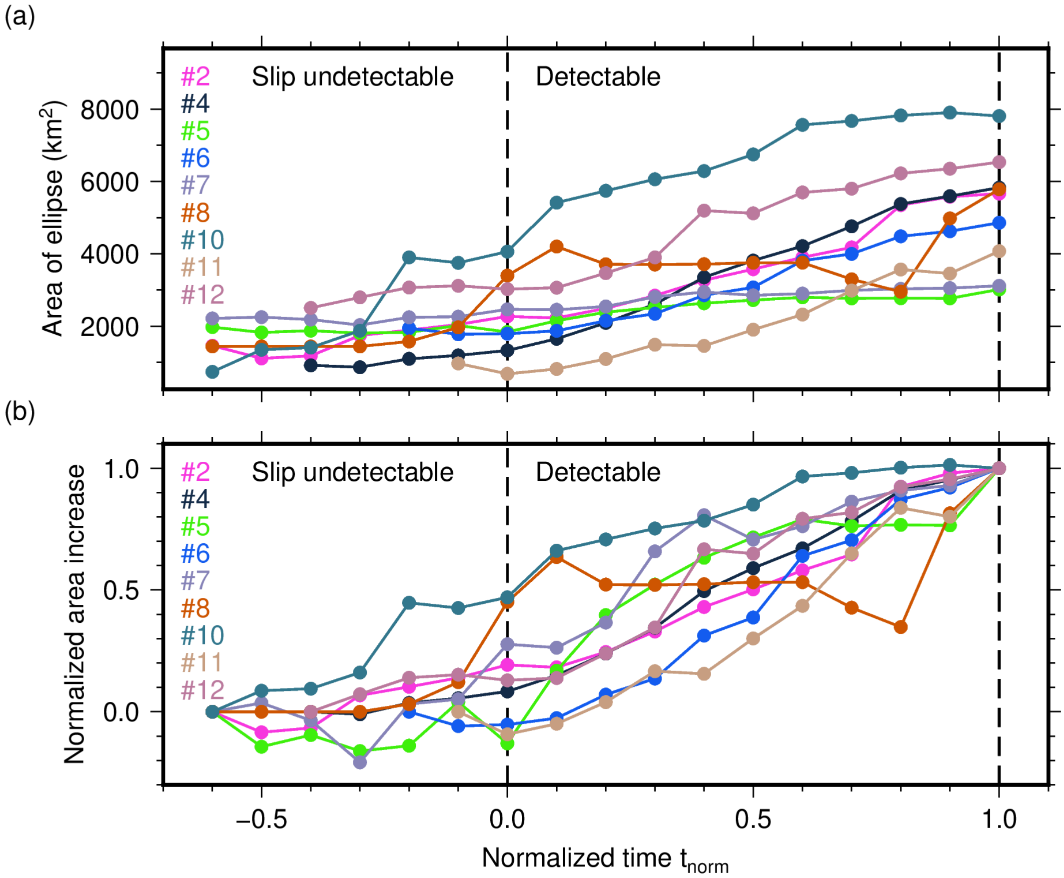

Figure 7. (a) Area of ellipse enclosing 95% of tremor epicenters $A_e(t_{norm})$ for each ETS initiation event a function of time t_{norm} (Figure 6). Tremors shown in Figure 6 are considered for the calculation and those at $t_{norm} < -1$ are excluded. (b) Normalized atea increase $\Delta A_e(t_{norm})$ (Equation (5)).

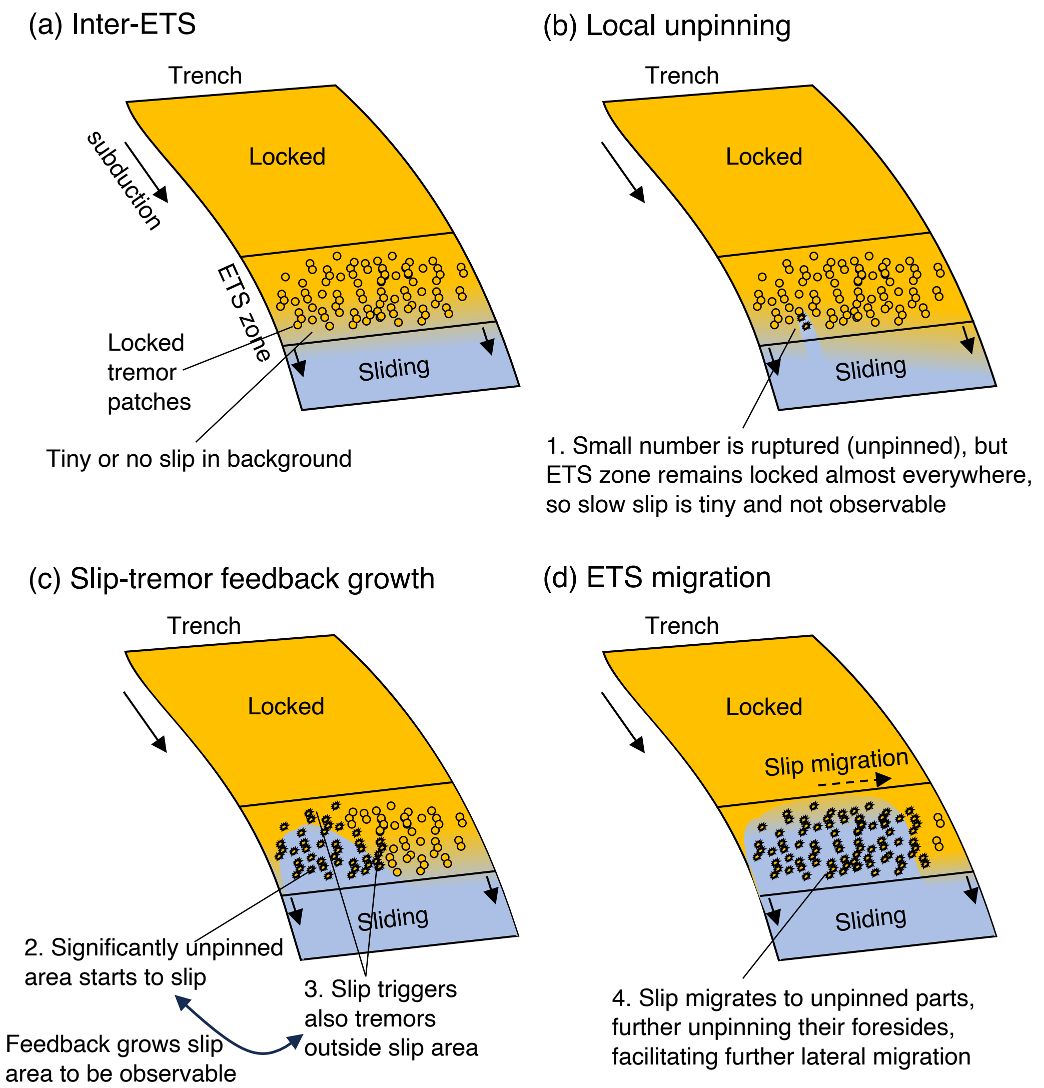

Figure 8. Sketch of the conceptual model we propose as a mechanism for ETS initiation in Cascadia. Tremor patches are a relatively strong portion of the locked interface, and their removal facilitates the SSE growth. A unilateral migration case is drawn for visual clarity, but the same model holds for the bilateral migration case. The model is drawn with a zero-thickness ETS zone fault for simplicity, but the concept here can be extended into a finite-thickness heterogeneous brittle-ductile mixed fault zone.

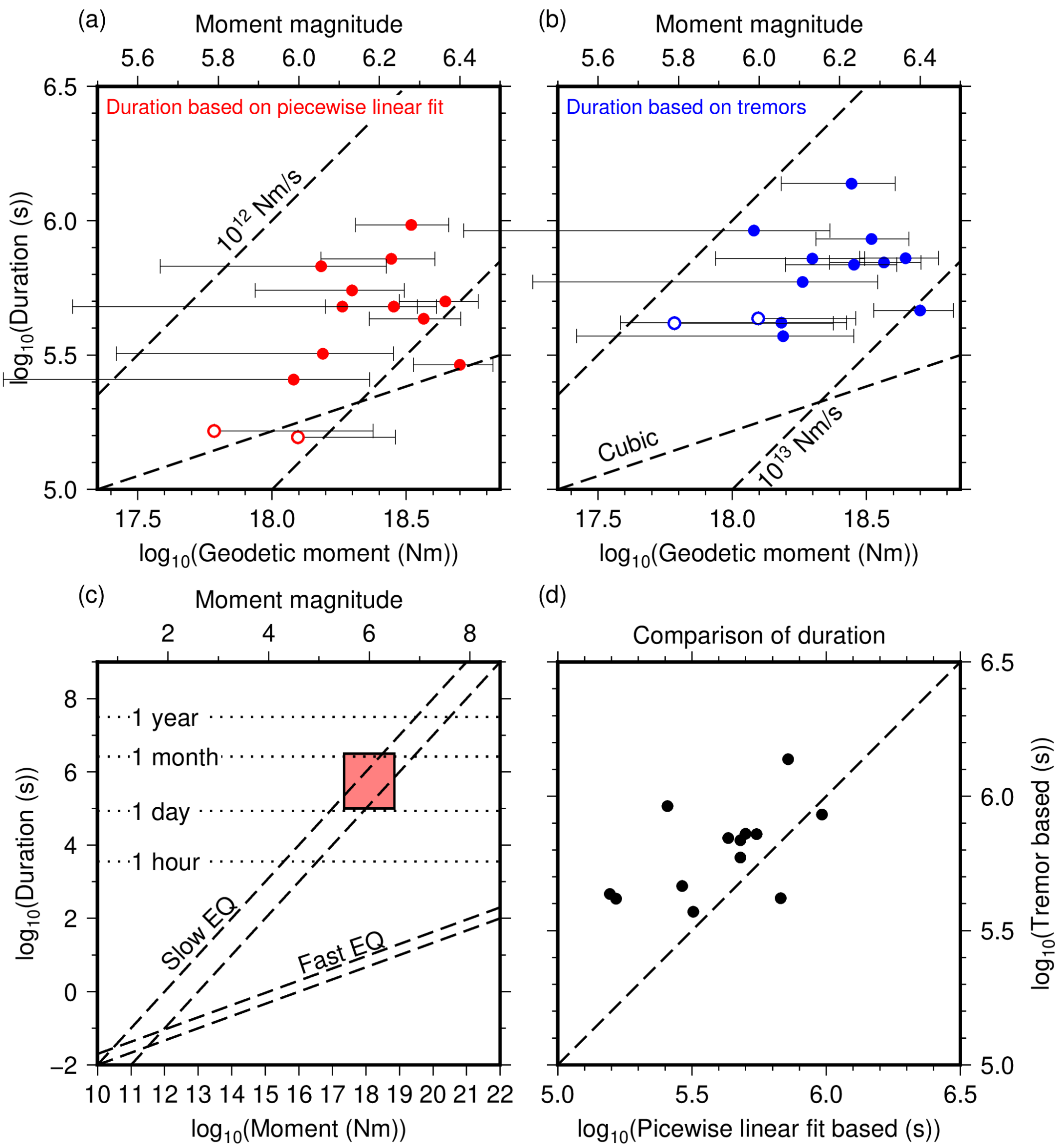

Figure 9. Moment-duration scaling of SSE initiation estimated in this study. (a-b) Moment and duration (dots) with duration estimated by the piece-wise linear fit (a; Figures 2, 4a, and S14-S25) and the tremor count analysis (b; Figure S28). We estimated error bars of geodetic moment based on the quartile deviation of the GPS stack. Data points are drawn with open symbols with error bars on the lower side trimmed when their ends are negative. (c) Global moment-duration scaling for fast and slow earthquakes (drawn after Ide and Beroza (2023)). Area of (a-b) is shown as a red rectangle. (d) Comparison of duration estimated by the two ways shown in (a-b). The broken line indicates a 1:1 ratio.

Supporting Information for "Slip-tremor interaction at the very beginning of Episodic Tremor and Slip in Cascadia"

Yuji Itoh[1,2], Anne Socquet[1], and Mathilde Radiguet[1]

[1]Univ. Grenoble Alpes, Univ. Savoie Mont Blanc, CNRS, IRD, Univ. Gustave Eiffel, ISTerre, 38000 Grenoble, France

[2]Earthquake Research Institute, The University of Tokyo, Tokyo, Japan

Contents of this file

1. Text S1. Details of sub-daily GPS time series cleaning and multi-site stacking

1.1. Sub-daily GPS time series cleaning

We employed GPS coordinates at a 5-minute interval processed by Nevada Geodetic Laboratory (Blewitt et al., 2018). After fixing the coordinates into the North American plate reference frame (Altamimi et al., 2017), we removed spatiotemporally correlating fluctuations due to multipath (e.g., Choi et al., 2004; Itoh & Aoki, 2022; Larson et al., 2007; Ragheb et al., 2007), diurnal variation (Itoh et al., 2022) and common mode error (e.g., Wdowinski et al., 1997). We mostly followed the procedure of Moutote, Itoh, Lengliné, Duputel, and Socquet (2023) and Itoh, Socquet, and Radiguet (2023) (Figure S13a) and outline the step-by-step procedure here. We employed Seasonal-Trend decomposition using LOESS (STL, Cleveland et al., 1990; Pedregosa et al., 2011) to separate fluctuations due to multipath and diurnal variations by setting their repeat period as 23 hours 55 minutes, and 1 day, respectively. Here, the choice of 23 hours 55 minutes is based on the closest integer multiple of the GPS sampling rate (5 minutes) to the typical multipath period (23 hours 55 minutes 54 seconds; e.g., Ragheb et al., 2007). Then, we removed the common mode error from the time series free from the two periodic noises. We explain the procedure of the common mode error estimation in the next paragraph. After removing the common mode error, we removed outliers which extremely deviate from the median of each time series based on Equation (1) of Itoh et al. (2022) with $n = 8$. Finally, we removed artificial offsets due to instrumental changes and other technical reasons on days described on NGL's database, by calculating a difference between averages of a bunch of epochs before and after the day.

To estimate the common mode error, we stacked time series at sites between 121°W and 119°W, where we assumed that the impact of the Cascadia megathrust processes was negligible (Figure S13b). Before stacking the time series at those sites, they went through a data cleaning process similar to the above-mentioned except for two points: (1) we skipped the common mode error removal step and (2) we adopted $n = 10$ for the outlier removal method. We applied a looser criterion to define the outliers because it was practically quite difficult to distinguish real outliers and coordinate deviations of common modes. We weighted each site equally in the stacking, and we excluded sites with a small number of epochs.

1.2. Multi-site stacking

To resolve the temporal evolution of SSE at the initiation stage, we performed a weighted stack of multi-site time series (e.g., Bletery & Nocquet, 2023; Jara et al., 2024; Marill et al., 2021; Okada et al., 2022; Rousset et al., 2017; Wdowinski et al., 1997). The GPS stack for event e, $d_e(t)$, is:

$$d_e(t) = \frac{\sum_{i=1}^{N_e} \mathbf{d}_i^{GPS}(t) \cdot \mathbf{w}_i^e}{\sum_{i=1}^{N_e} |\mathbf{w}_i^e|}, \tag{1}$$

where, the term $\mathbf{d}_i^{GPS}(t)$ is the cleaned GPS time series at site i out of N_e time series. Here, $\mathbf{d}_i^{GPS}(t)$ is a matrix containing two time series in the east and north directions. The weight term $\mathbf{w}_i^e$ is a two-dimensional vector containing east and north elastic displacements due to anticipated megathrust slip in the initiation zone. For each event, $\mathbf{w}_i^e$ is time-invariant expected displacements associated with slip in the initiation zone. Here, $\mathbf{w}_i^e$ is elastic displacements in a homogeneous isotropic half-space (Okada, 1985) due to slip in a template fault model which has the same geometry as the square area designed for the definition of the initiation zone (Section 2.1). Depth, strike, and dip for the template faults follow Slab 2 model (G. P. Hayes et al., 2018; G. Hayes, 2018) and rake angle is computed with the OR-JF Euler pole (Bartlow, 2020; McCaffrey et al., 2007). Their dot product $\mathbf{d}_i^{GPS}(t) \cdot \mathbf{w}_i^e$ projects the time series in the two directions into the anticipated SSE-induced displacement direction and assign a weight for multi-site stacking according to the anticipated displacement amplitude, similar to Marill et al. (2021) and Bletery and Nocquet (2023). In this way, we can naturally enhance the expected signal associated with the initiation stage of SSE. As we normalized the stack using the sum of the norm of template displacement at each site (The denominator of Equation 1), the obtained GPS stack has the displacement unit. We went through the following steps for the selection of sites to stack for each event: (1) We normalized model displacements at the available sites $\mathbf{w}_i^e$ with respect to their maximum value $w_{max}^e = \max_i(|\mathbf{w}_i^e|)$, (2) we retrieved sites satisfying $|\mathbf{w}_i^e|/w_{max}^e >= b$ with $b = 0.3$, and (3) we discarded sites with the number of epochs smaller than 10000 ($\sim$ 35 days) in each analysis period from those retained at step 2. In some cases, we further manually removed some bad sites which show too different trend from other sites used for stacking. After the weighted stacking, we applied a moving median with a window length of 3 days to the stacked time series to drop off high-frequency fluctuations, and better resolve the long-period temporal evolution of the GPS stack. Sensitivity tests for the choice of b and the template fault shape indicate that the trend of the GPS stack at the initiation stage is not critically impacted by these stacking parameters (Figure S26).

The GPS stack exhibits a rapid transient signal roughly during the high tremor activity in the initiation zone (Figures 2a and S14a-S25a). Prior to and/or following this transient, most of the GPS stack exhibits a gentler displacement trend in the opposite direction to the transient signal. To remove this local trend, we fit a function consisting of a linear trend and a ramp function to the moving median of the GPS stack and subsequently removed the estimated trend (Figures 2a and S14a-S25a). The start and end times of the ramp function were determined by grid search. Event #13 is a re-initiation event after the short halt of Event #12, so we trimmed out the data period corresponding to Event #12 (Figures S24-S25). One of the reasons for this local trend could be the long-term trend representing landward motion due to interevent megathrust locking (e.g., Li et al., 2018; Schmalzle et al., 2014), which we did not remove from time series at individual sites. Yet, the origin of this trend is still enigmatic because the similar local trend before and/or after the transient appears by stacking GNSS time series corrected for the long-term trend (e.g., Okada et al., 2022; Rousset et al., 2017).

2. Text S2. Synthetic test of GPS stack using kinematic SSE model

We carried out a synthetic test to verify that part of the GPS stack time series satisfactorily represents the temporal evolution of the moment in the initiation zone and is little smeared by the migrating slip. We built a kinematic slow slip model, simulated surface displacement time series due to the slip, and carried out the same weighted-stacking analysis with these synthetic displacement time series.

2.1. Model description

In the synthetic model, the slip begins by growing as an expanding circular patch from one point, which is followed by a bilateral along-strike migration once the rupture front fills the down-dip width of the modeled fault (Figure S27a). The initial circular slip area has a radius equal to half of the down-dip model dimension and we call this slip area initiation zone. We put the areas with the same geometry at both lateral ends of the model domain, which we call the termination zone. For simplicity, we do not consider along-dip or along-strike variation of the final slip amount except the quick tapering toward zero at the end of the model domain. The rupture velocity is set constant for simplicity; a number of SSE and slow earthquake observations proves that this simplification is valid at least for the migration stage (Figures 1 and S1-S12) (e.g., Houston et al., 2011). Following Costantino et al. (2023), the temporal evolution of slip $s(x_j, t)$ at each subfault j at location x_j and time t obeys a logistic function:

$$s(x_j, t) = \frac{S(x_j)}{1 + e^{-\tau_j (t - t_j^c)}} \tag{2}$$

where, $S(x_j)$, τ_j, and t_j^c indicate the final slip explained above, a time constant, and a time of the peak slip rate, respectively, at each subfault j. Here, τ_j and t_j^c are functions of three parameters, namely, an onset time t_j^0 of slip at each patch, an arbitrary positive slip duration T_j and a non-dimensional coefficient a ranging from 0 to 0.5:

$$\tau_j = \frac{2}{T_j} \log(\frac{1-a}{a}), \tag{3}$$

and

$$t_j^c = t_j^0 + \frac{T_j}{2}. \tag{4}$$

The onset time of each patch t_j^0 is automatically determined from a prescribed rupture velocity. The terms T_j and a need prescribing. With Equations (2) - (4), slip with an amount of $(1 - 2a)S(x_j)$ takes place during the duration T_j starting from the rupture front arrival at each subfault at time t_j^0. Prescribing larger T_j and/or a results in slower moment release. By setting a satisfactorily small a value, the moment release before the onset time becomes negligibly small. The duration T_j is defined as follows:

$$\begin{aligned} T_j &= \frac{r_j}{r}(T_{migr} - T_{nucl}) + T_{nucl} \quad (r_j \leq r) \\ &= T_{migr} \quad\quad\quad\quad\quad\quad\quad\quad\; (r_j > r) \end{aligned} \tag{5}$$

where r, r_j, T_{nucl}, and T_{migr} is the radius of the initiation zone, the distance of subfault j from its center, and the duration of slip at each subfault inside and outside the initiation zone, respectively. In this scenario, T_j changes from T_{nucl} to T_{migr} linearly with the distance from the center to the edge of the circular initiation zone, and at the edge, the duration is equal to the migration stage so that the continuous change is realized without a jump. By prescribing a larger duration to T_{nucl} than T_{migr}, we can better model slip hinted by the longer duration of tremor activity in the initially slipping area than the outside; the resultant slip model behaves more closely to a crack-like rupture at the initiation.

2.2. Parameter setting

We referred to Event #2 to prescribe the model parameters (Figure 1). The modeled fault has a geometry of 400 and 80 km in the strike and dip directions, so the radius of the initiation and termination zones r is 40 km (Figures S27a-b). The initiation point of slip is set at the center of the model domain where the depth is set to 40 km (Table 1). The dip angle is 10 degrees everywhere for simplicity as a representative value of the region of interest (Table S2). We imposed a dip slip everywhere and no strike slip component is considered. The rupture velocity was set to 8 km/day, consistent with earlier studies (e.g., Houston, 2015; Houston et al., 2011). We set a to 0.01 and T_{nucl} and T_{migr} to 11 and 6 days, respectively, read from the distance versus time diagram of tremors (Figures 1c and S27b). We do not implement the change in the strike orientation near the border of

Canada and the United States into this synthetic model but this simplification is enough for our aim of this synthetic model analysis.

2.3. Synthetic test result

With the prescribed parameters, we simulated a temporal evolution of surface displacements at the GPS sites projected to the synthetic model domain. The obtained time series were subsequently stacked with weights gained as elastic displacements caused by a template fault slip, which was also projected to the synthetic model domain. First, we compared the synthetic displacement stack with the moment evolution computed only from the subfaults in the initiation zone (i.e., $r_j \leq r$). We normalized them by the final value of each, which matched with each other quite well (Figure S27c). This means that the temporal evolution function of the GPS stack satisfactorily represents the temporal function of the moment evolution in the initiation zone if we could perfectly exclude the laterally migrating slip effects from the GPS stack. However, such a correction is practically not feasible. Then, we compared two synthetic displacement stacks containing the contribution from (1) the initiation zone only and (2) all the subfaults in the entire model domain (Figure S27d); the latter can be considered as a noise-free observed stack. As expected, the two stacks match with each other perfectly from the beginning to a certain time and they depart from each other after this time. This departure time is close to the time when the rupture front passes the edge of the initiation zone and, therefore, the contribution of the migrating slip to the surface displacement starts to become significant. Based on these synthetic test results, we verified that we can interpret the temporal evolution pattern of the observed GPS stacks as a representation of scale-free temporal evolution of moment release in the initiation zone until a certain time. We determined the time until which we could consider the migration effect based on the cumulative tremor count curve (Section 3.1).

3. Text S3. Synthetic test of GPS stack using kinematic SSE model

We inferred approximate area of the tremor activity by fitting an ellipse enclosing about 95% of tremor epicenters using singular value decomposition (SVD) analysis. For each ETS initiation event, we took tremors from $t_{norm} = -1$ to $t_{norm} = T_{area}$ with T_{area} varied from -0.6 to 1 to illustrate the temporal evolution of area until the onset of the migration stage. The normalized time axis t_{norm} is defined in Section 3.4. The threshold of 95% was sometimes not enough to exclude tremors very far away from the main cluster in case some isolated clusters were recorded in the catalogs. To mitigate their influence, for all the cases, we carried out the SVD twice; after the first run, we calculated the standard deviation of tremor distribution measured in the directions of the two ellipse axes, and trimmed out tremors away from the ellipse center by 4 times of the standard deviation. Then, we repeated the same analysis without those outliers and calculated the area of tremor activity, which was finally corrected for the average dip angle of the plate interface taken from that of each template fault (Table S2).

References

Altamimi, Z., Métivier, L., Rebischung, P., Rouby, H., & Collilieux, X. (2017, 03). ITRF2014 plate motion model. *Geophysical Journal International*, *209*(3), 1906-1912. Retrieved from `https://doi.org/10.1093/gji/ggx136` doi: 10.1093/gji/ggx136

Bartlow, N. M. (2020). A long-term view of episodic tremor and slip in cascadia. *Geophysical Research Letters*, *47*(3), e2019GL085303. Retrieved from https://agupubs.onlinelibrary.wiley.com/doi/abs/10.1029/2019GL085303 (e2019GL085303 10.1029/2019GL085303) doi: https://doi.org/10.1029/2019GL085303

Bletery, Q., & Nocquet, J.-M. (2023). The precursory phase of large earthquakes. *Science*, *381*(6655), 297-301. Retrieved from https://www.science.org/doi/abs/10.1126/science.adg2565 doi: 10.1126/science.adg2565

Blewitt, G., Hammond, W. C., & Kreemer, C. (2018). Harnessing the gps data explosion for interdisciplinary science. *EOS*, *99*. doi: 10.1029/2018EO104623

Choi, K., Bilich, A., Larson, K. M., & Axelrad, P. (2004). Modified sidereal filtering: Implications for high-rate gps positioning. *Geophysical Research Letters*, *31*(22). doi: 10.1029/2004GL021621

Cleveland, R. B., Cleveland, W. S., McRae, J. E., & Terpenning, I. (1990). Stl: A seasonal-trend decomposition. *J. Off. Stat*, *6*(1), 3–73.

Costantino, G., Giffard-Roisin, S., Radiguet, M., Dalla Mura, M., Marsan, D., & Socquet, A. (2023). Multi-station deep learning on geodetic time series detects slow slip events in cascadia. *Communications Earth & Environment*, *4*(1), 435. doi: 10.1038/s43247-023-01107-7

Hayes, G. (2018, Aug). *A comprehensive subduction zone geometry model.* Retrieved from https://doi.org/10.5066/F7PV6JNV

Hayes, G. P., Moore, G. L., Portner, D. E., Hearne, M., Flamme, H., Furtney, M., & Smoczyk, G. M. (2018). Slab2, a comprehensive subduction zone geometry model. *Science*, *362*(6410), 58-61. Retrieved from https://www.science.org/doi/abs/

10.1126/science.aat4723 doi: 10.1126/science.aat4723

Houston, H. (2015). Low friction and fault weakening revealed by rising sensitivity of tremor to tidal stress. *Nature Geoscience*, *8*(5), 409–415.

Houston, H., Delbridge, B. G., Wech, A. G., & Creager, K. C. (2011). Rapid tremor reversals in cascadia generated by a weakened plate interface. *Nature Geoscience*, *4*(6), 404–409.

Itoh, Y., & Aoki, Y. (2022). On the performance of position-domain sidereal filter for 30-s kinematic gps to mitigate multipath errors. *Earth, Planets and Space*, *74*(1), 1–20. doi: 10.1186/s40623-022-01584-8

Itoh, Y., Aoki, Y., & Fukuda, J. (2022). Imaging evolution of cascadia slow-slip event using high-rate gps. *Scientific reports*, *12*(1), 7179.

Itoh, Y., Socquet, A., & Radiguet, M. (2023). Largest aftershock nucleation driven by afterslip during the 2014 iquique sequence. *Geophysical Research Letters*, *50*(24), e2023GL104852. Retrieved from https://agupubs.onlinelibrary.wiley.com/doi/abs/10.1029/2023GL104852 (e2023GL104852 2023GL104852) doi: https://doi.org/10.1029/2023GL104852

Jara, J., Jolivet, R., Socquet, A., Comte, D., & Norabuena, E. (2024, Jun.). Detection of slow slip events along the southern peru - northern chile subduction zone. *Seismica*, *3*(1). Retrieved from https://seismica.library.mcgill.ca/article/view/980 doi: 10.26443/seismica.v3i1.980

Larson, K. M., Bilich, A., & Axelrad, P. (2007). Improving the precision of high-rate gps. *Journal of Geophysical Research: Solid Earth*, *112*(B5). doi: 10.1029/2006JB004367

Li, S., Wang, K., Wang, Y., Jiang, Y., & Dosso, S. E. (2018). Geodetically inferred locking state of the cascadia megathrust based on a viscoelastic earth model. *Journal of Geophysical Research: Solid Earth*, *123*(9), 8056-8072. Retrieved from https://agupubs.onlinelibrary.wiley.com/doi/abs/10.1029/2018JB015620 doi: https://doi.org/10.1029/2018JB015620

Marill, L., Marsan, D., Socquet, A., Radiguet, M., Cotte, N., & Rousset, B. (2021). Fourteen-Year Acceleration Along the Japan Trench. *Journal of Geophysical Research: Solid Earth*, *126*(11), e2020JB021226. doi: 10.1029/2020JB021226

McCaffrey, R., Qamar, A. I., King, R. W., Wells, R., Khazaradze, G., Williams, C. A., … Zwick, P. C. (2007, 06). Fault locking, block rotation and crustal deformation in the Pacific Northwest. *Geophysical Journal International*, *169*(3), 1315-1340. Retrieved from https://doi.org/10.1111/j.1365-246X.2007.03371.x doi: 10.1111/j.1365-246X.2007.03371.x

Michel, S., Gualandi, A., & Avouac, J.-P. (2019, September). Interseismic Coupling and Slow Slip Events on the Cascadia Megathrust. *Pure and Applied Geophysics*, *176*(9), 3867-3891. doi: 10.1007/s00024-018-1991-x

Moutote, L., Itoh, Y., Lengliné, O., Duputel, Z., & Socquet, A. (2023). Evidence of a transient aseismic slip driving the 2017 valparaiso earthquake sequence, from foreshocks to aftershocks. *Journal of Geophysical Research: Solid Earth*, *128*(9), e2023JB026603. Retrieved from https://agupubs.onlinelibrary.wiley.com/doi/abs/10.1029/2023JB026603 (e2023JB026603 2023JB026603) doi: https://doi.org/10.1029/2023JB026603

Okada, Y. (1985, 08). Surface deformation due to shear and tensile faults in a half-space. *Bulletin of the Seismological Society of America*, *75*(4), 1135-1154. Retrieved from https://doi.org/10.1785/BSSA0750041135 doi: 10.1785/BSSA0750041135

Okada, Y., Nishimura, T., Tabei, T., Matsushima, T., & Hirose, H. (2022). Development of a detection method for short-term slow slip events using gnss data and its application to the nankai subduction zone. *Earth, Planets and Space*, *74*(1), 1–18.

Pedregosa, F., Varoquaux, G., Gramfort, A., Michel, V., Thirion, B., Grisel, O., ... others (2011). Scikit-learn: Machine learning in python. *the Journal of machine Learning research*, *12*, 2825–2830.

Ragheb, A., Clarke, P. J., & Edwards, S. (2007). Gps sidereal filtering: coordinate-and carrier-phase-level strategies. *Journal of Geodesy*, *81*(5), 325–335. doi: 10.1007/s00190-006-0113-1

Rousset, B., Campillo, M., Lasserre, C., Frank, W. B., Cotte, N., Walpersdorf, A., ... Kostoglodov, V. (2017). A geodetic matched filter search for slow slip with application to the mexico subduction zone. *Journal of Geophysical Research: Solid Earth*, *122*(12), 10,498-10,514. Retrieved from https://agupubs.onlinelibrary.wiley.com/doi/abs/10.1002/2017JB014448 doi: https://doi.org/10.1002/2017JB014448

Schmalzle, G. M., McCaffrey, R., & Creager, K. C. (2014). Central cascadia subduction zone creep. *Geochemistry, Geophysics, Geosystems*, *15*(4), 1515-1532. Retrieved from https://agupubs.onlinelibrary.wiley.com/doi/abs/10.1002/2013GC005172 doi: https://doi.org/10.1002/2013GC005172

Wdowinski, S., Bock, Y., Zhang, J., Fang, P., & Genrich, J. (1997). Southern california permanent gps geodetic array: Spatial filtering of daily positions for estimating coseismic and postseismic displacements induced by the 1992 landers earthquake. *Journal of Geophysical Research: Solid Earth*, *102*(B8), 18057-18070. doi: 10.1029/97JB01378

Wech, A. G. (2021). Cataloging tectonic tremor energy radiation in the cascadia subduction zone. *Journal of Geophysical Research: Solid Earth*, *126*(10), e2021JB022523. Retrieved from https://agupubs.onlinelibrary.wiley.com/doi/abs/10.1029/2021JB022523 doi: https://doi.org/10.1029/2021JB022523

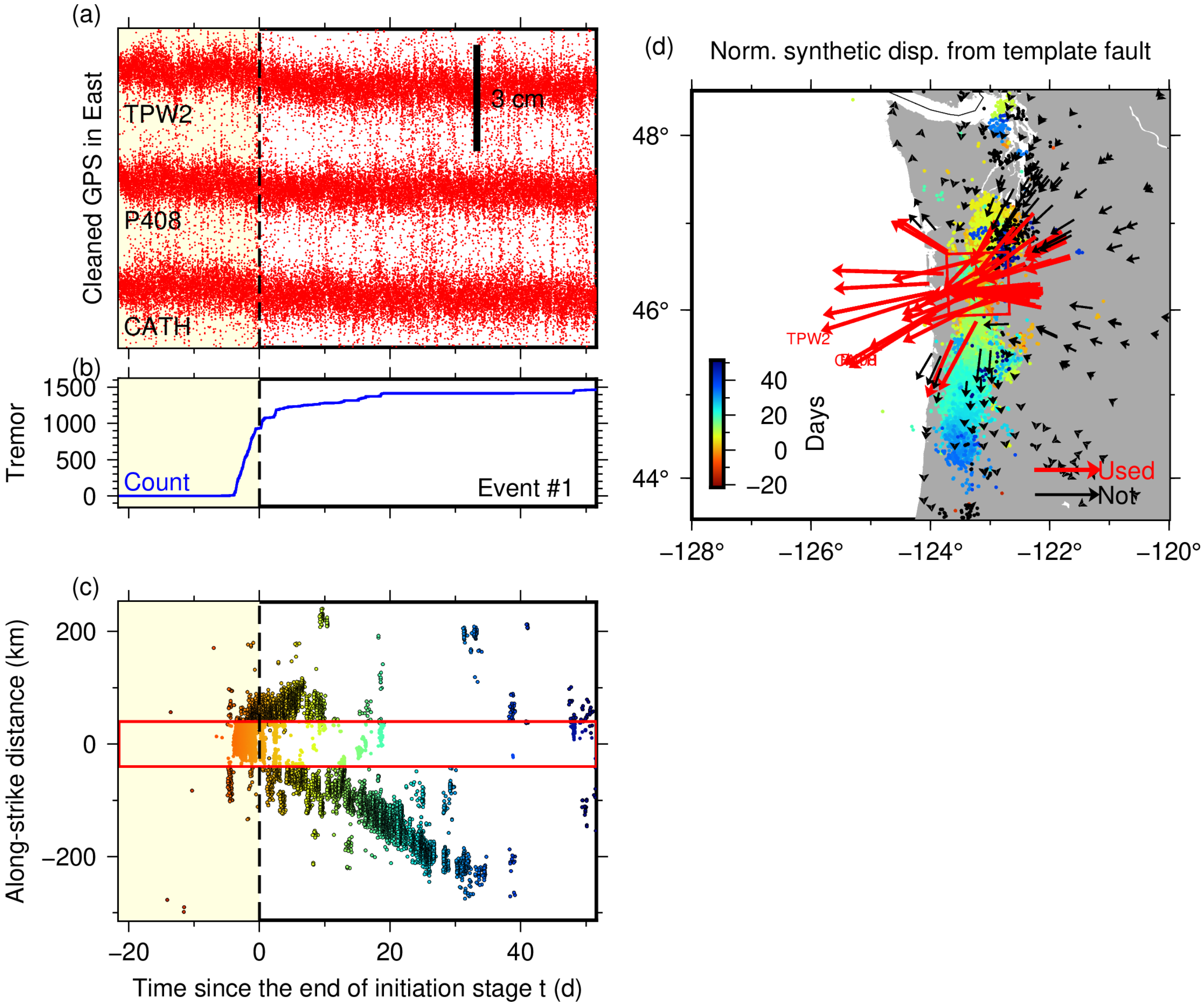

Figure S1. Same as Figure 1 but for Event #1.

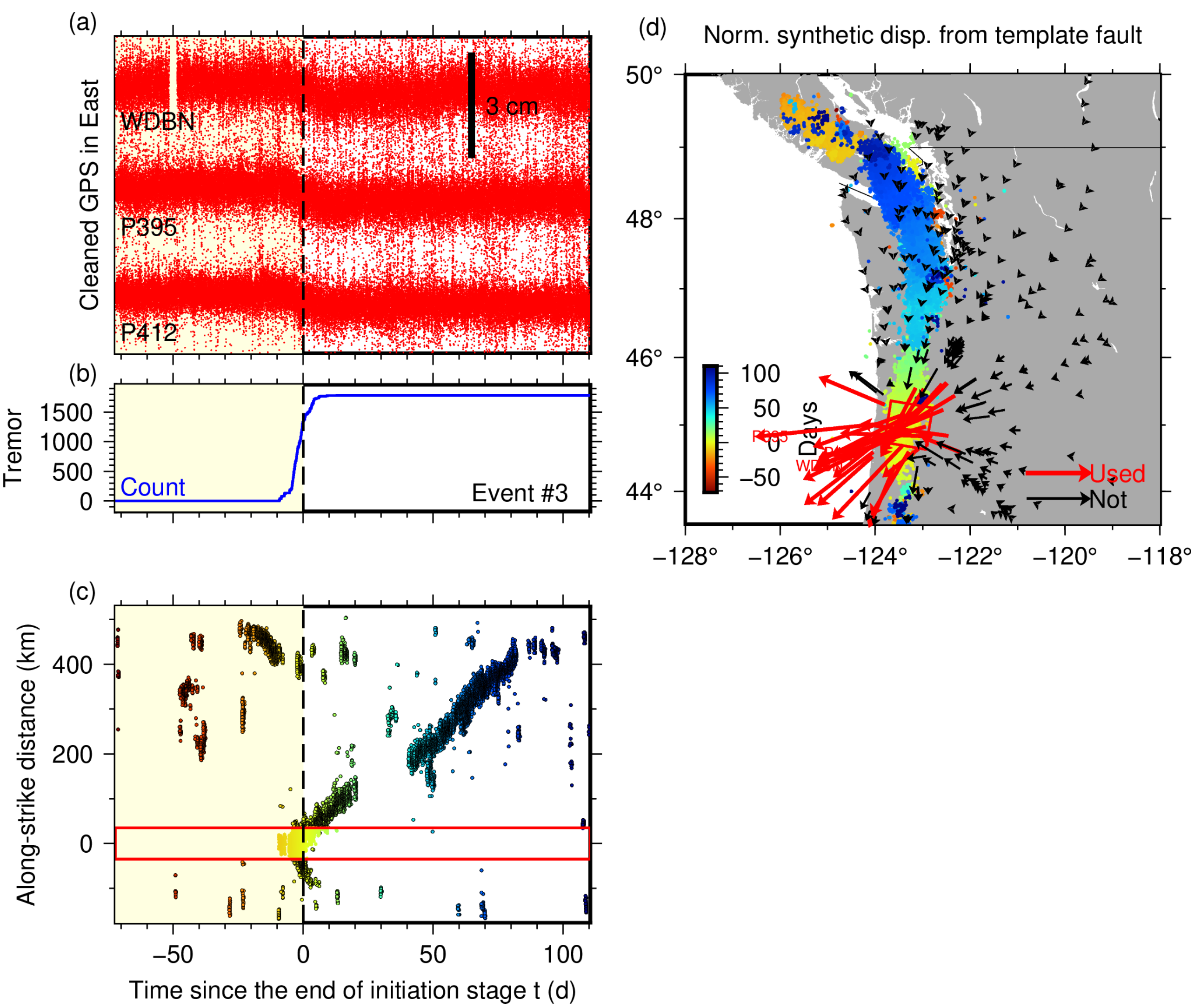

Figure S2. Same as Figure 1 but for Event #3.

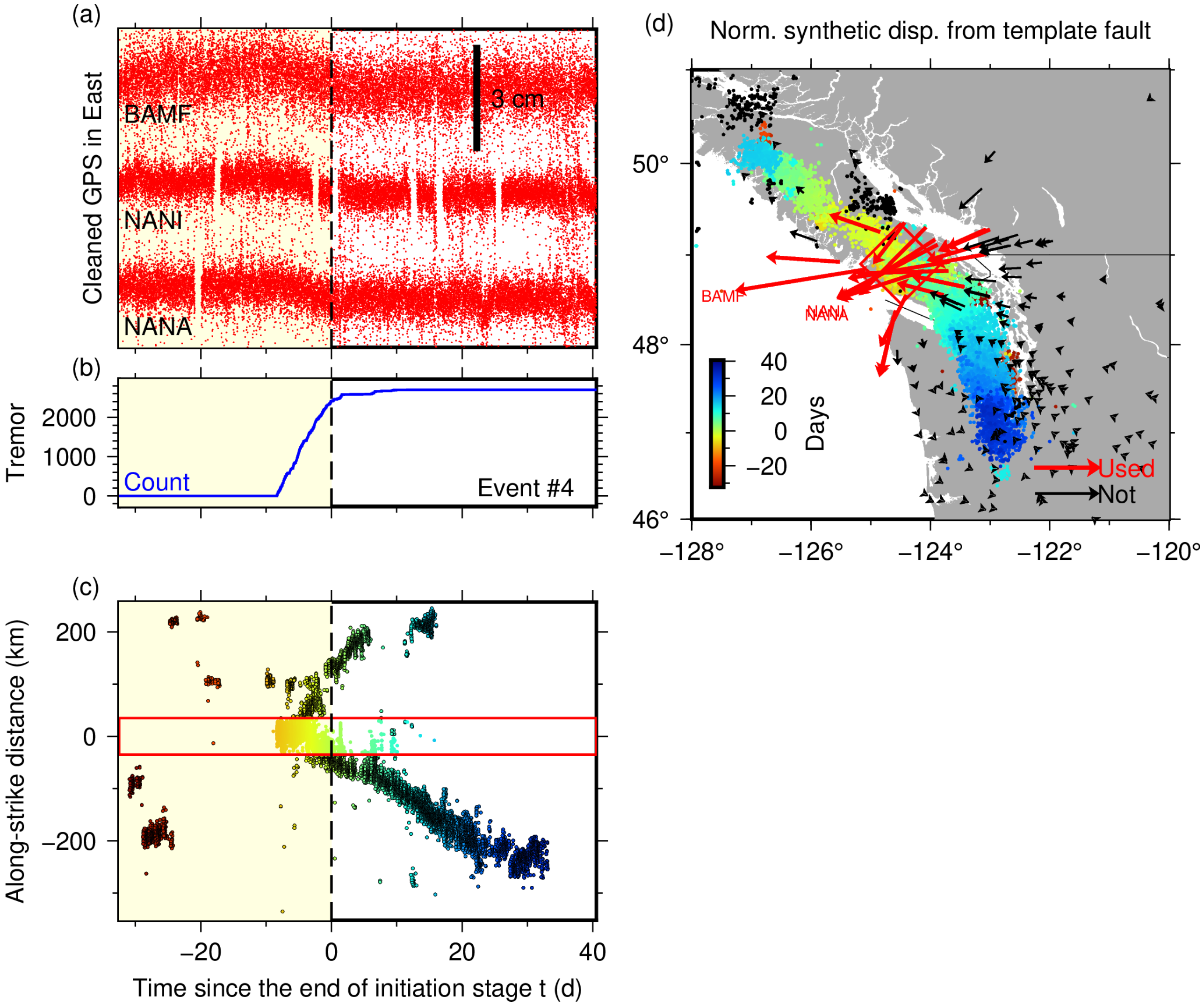

Figure S3. Same as Figure 1 but for Event #4.

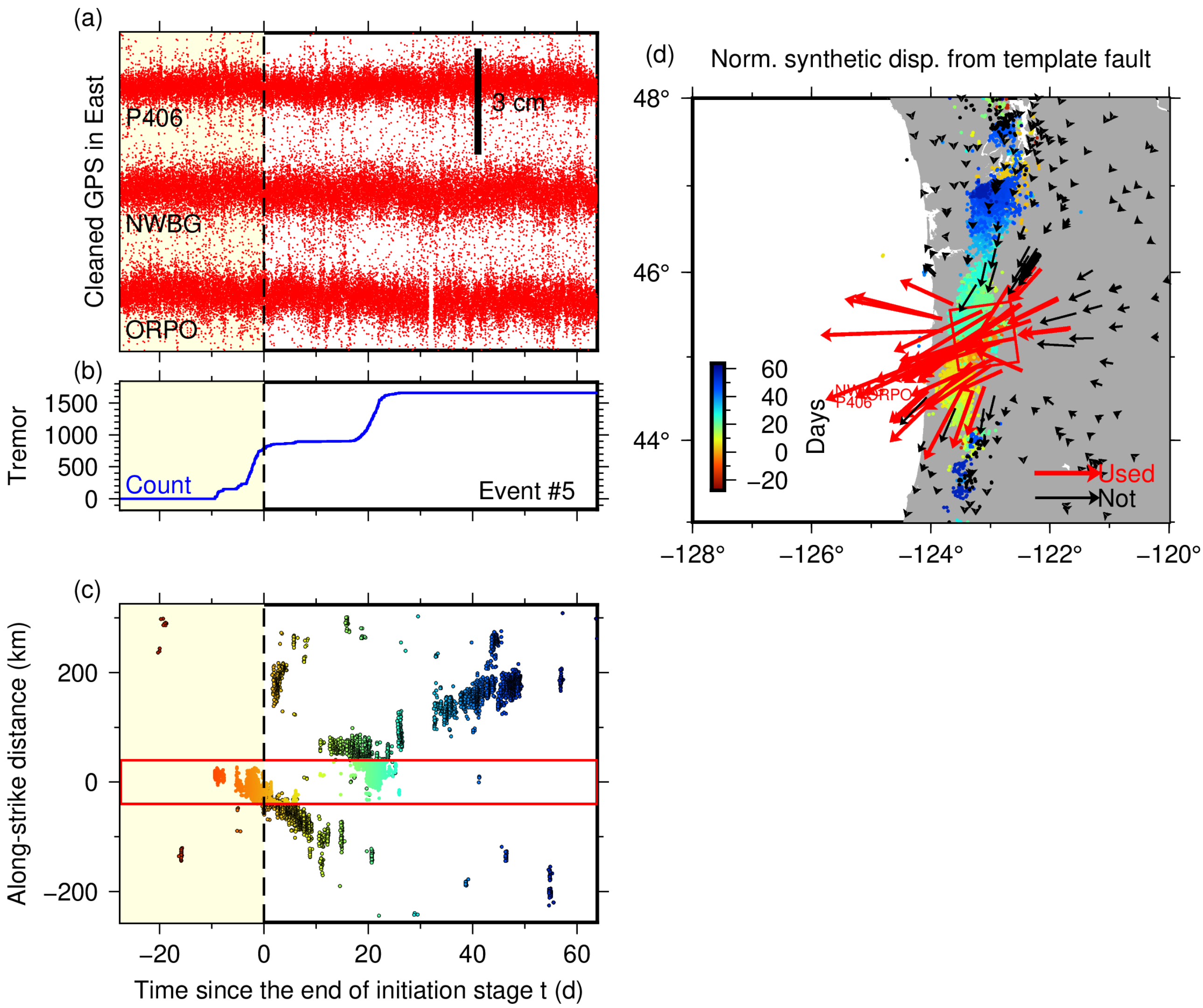

Figure S4. Same as Figure 1 but for Event #5.

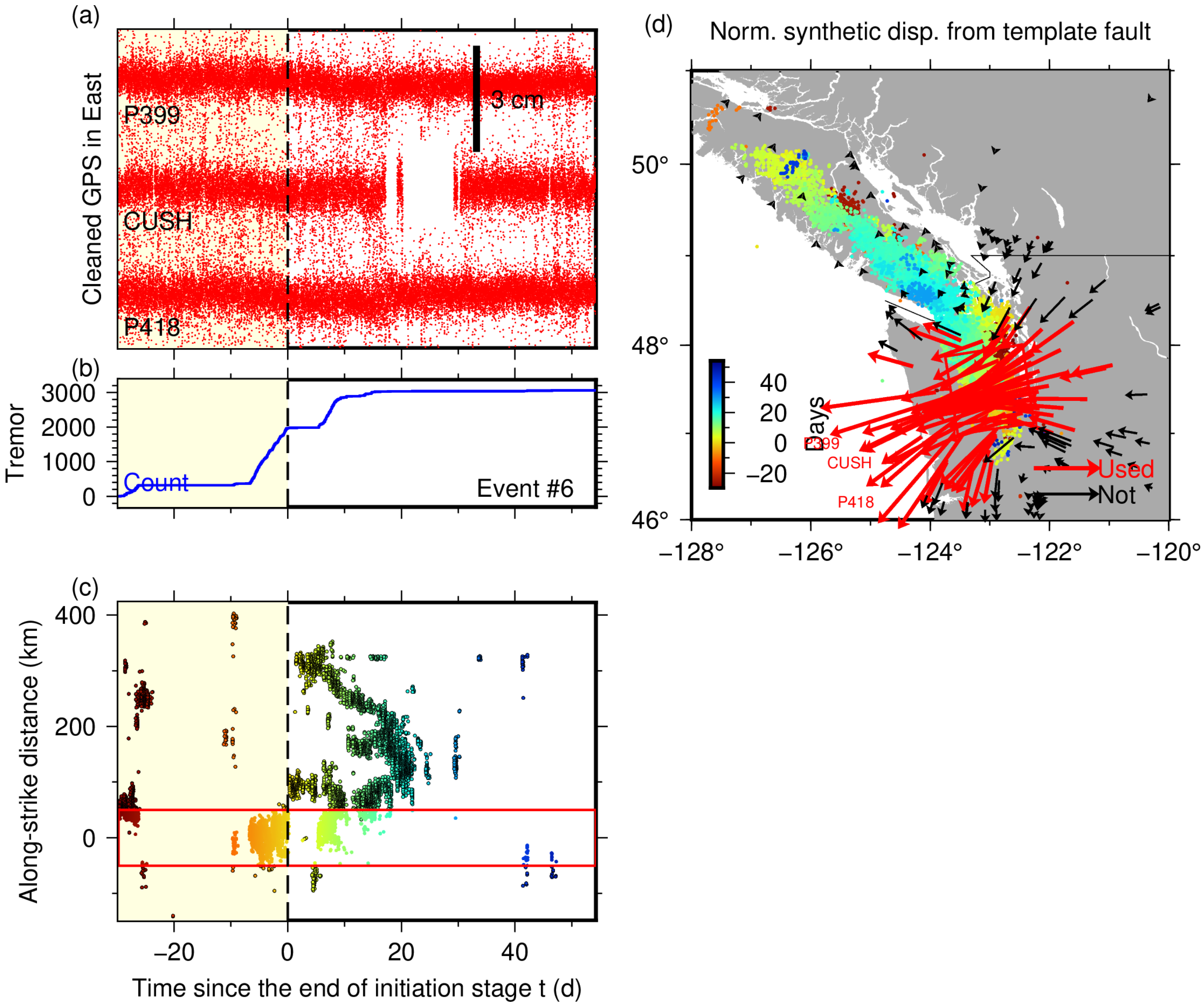

Figure S5. Same as Figure 1 but for Event #6.

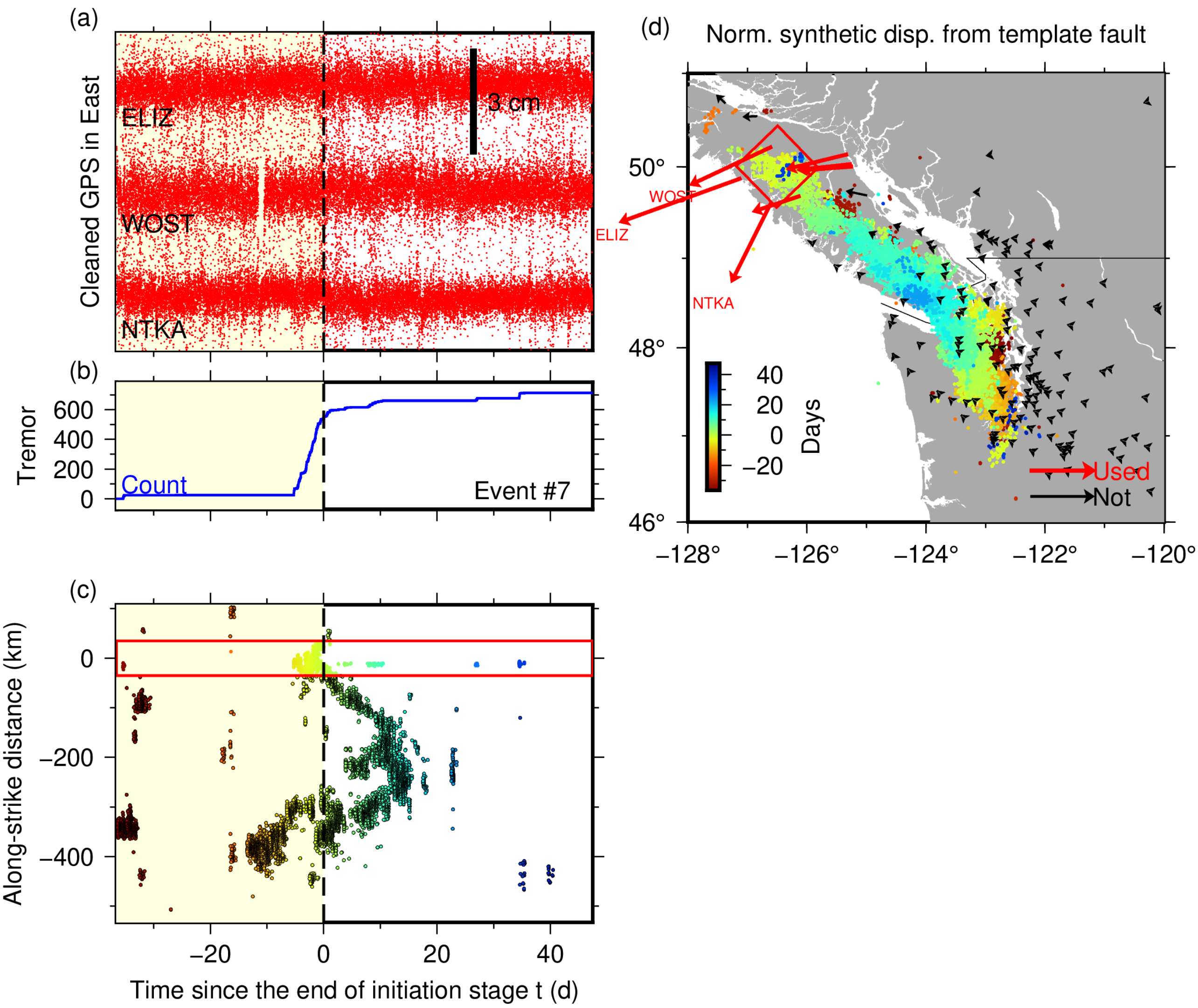

Figure S6. Same as Figure 1 but for Event #7.

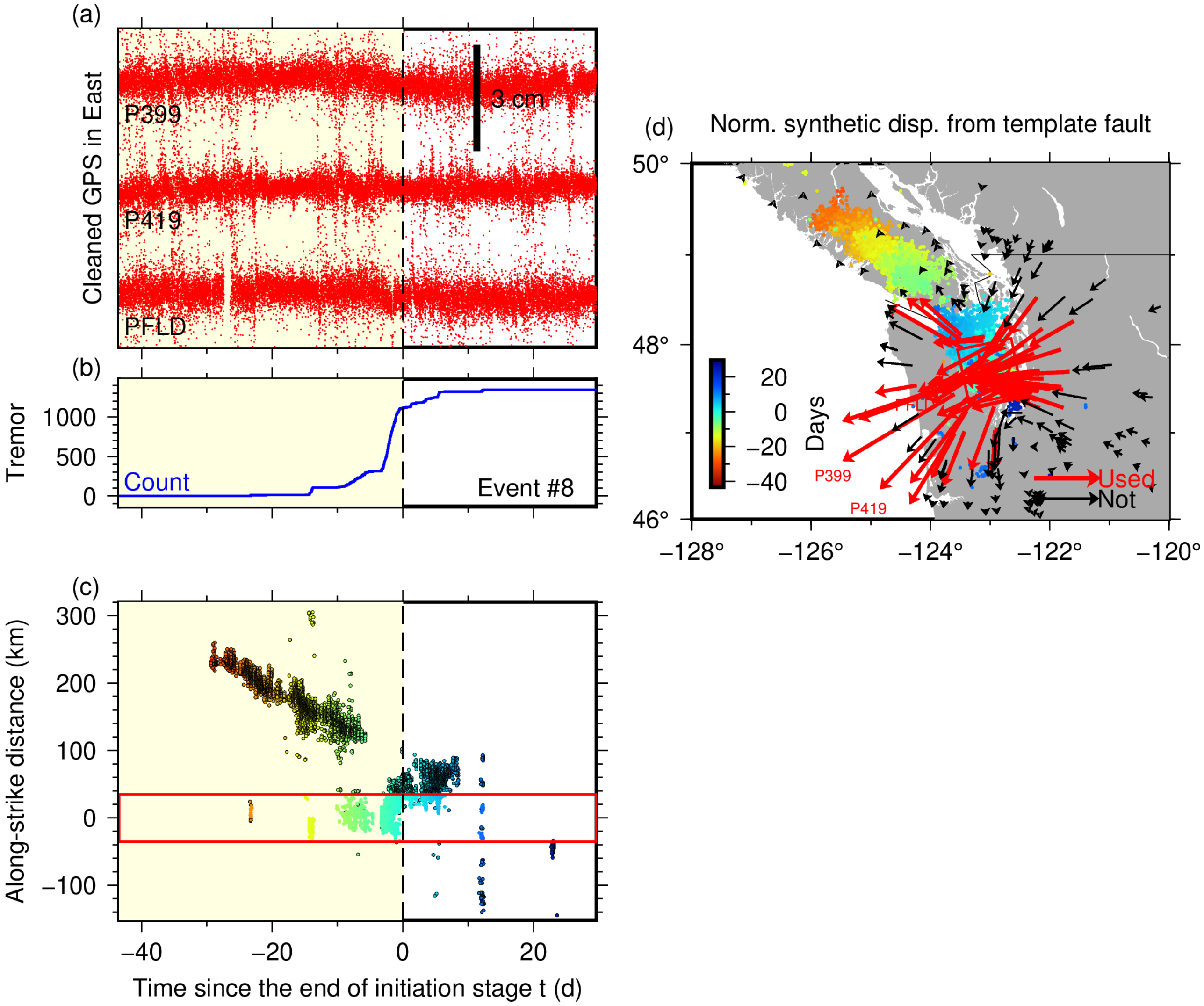

Figure S7. Same as Figure 1 but for Event #8.

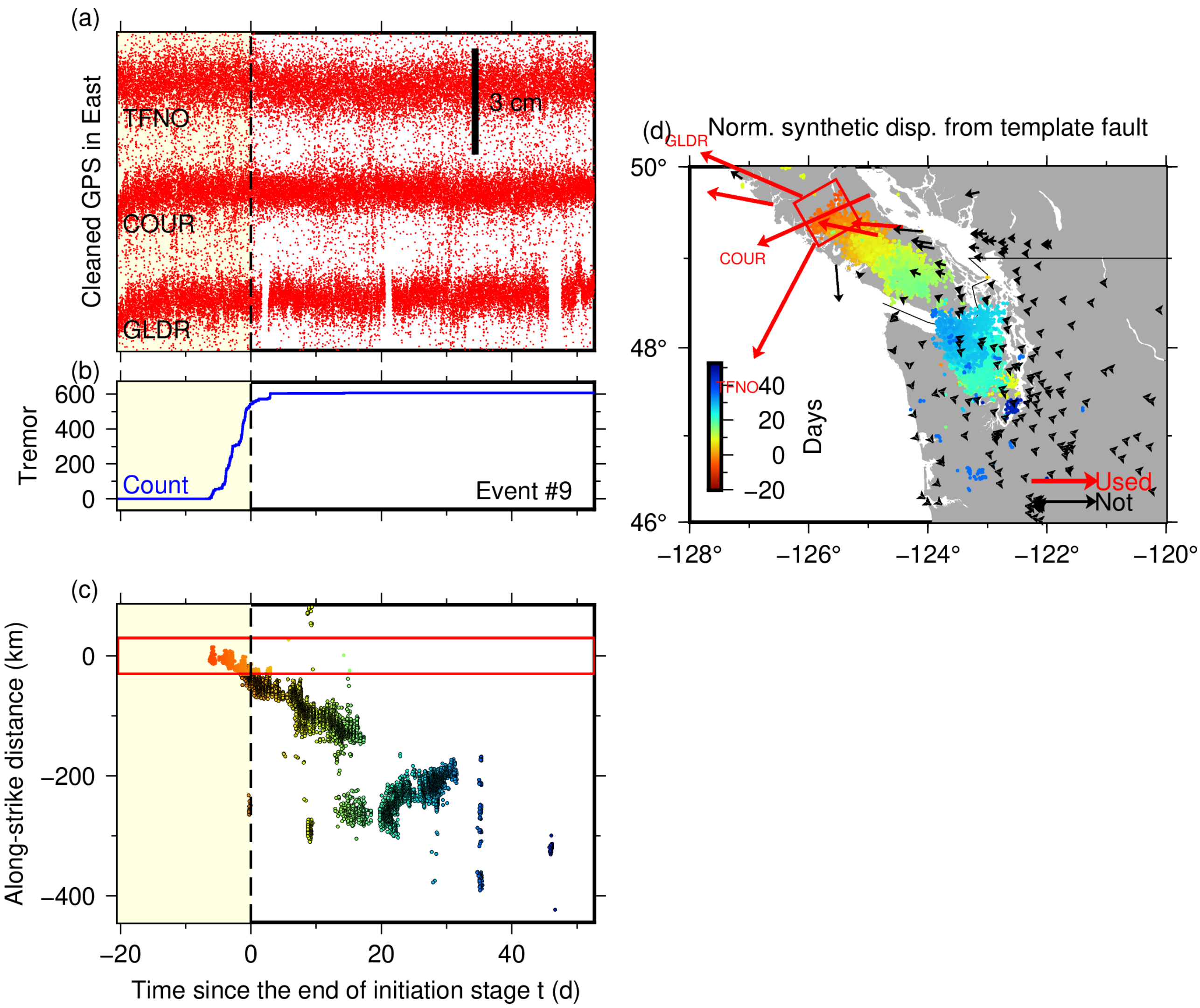

Figure S8. Same as Figure 1 but for Event #9.

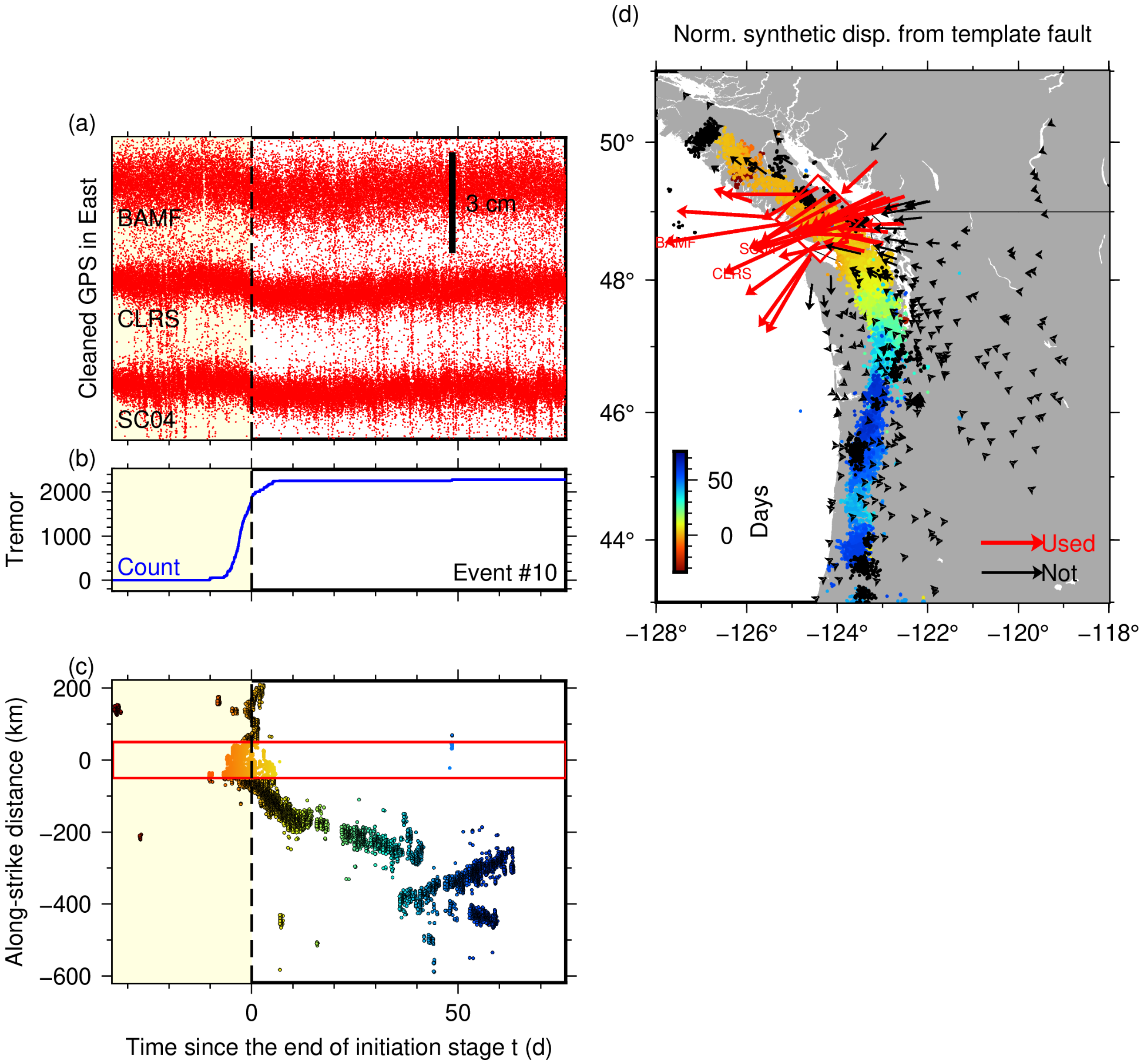

Figure S9. Same as Figure 1 but for Event #10.

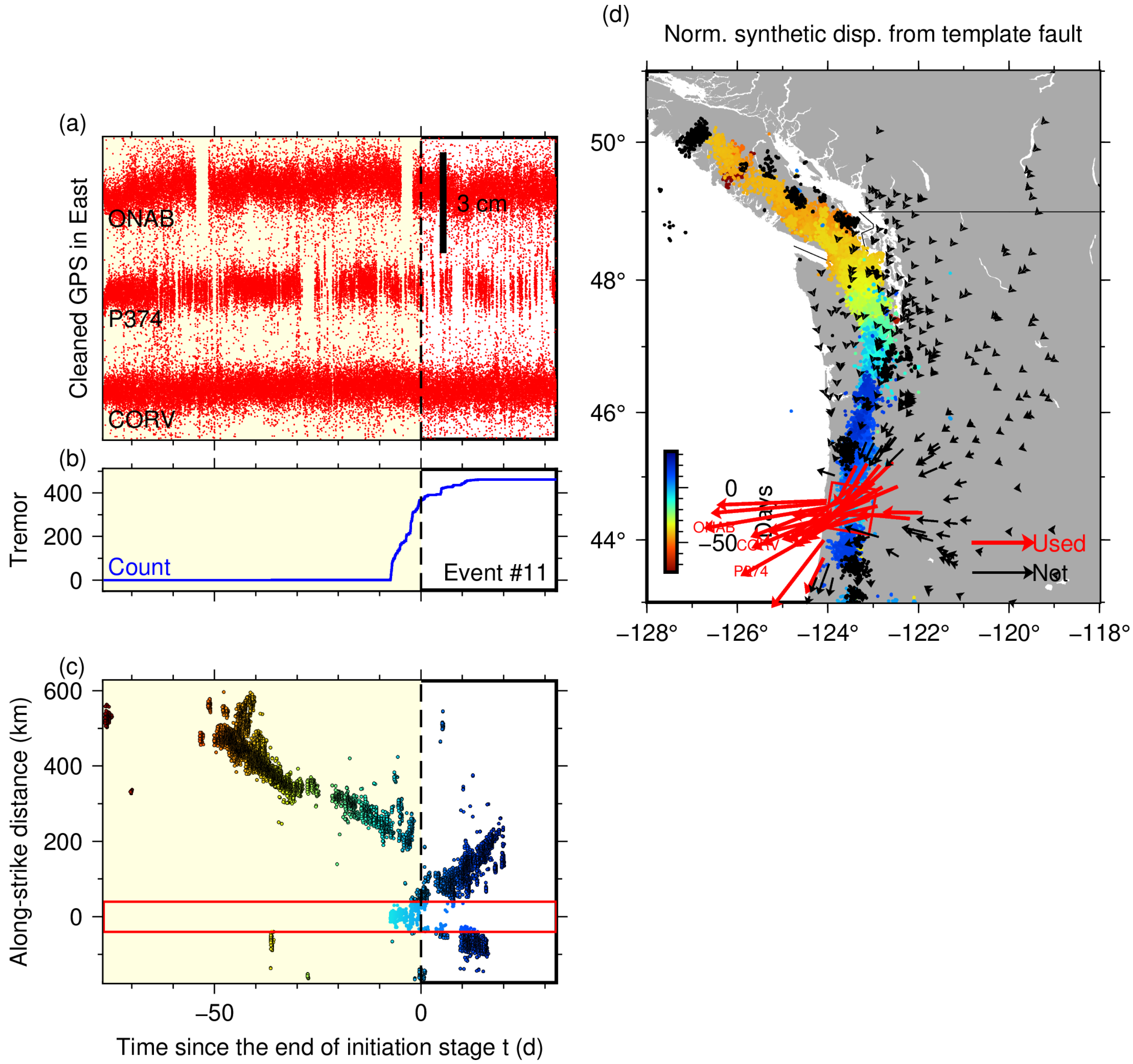

Figure S10. Same as Figure 1 but for Event #11.

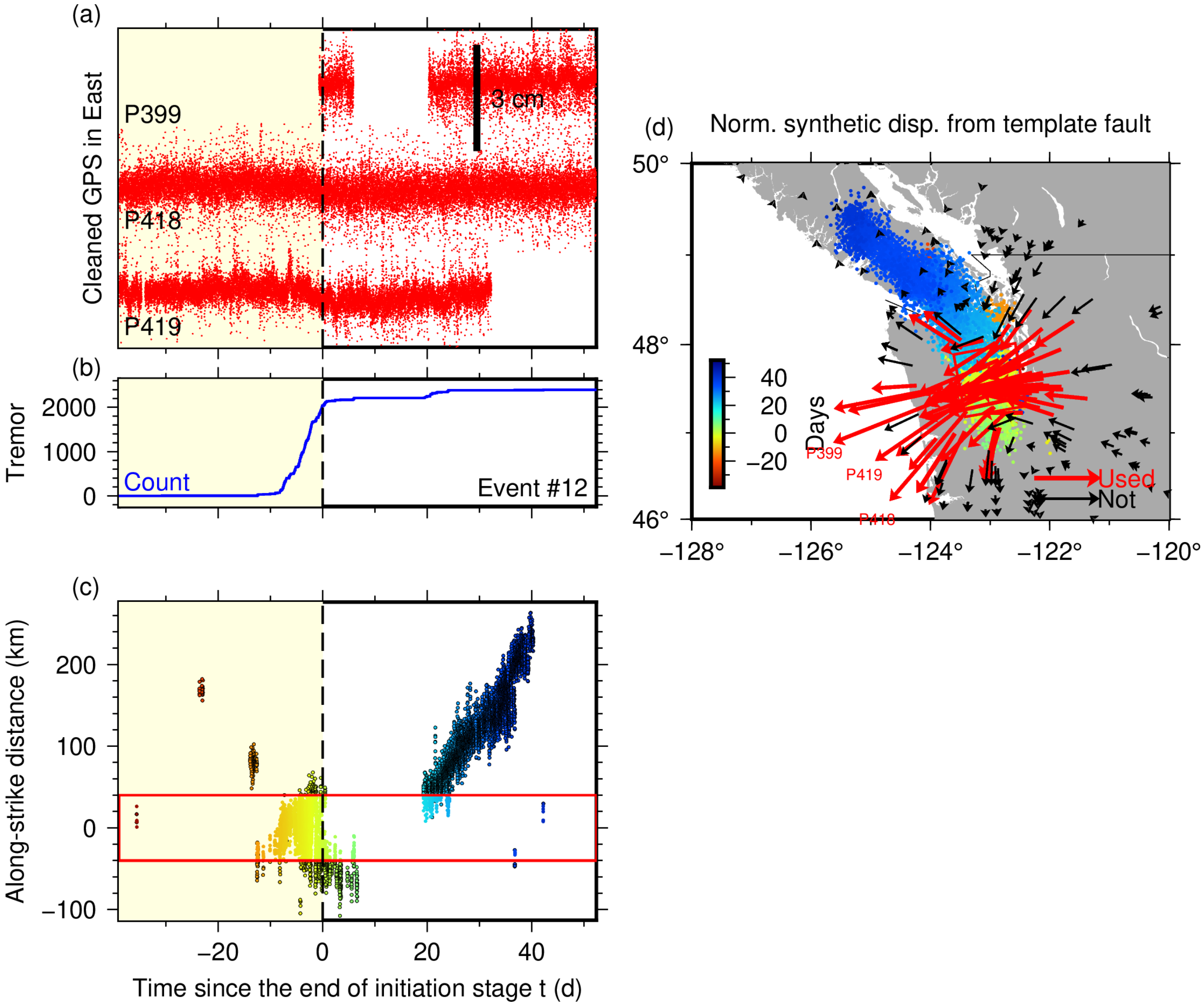

Figure S11. Same as Figure 1 but for Event #12.

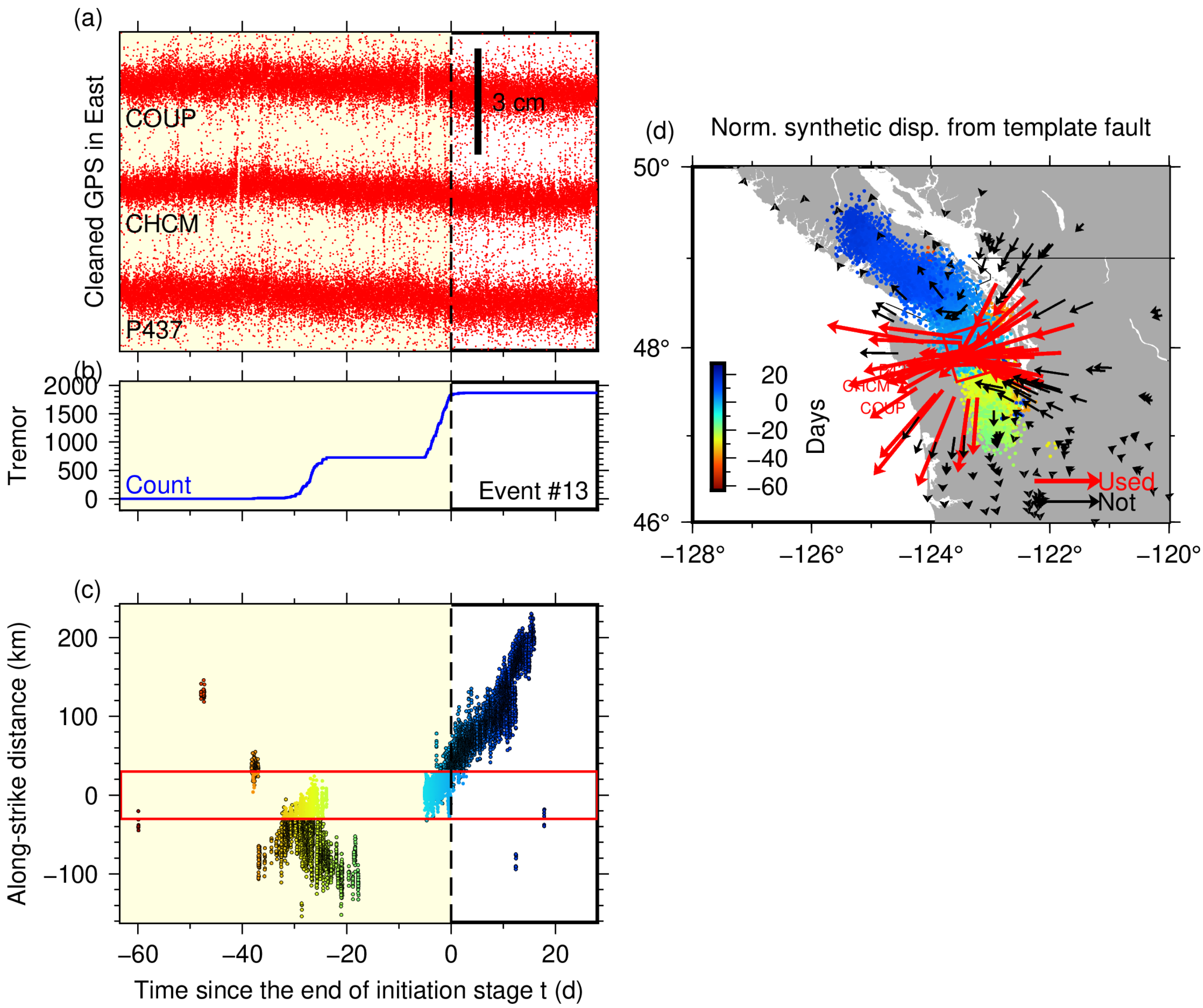

Figure S12. Same as Figure 1 but for Event #13.

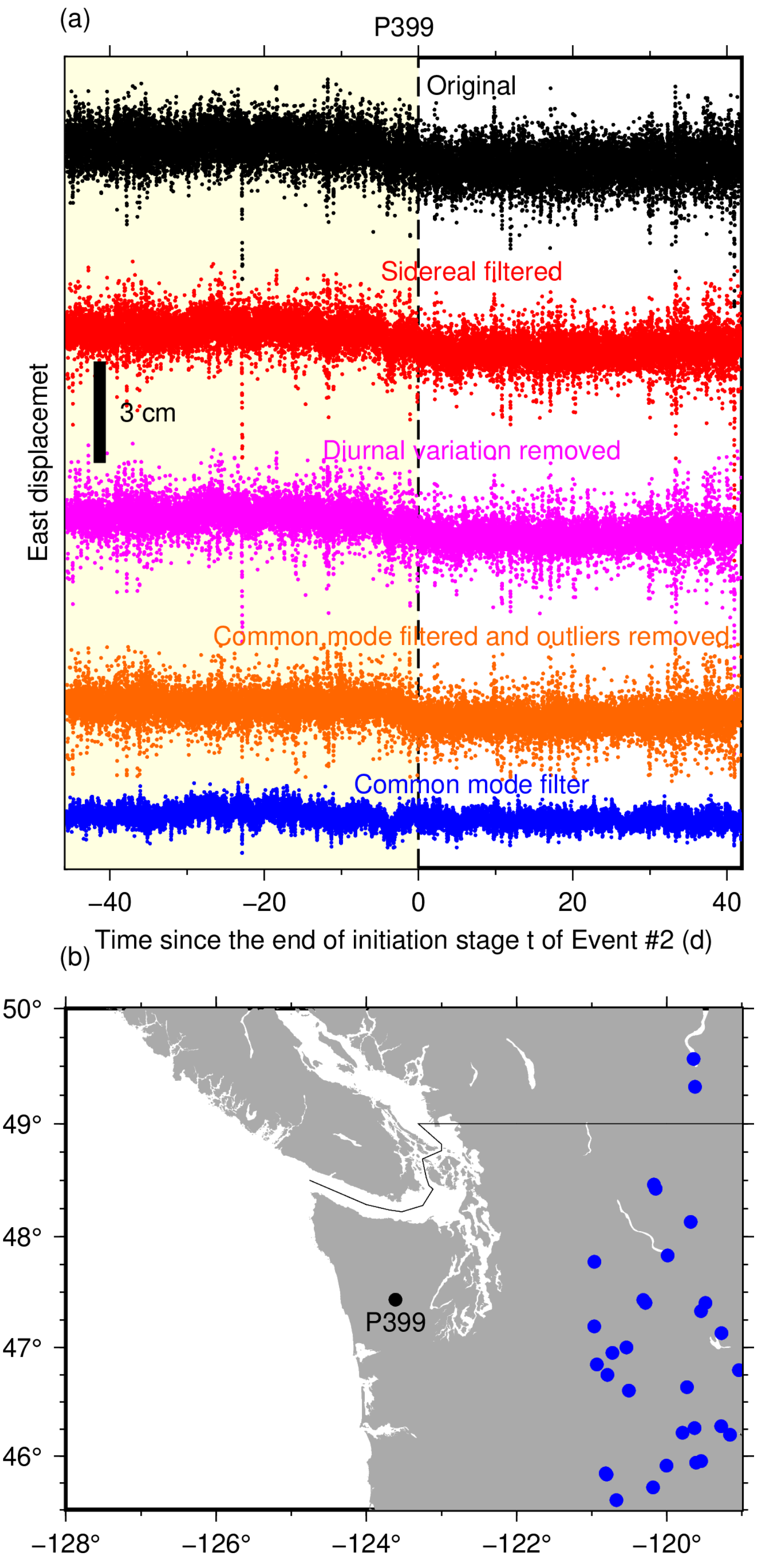

Figure S13. Cleaning process of subdaily GPS coordinates at site P399 for Event #2 as an example. (a) Results after each step of cleaning as labeled as well as common mode filter (blue) (Text S1). (b) The location of site P399 and site distribution which used to infer the common mode filter in (a) (blue dots).

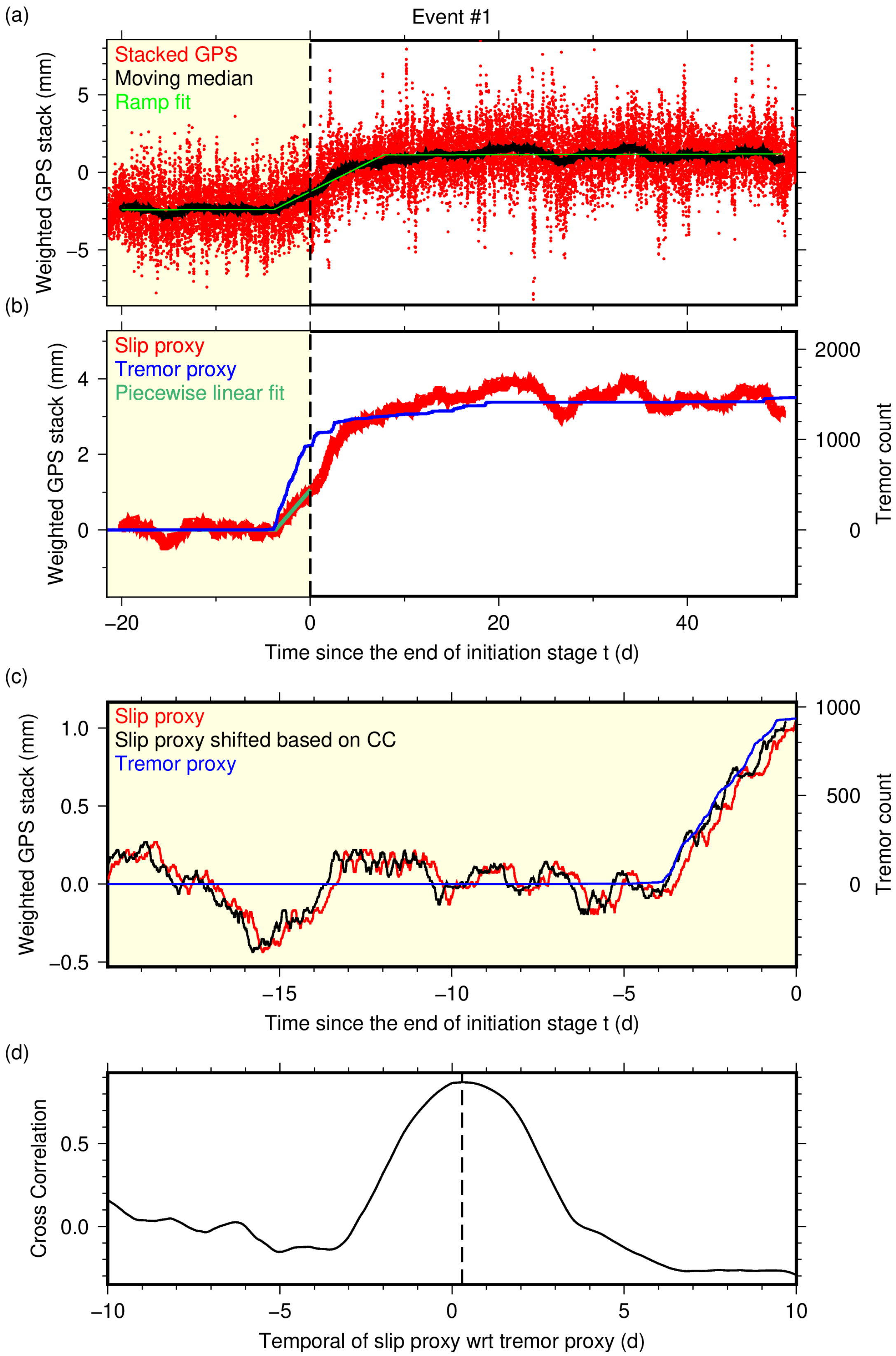

Figure S14. Same as Figures 2 and 3a-b but for Event #1

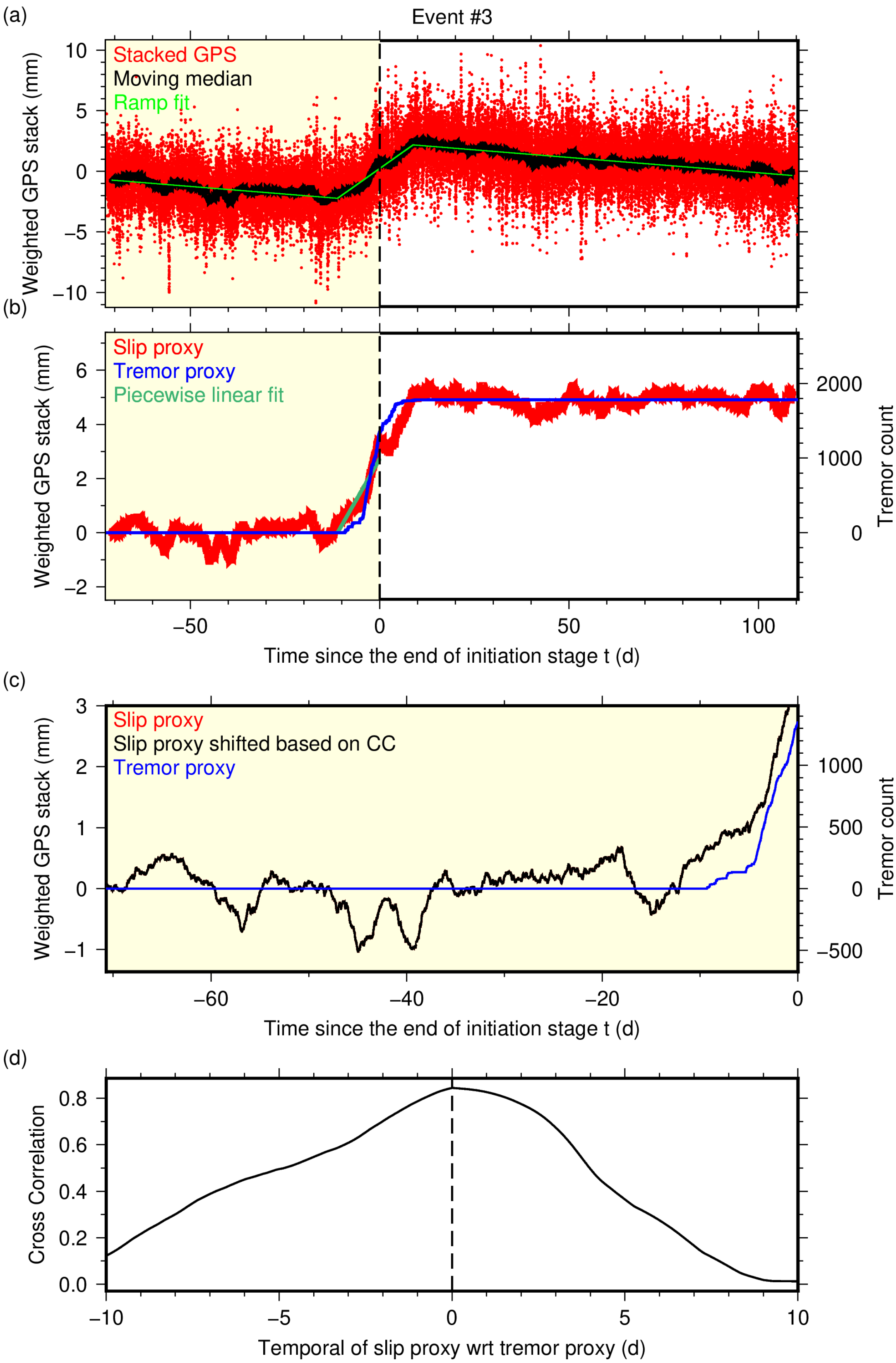

Figure S15. Same as Figures 2 and 3a-b but for Event #3

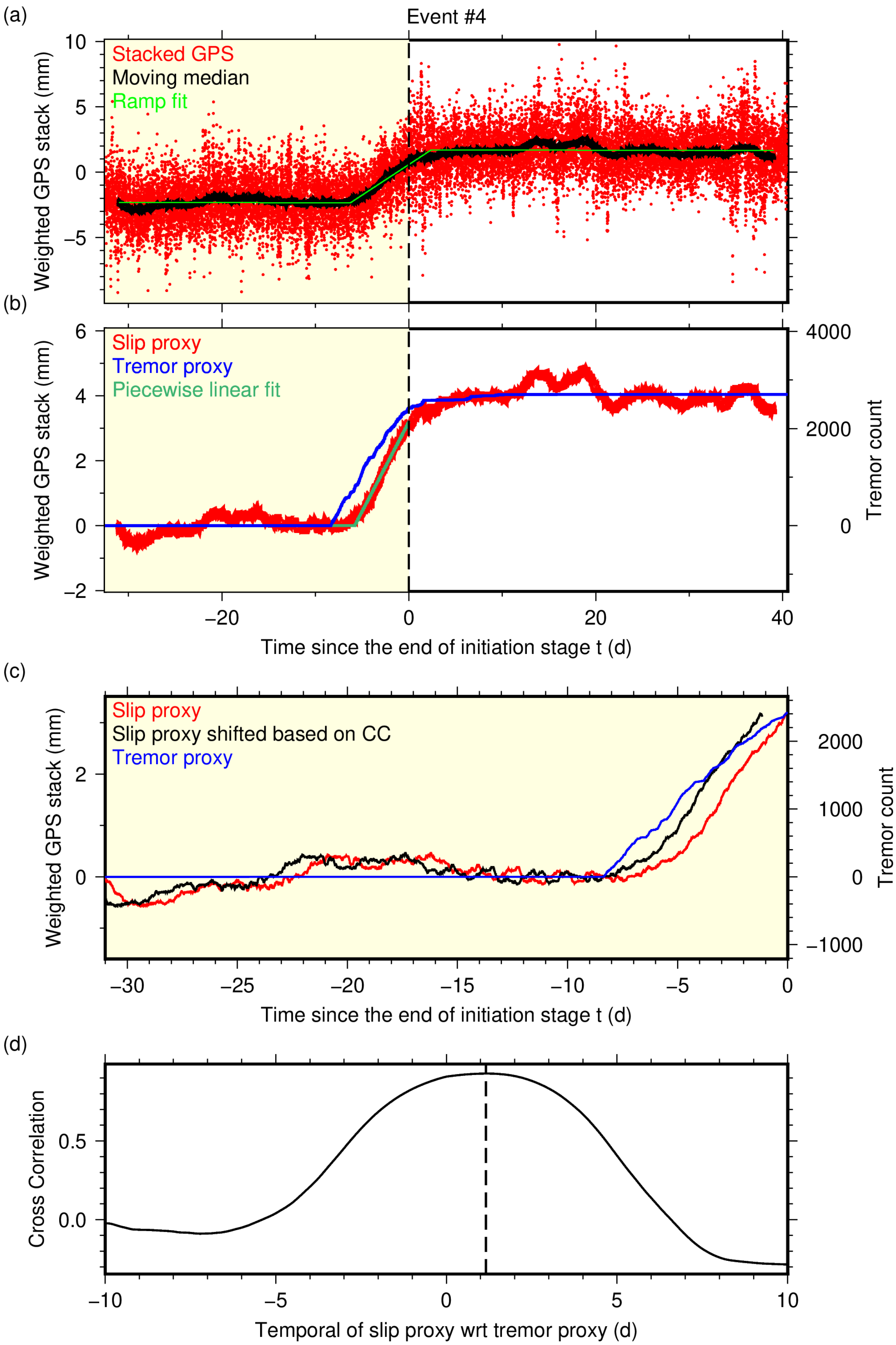

Figure S16. Same as Figures 2 and 3a-b but for Event #4

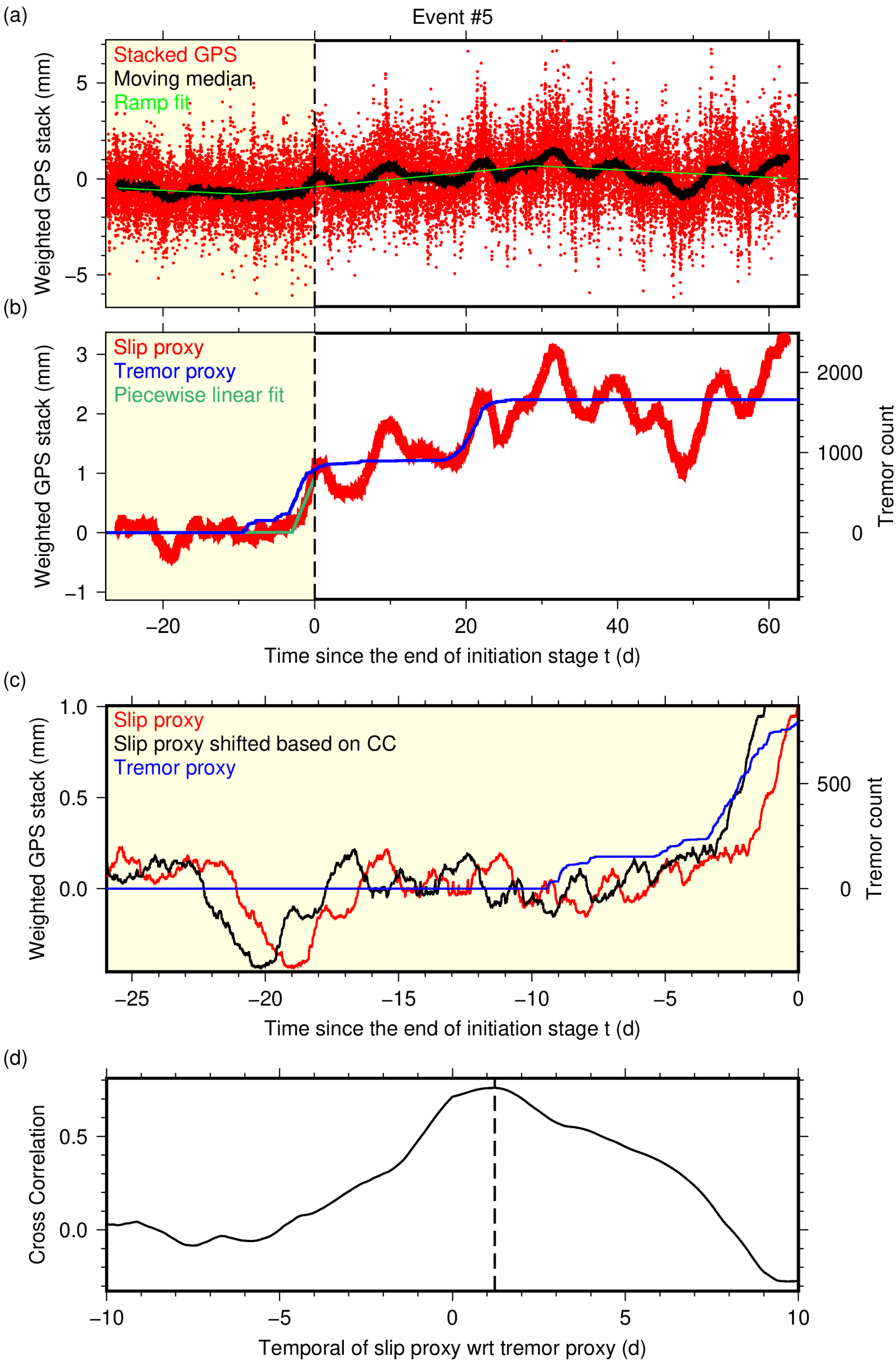

Figure S17. Same as Figures 2 and 3a-b but for Event #5

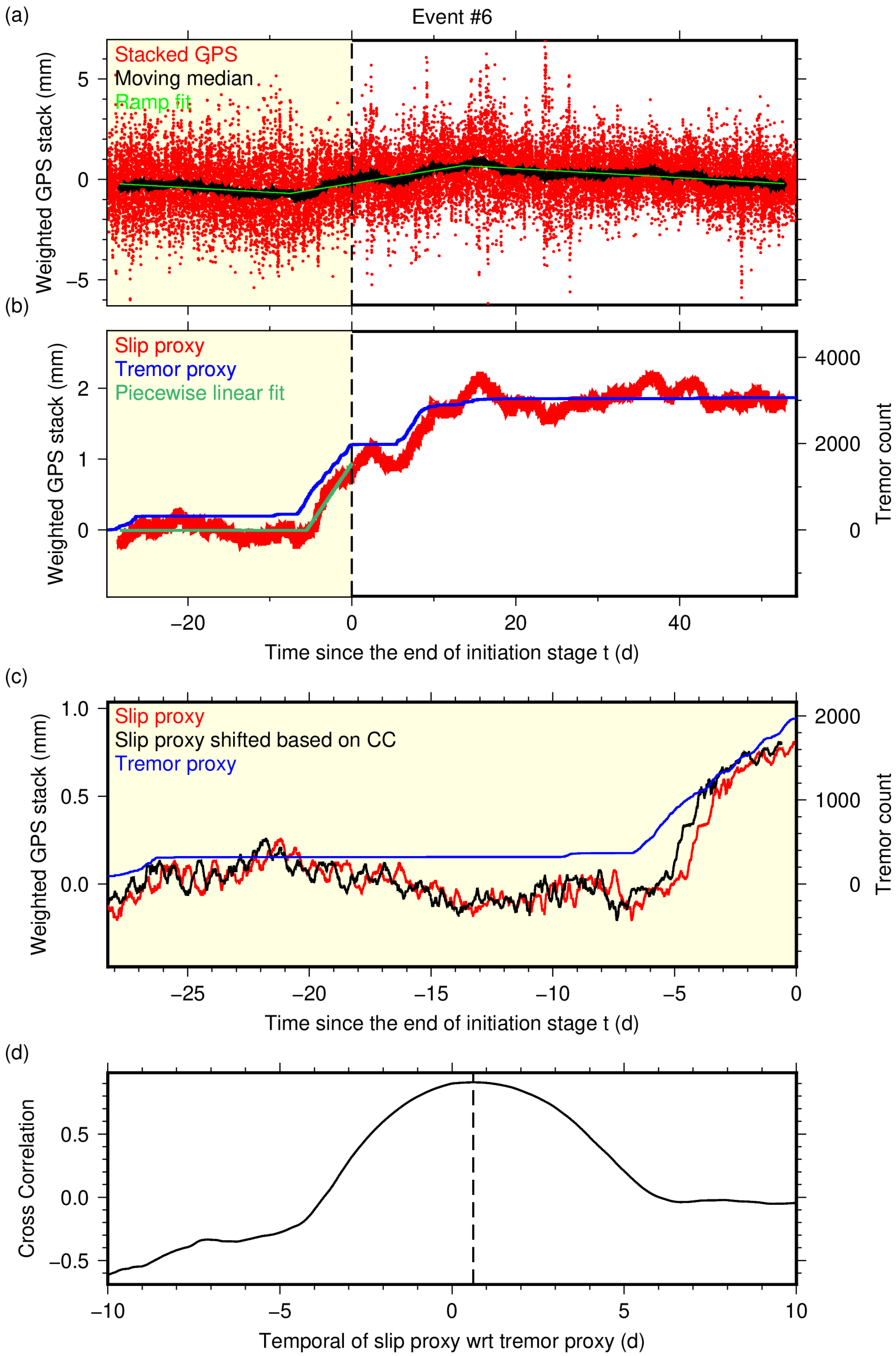

Figure S18. Same as Figures 2 and 3a-b but for Event #6

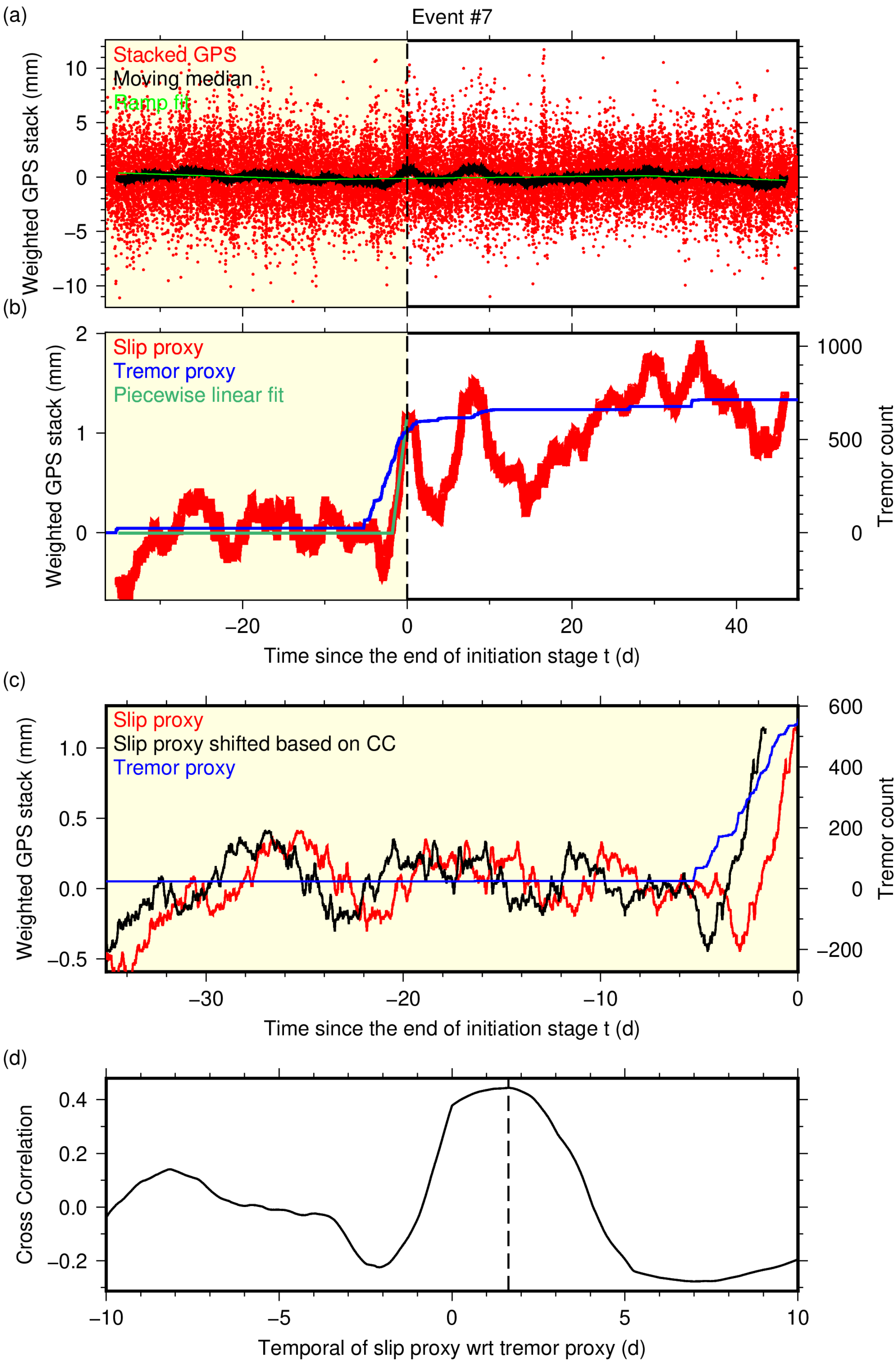

Figure S19. Same as Figures 2 and 3a-b but for Event #7

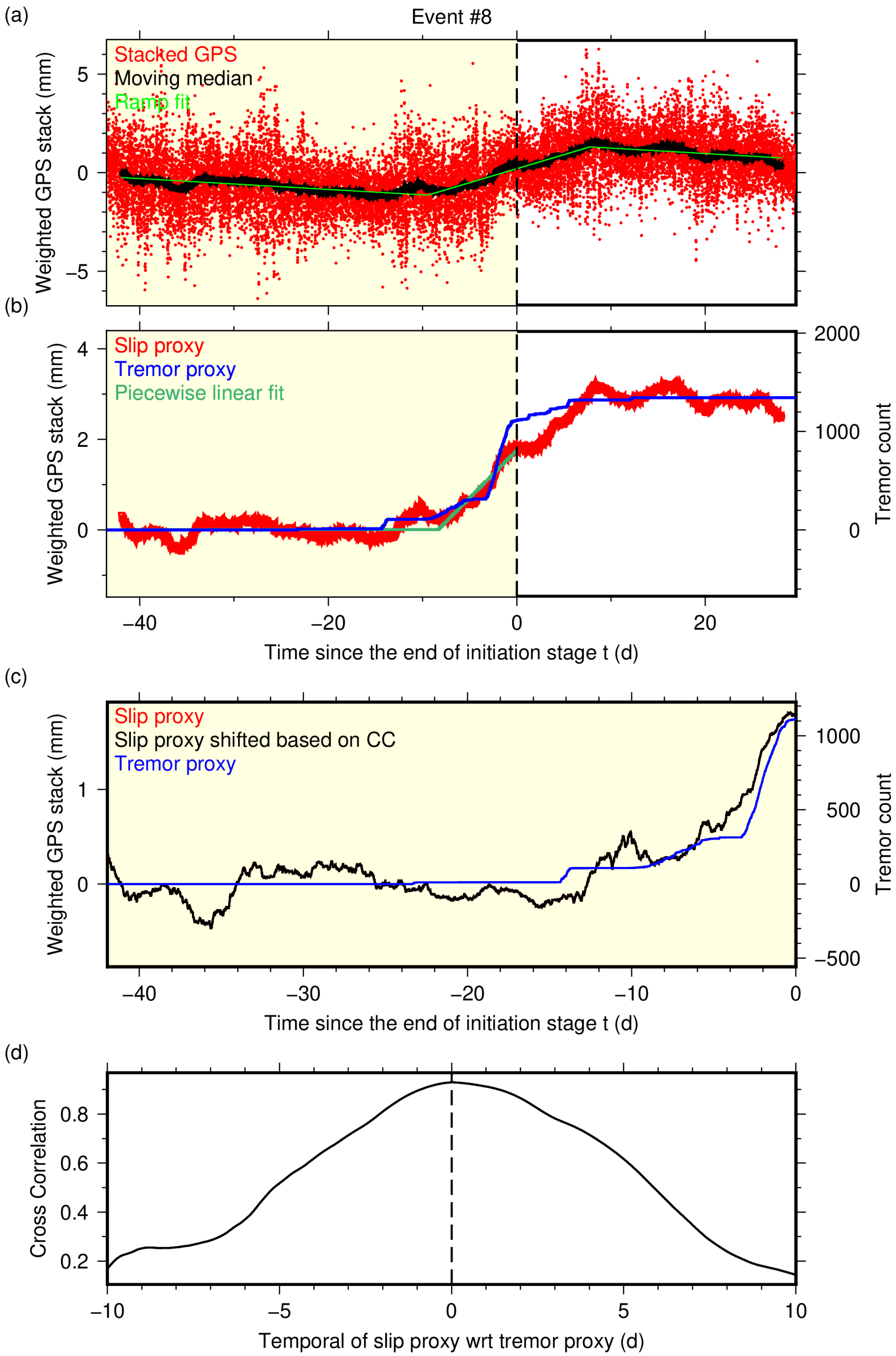

Figure S20. Same as Figures 2 and 3a-b but for Event #8

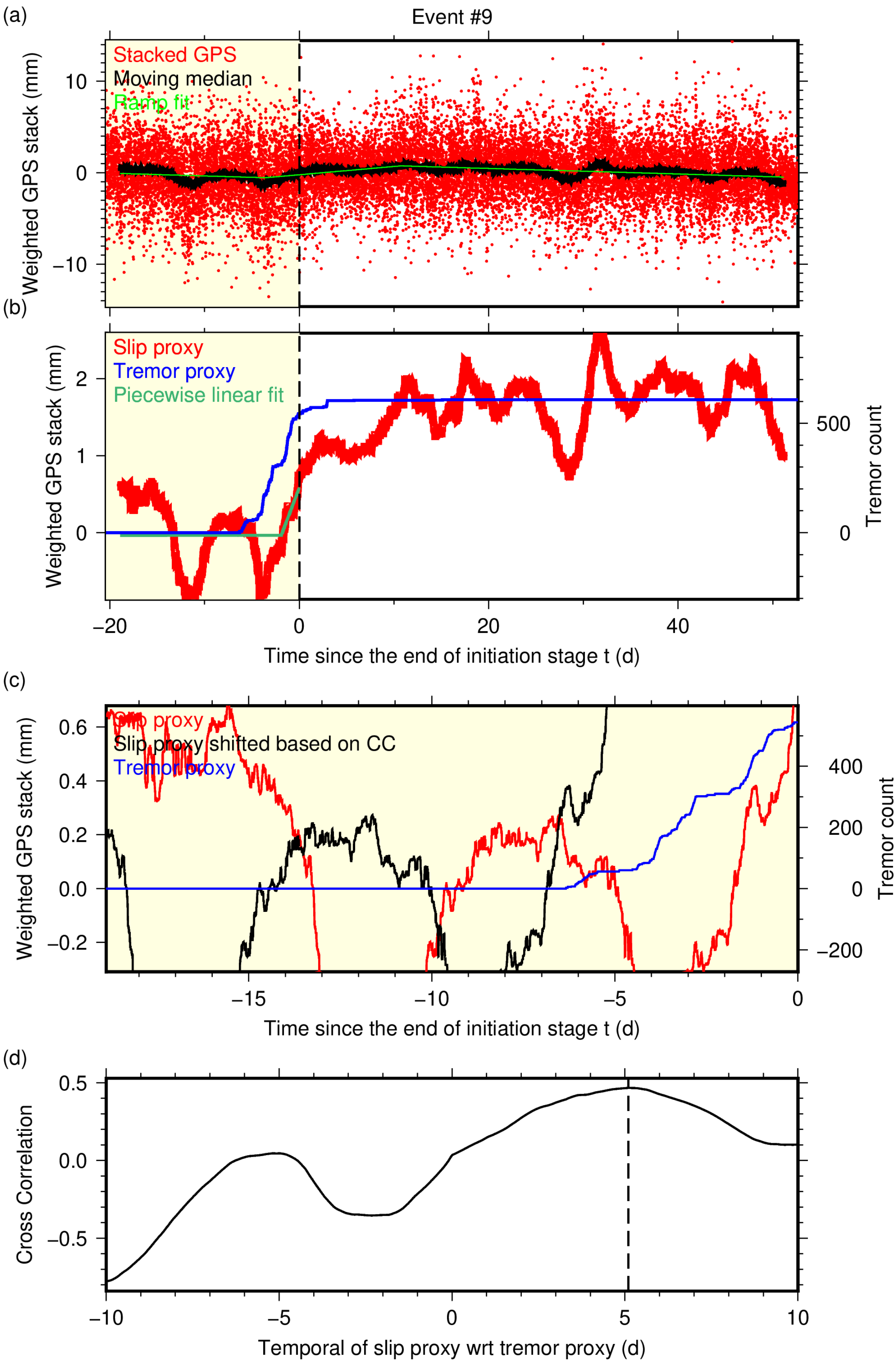

Figure S21. Same as Figures 2 and 3a-b but for Event #9

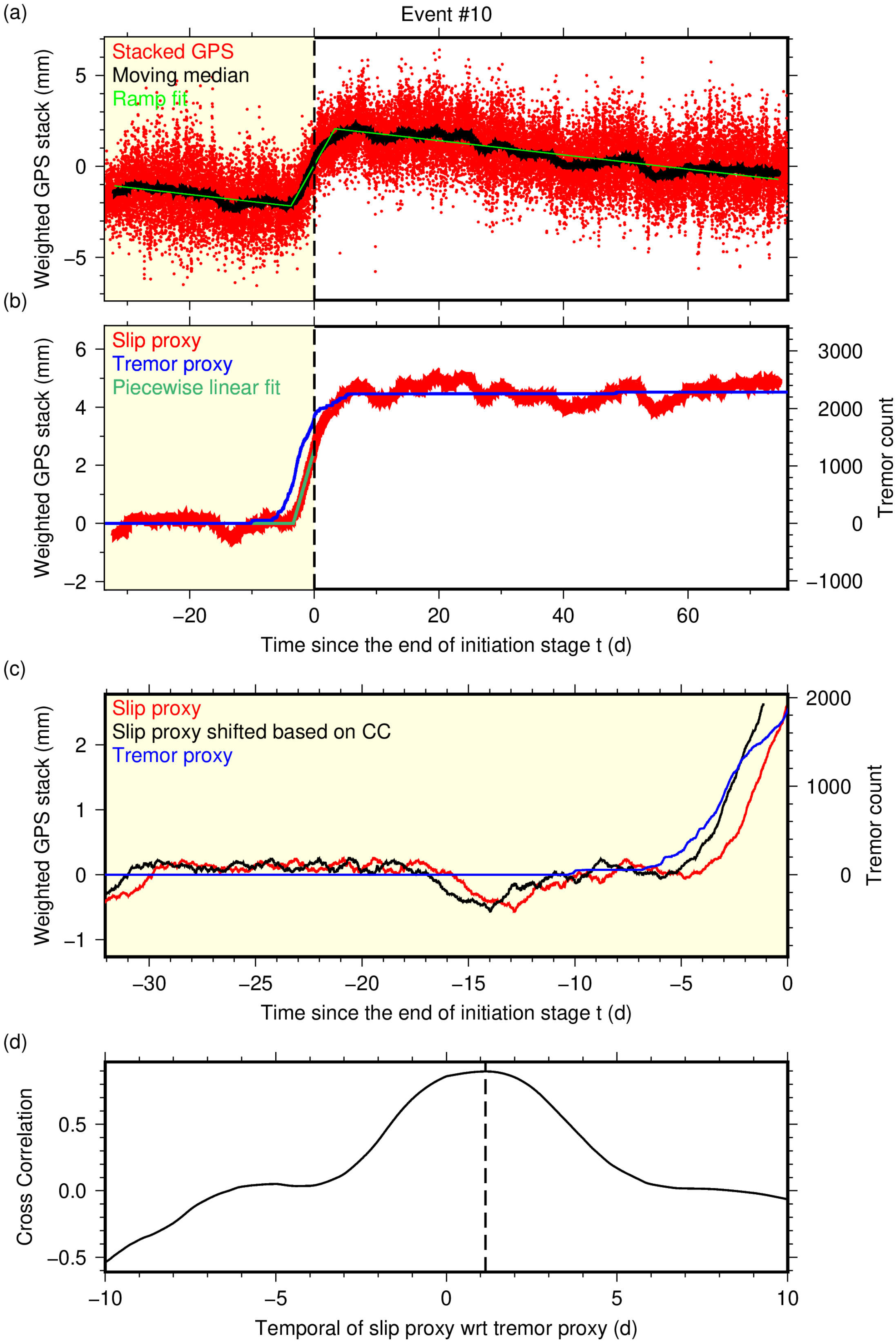

Figure S22. Same as Figures 2 and 3a-b but for Event #10

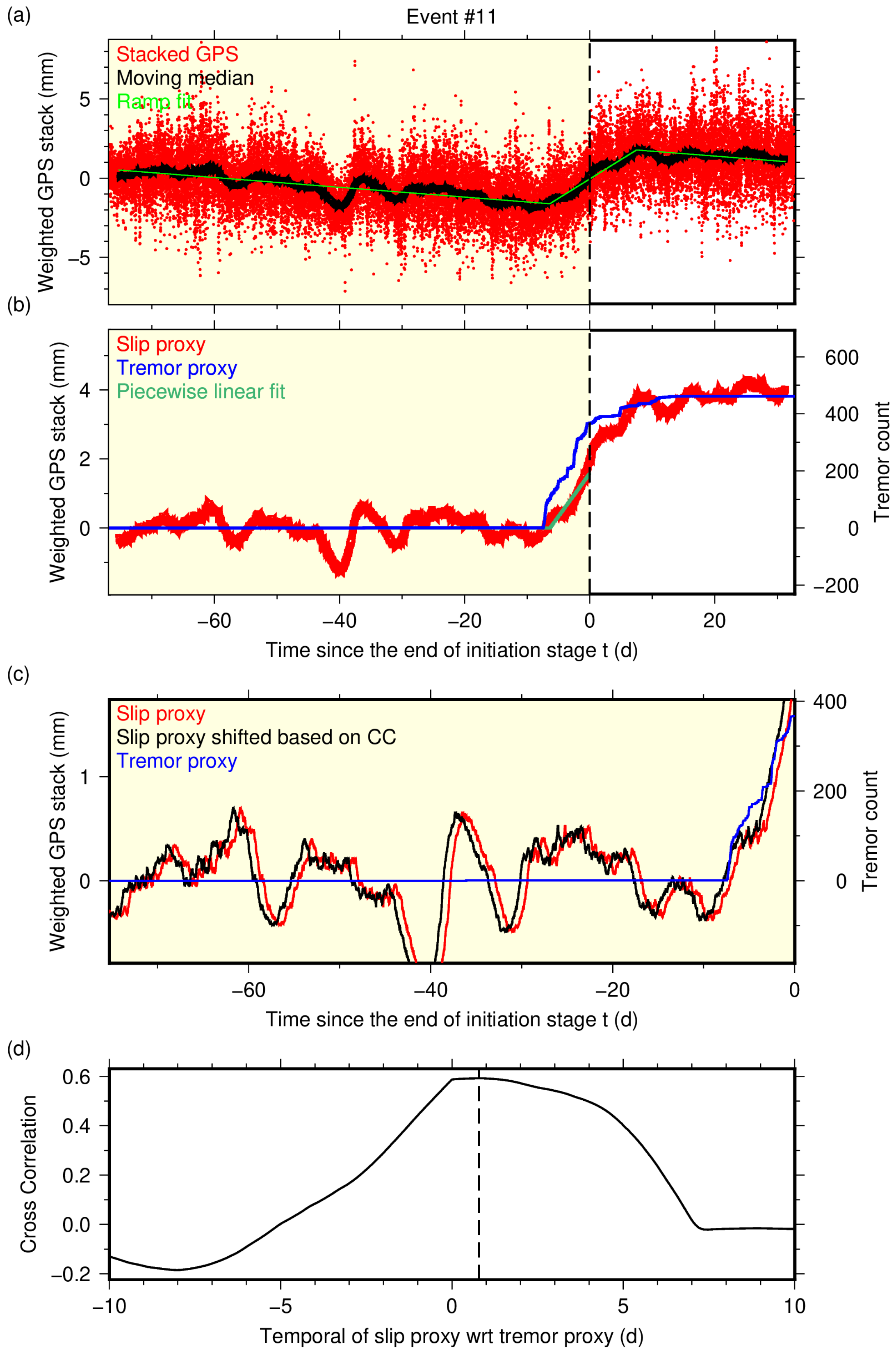

Figure S23. Same as Figures 2 and 3a-b but for Event #11

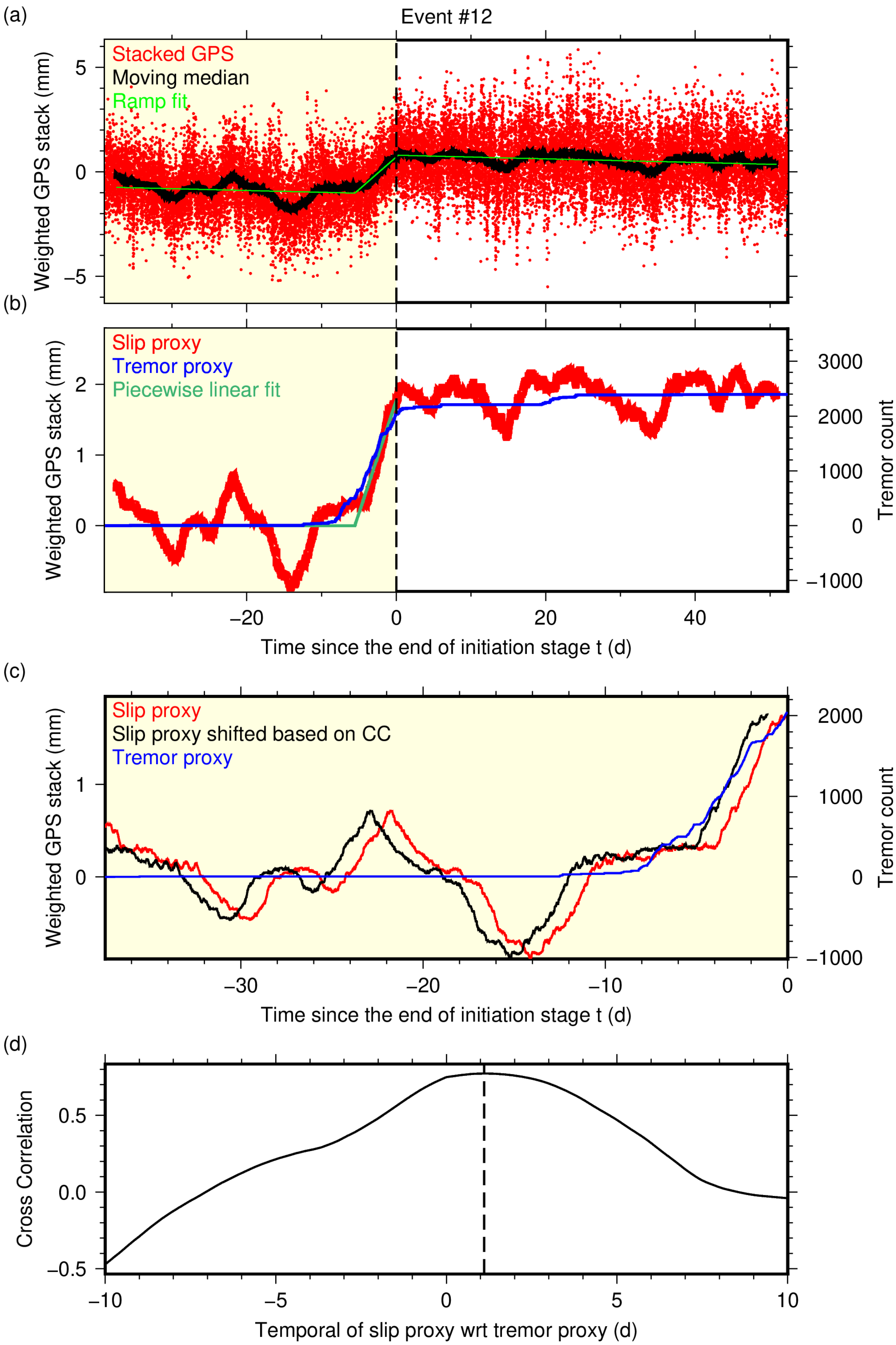

Figure S24. Same as Figures 2 and 3a-b but for Event #12

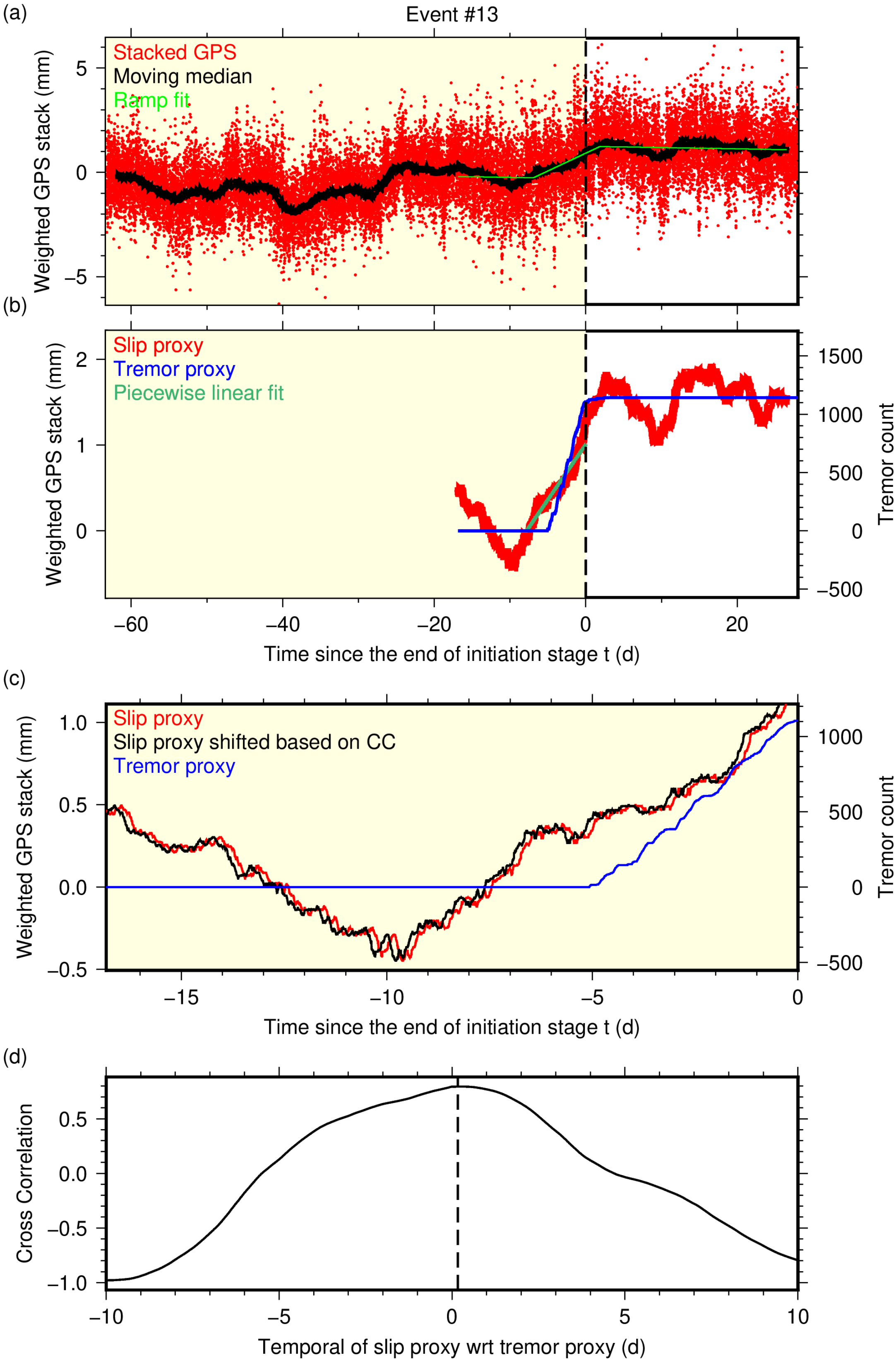

Figure S25. Same as Figures 2 and 3a-b but for Event #13. We removed the data period corresponding to Event #12 (Figures S24) because this event is a re-initiation event after the short halt of Event #12.

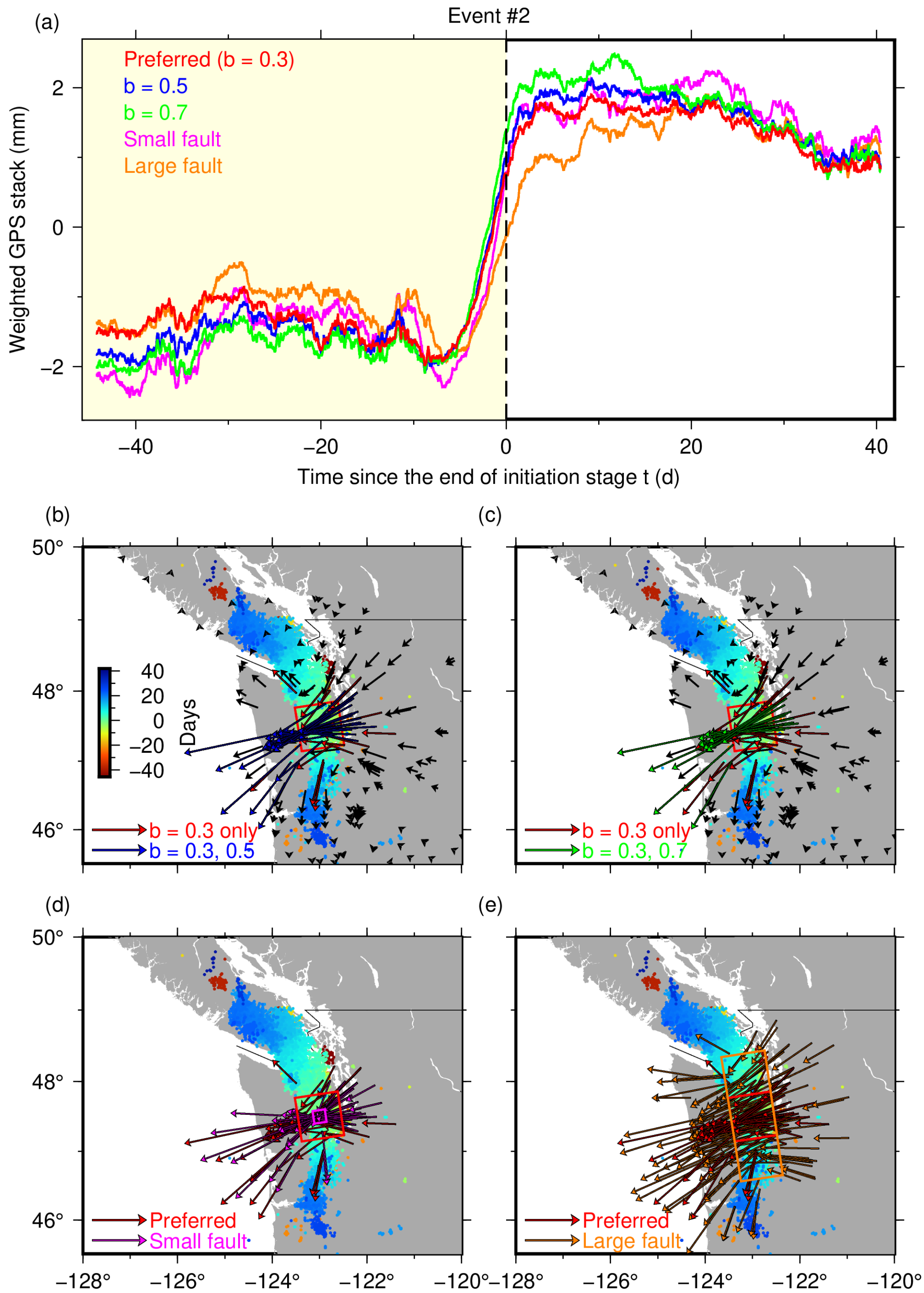

Figure S26. Tests for weights and site selection for GPS stack. (a) Stacked GPS with the preferred and four test cases as labeled. The main period of interest is highlighted in light yellow. (b-e) Weights (vectors) and template faults (rectangle) for the tests. (b-c) Tests with the preferred template fault but with a smaller number of sites controlled by b as labeled. (d-e) Cases with a smaller (d) and a larger (e) template faults. The template fault tested in (d) is too small (20 km x 20 km) and so not clearly illustrated.

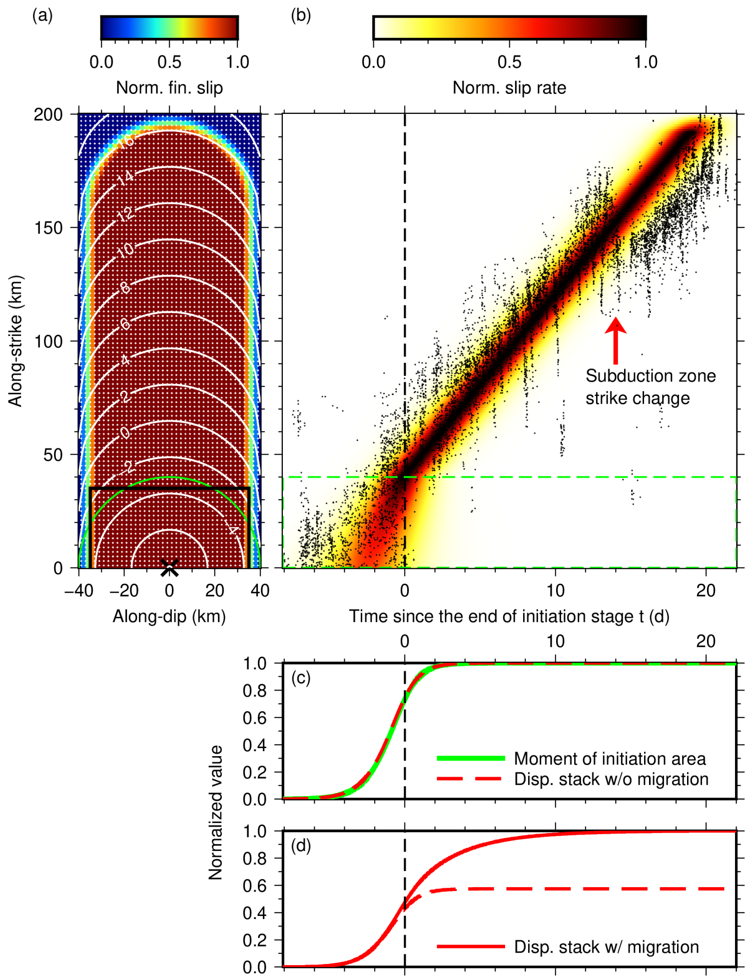

Figure S27. (a) Synthetic kinematic slow slip model mimicking Event #2 (color) (Figure 1). White contours indicate the rupture front with time in seconds with the rupture origin with a cross. The green curve and black rectangle indicate the initiation zone and the template fault, respectively. The time axis is concordantly shifted with the main observed ETS analysis. Only the upper half of the symmetric model is presented. (b) Spatio-temporal evolution of slip rate measured along the fault center in the strike direction (color). Green and black broken lines indicate the edge of the initiation zone and the end time of the initiation stage, respectively. Black dots indicate tremors during Event #2 (Wech, 2021), which we used to determine the end time of the initiation stage (Section 3.1). (c) Temporal evolution of normalized moment (green) and displacement stack (red) considering only the contribution from the initiation zone subfaults. (d) Displacement stack with (solid) and without (broken) the migrating slip contribution normalized by the final value of the former.

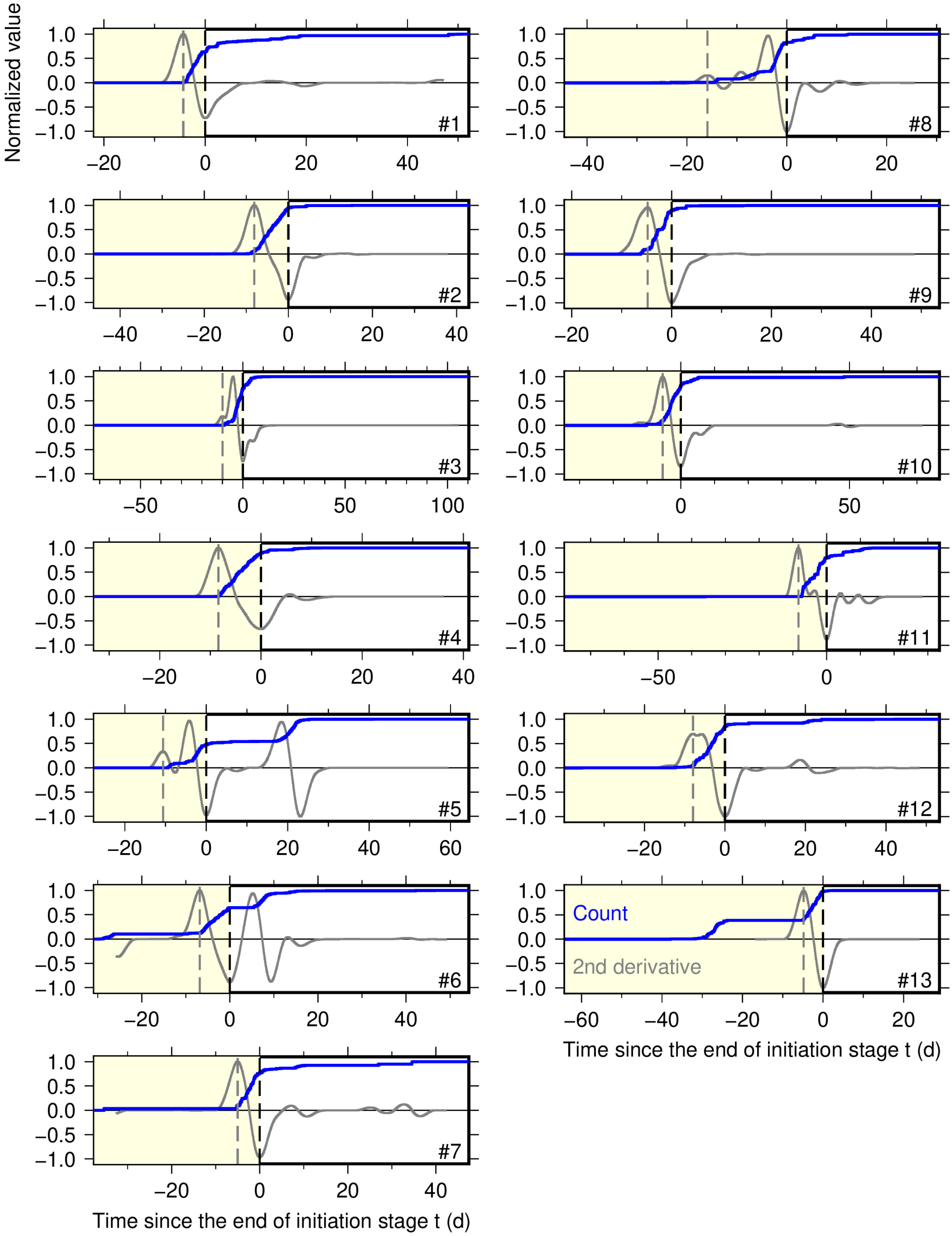

Figure S28. Determination of tremor onset time T_e^{tb} and the end time of the initiation stage T_e (vertical broken lines) for each event e as labeled. Curves indicate cumulative tremor counts in each template fault (normalized, blue) and their second derivative (normalized with the largest absolute value, gray).

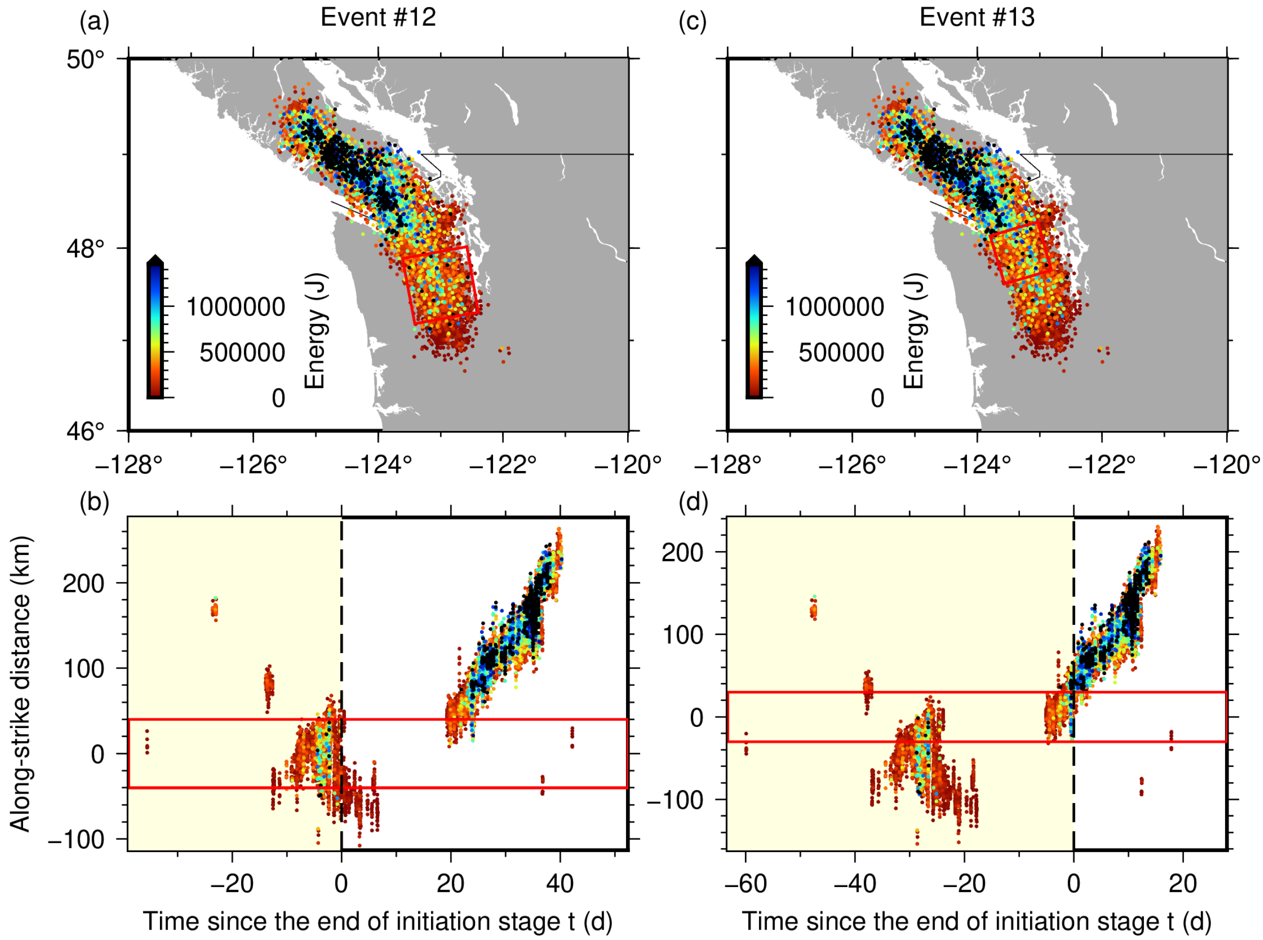

Figure S29. Tremor energy distribution (dot color) for Event #12 (a-b) and #13 (c-d). Refer to Figure 1 for other elements. Energy estimates were not supplied for events before 2017 in the PNSN catalog, so we only made plots for these two events (Table 1).

Table S1. Comparison of this study's and Michel et al. (2019)'s Event #s

This study's	Michel et al. (2019)'s	Data analysis period[a]
1	19, 20, 21	2009.55 - 2009.75
2	24, 25	2010.50 - 2010.74
3	28, 30, 31, 32	2011.25 - 2011.75
4	34, 35	2012.60 - 2012.80
5	38, 39	2013.10 - 2013.35
6	41, 42	2013.62 - 2013.85
7	41, 42	2013.62 - 2013.85
8	51, 52	2014.80 - 2015.00
9	51, 52	2014.80 - 2015.00
10	54, 55, 57	2015.90 - 2016.20
11	54, 55, 57	2015.90 - 2016.20
12	59, 60, 61	2017.05 - 2017.30
13	59, 60, 61	2017.05 - 2017.30

[a] Not the period of the initiation stage, but the data period we used

Table S2. Strike, dip, and rake angles for template faults

#	Strike[a] (°)	Dip[a] (°)	Rake[b] (°)
1	358.13	10.20	110.40
2	351.33	11.69	102.67
3	9.70	4.30	-237.16
4	314.88	10.00	67.86
5	352.05	2.69	104.72
6	351.33	11.69	102.67
7	316.00	7.58	71.39
8	348.22	11.78	99.46
9	330.39	13.99	84.85
10	313.93	10.06	66.75
11	9.48	9.63	-236.75
12	349.71	11.69	101.01
13	343.71	11.08	95.30

[a] Slab 2 (G. P. Hayes et al., 2018)

[b] Oregon block motion with respect to Juan de Fuca plate McCaffrey et al. (2007)